



Title	The muon-spin resonance ( $\mu$ SR) and density functional theory (DFT) study of YBa <sub>2</sub> Cu <sub>3</sub> O <sub>6</sub>
Author(s)	Irwan, Ramli
Citation	北海道大学. 博士(理学) 甲第13752号
Issue Date	2019-09-25
DOI	10.14943/doctoral.k13752
Doc URL	<a href="http://hdl.handle.net/2115/82768">http://hdl.handle.net/2115/82768</a>
Type	theses (doctoral)
File Information	Irwan_Ramli.pdf



[Instructions for use](#)

Doctoral Dissertation

**The muon-spin resonance ( $\mu$ SR) and  
density functional theory (DFT) study  
of  $\text{YBa}_2\text{Cu}_3\text{O}_6$**

( $\text{YBa}_2\text{Cu}_3\text{O}_6$  のミュオンสปิน緩和法 ( $\mu$ SR) および密度汎  
関数法 (DFT) による研究)

**Irwan Ramli**

Graduate School of Science, Hokkaido University  
Department of Condensed Matter Physics

September 2019



# Abstract

The  $\text{YBa}_2\text{Cu}_3\text{O}_6$  ( $\text{YBCO}_6$ ) is a mother compound of cuprate based high- $T_c$  superconductor. The  $\text{YBCO}_6$  shows long-range antiferromagnetic (AF) ordering and Mott insulator. The long-range AF ordering of this system disappears with doping and superconductivity appears. The detail study of magnetic and electronic state of  $\text{YBCO}_6$  is very important to understand from which the superconductivity appears. The  $\mu\text{SR}$  is extremely sensitive to probe the local magnetism due to the large gyromagnetic ratio of the muon spin and the first evidence of the presence long-range AF ordering was given by  $\mu\text{SR}$ . On the other hand,  $\mu\text{SR}$  has limitation due to unknown positions of the injected muon in the materials and complicated local perturbations given by the muon to its surroundings which prevent us to get deeper understanding of magnetic and electronic structure of the system.

The density functional theory (DFT) with the on-site coulomb repulsion,  $U$ , is employed to muon-site estimation and quantify the muon perturbation. The muon site estimation is based on the local minimum potential as muon has positive charge. The muon then introduced in to the  $\text{YBCO}_6$  as hydrogen ion. The calculation was done in the large supercell to compensate the behavior of the muon as ultradilute impurity. We found that three distinct muon sites, two near apical oxygen and one near planar oxygen. Our new high-statistics  $\mu\text{SR}$  experiment of high quality single crystal of  $\text{YBCO}_6$  reveals three distinct muon spin precession components which is consistent with our muon site estimation.

The main parameter that can be inferred from the  $\mu\text{SR}$  experiment is internal field at the muon sites. The examination of the internal fields at the estimated muon site was done on the basis dipolar interaction muon and magnetic ion in  $\text{YBCO}_6$  with considering the local crystal deformation. The internal field calculation by assume the spin reside in the particular ion (point dipole model) is overestimated the internal field at the muon site.

The strong hybridization between  $d$  orbital Cu with the  $p$  orbital O is play the crucial role in the magnetic properties of the cuprates which is known as covalency effect. This phenomena leads to the extension the spin density in the real space which is contradictive with the point dipole model. Since the long-range antiferromagnetic ordering in the Mott insulator arises from the strong on-site electron repulsive, the spin density has strong dependence to the strength the on-site electron repulsive which is characterized by  $U$  value. Thus, the carefully tune of the  $U$  value is needed. The best value of the  $U$ , 6.6 eV, for the  $\text{YBCO}_6$  is determined by absolute different the internal field from the experiment and theoretical calculations. The internal field calculation at each muon site on the basis of this model are fairly match with internal fields from the experiment.

It is also found that the ground state of the muon which is referred as zero-point energy (ZPE) vibration motion is play crucial role in the muon site determination. This effect is included simultaneously with covalency effect and local crystal deformation from DFT calculation in order to explain the local internal field at the muon site.

# Acknowledgement

I would like to sincerely thanks to my supervisor during my Ph.D course Dr. Isao Watanabe for his guidance in my research, effective dicussion to carefully consider physical phenomena and providing me various opportunity to discuss with other scientist from the worldwide through some conference and workshop.

I would like to thank Prof. Migaku Oda and Prof. Atsushi Kawamoto from department of condensed matter physics, Hokkaido University for their constructive and fruitful comments and suggestion to this thesis.

I also want to thanks to Prof. Shukri Sulaiman, Dr. M. M. I. Ibrahim and S. S. mohd-tajudin from the USM for nice collaborator and discussion during my Ph.D course.

Many thanks to Dr. Masahiko Iwasaki for providing me a change to join on his Laboratory Meson Science Laboratory and the administratif staff Fujita-san, Asakawa-san, Yamamoto-san and Iwanami-san for your kind help and support. I also thank to my friends and colegeous in Meson group (M. Darwis, S. Yoon, Noraina, M. R. Ramadhan, Julia, Dita P, Retno A, Suci W, Fahmi A, Harizon, S Aikawa and Utami W) and all Indonesian society in wako for sharing and many experiences during my stay in Japan.

Mostly of this work was done at HOKUSAI supercomputer in Advanced Center for Computing and Communication (ACCC) RIKEN. I am greatfull for the provision of the computing time allocation at that facilities. Thanks to the Paul Scherrer Institute (PSI) for the muon spin resonance experiment support. I also acknowledge RISTEKDIKTI and Lembaga Pengelola Dana Pendidikan (LPDP) Indonesia for providing the finansial support through Beasiswa Unggulan Dosen Indonesia-Luar Negeri (BUDI-LN) scholarship scheme.

My thanks also go out to Rector, Dean of faculty of science, Head of department of physics and all supporting staffs in Universitas Cokroaminoto Palopo (UNCP) for providing me great support and encouragement to pursue a Doctoral degree.

Last but not least, I would like to thank my wife Ulmiati Amdar and my son Muhammad Al fatih for great and wondfull time together and for your never ending support. I also thanks to my big family in Indonesia for their support and praying for my success.



# Contents

<b>Abstract</b>	<b>iii</b>
<b>Acknowledgement</b>	<b>v</b>
<b>1 Introduction</b>	<b>1</b>
1.1 The history of high- $T_c$ superconductor . . . . .	1
1.2 Basic properties of high- $T_c$ superconductor . . . . .	3
1.3 The phase diagram of high- $T_c$ superconductor . . . . .	6
1.4 The magnetic properties of the $\text{YBa}_2\text{Cu}_3\text{O}_6$ . . . . .	7
1.5 The muon-site problem . . . . .	13
1.6 The covalent bonding . . . . .	17
1.7 The thesis outline . . . . .	20
<b>2 The muon-spin rotation</b>	<b>21</b>
2.1 The muon production and implantation process . . . . .	21
2.2 The $\mu\text{SR}$ experiment . . . . .	23
2.3 Internal field at the muon site . . . . .	28
<b>3 The density functional theory</b>	<b>31</b>
3.1 Many-body problem . . . . .	31
3.2 The electron density . . . . .	32
3.3 The exchange-corelation function . . . . .	33
3.3.1 The local density approximation (LDA) . . . . .	33
3.3.2 The generalized gradient approximation (GGA) . . . . .	34
3.4 Pseudopotential . . . . .	35
3.5 Plane wave basis set . . . . .	37
3.6 Solve the Kohn-Sham self consistently . . . . .	38
3.7 The DFT+U . . . . .	38
3.8 The muon site calculation . . . . .	41
<b>4 Results and discussion</b>	<b>43</b>
4.1 The $\mu\text{SR}$ experiment . . . . .	43
4.2 The muon-site calculation . . . . .	45



---

4.2.1	The band-structure calculations . . . . .	45
4.2.2	Initial muon site . . . . .	46
4.2.3	The muon perturbation . . . . .	47
4.2.4	Internal fields simulation . . . . .	50
4.3	Quantum correction . . . . .	53
4.4	The covalency effect . . . . .	55
4.5	Discussion . . . . .	58
<b>5</b>	<b>Summary and Outlook</b>	<b>63</b>
5.1	Summary . . . . .	63
5.2	Outlook . . . . .	64
<b>A</b>	<b>The detail of the VASP calculations</b>	<b>65</b>
A.1	Input file . . . . .	65
A.1.1	INCAR . . . . .	65
A.1.2	POSCAR . . . . .	68
A.1.3	POTCAR . . . . .	69
A.1.4	KPOINTS . . . . .	72
A.2	OUTPUT . . . . .	72
A.3	Implementation in the Supercomputer . . . . .	73
<b>B</b>	<b>The dipole-field calculation program</b>	<b>75</b>
<b>C</b>	<b>Internal fields calculations results</b>	<b>81</b>
	<b>Bibliography</b>	<b>85</b>

# List of Figures

1.1	plot of resistance ( $\Omega$ ) versus temperature (K) for mercury from the 26 October 1911 experiment shows the superconducting transition at 4.20 K . . .	1
1.2	The formation of the Cooper pair in conduction process of superconductivity	3
1.3	$T_c$ versus time . . . . .	4
1.4	The illustration of Meissner effect. . . . .	5
1.5	The magnetic phase diagram for type I and type II superconductor. . . . .	6
1.6	The illustration of London penetration depth . . . . .	6
1.7	Typical phase diagram of high- $T_c$ cuprates. $T_c$ and $T_N$ are the superconducting transition temperature and Néel temperature, respectively. . . . .	7
1.8	$\mu$ SR spectra of $\text{YBa}_2\text{Cu}_3\text{O}_{6.2}$ at 315 K, 250 K, and 15 K . . . . .	8
1.9	The zero-field $\mu$ SR time spectra of $\text{YBa}_2\text{Cu}_3\text{O}_x$ at 20 mK in all cases except for $x = 6.04$ for which $T = 90\text{mK}$ . . . . .	9
1.10	Proposed magnetic structure from the neutron diffraction for $\text{YBa}_2\text{Cu}_3\text{O}_{6+x}$ with $x \sim 0$ . . . . .	10
1.11	The magnetic unit cell of $\text{YBa}_2\text{Cu}_3\text{O}_6$ . . . . .	11
1.12	The universal relation between $T_c$ and relaxation rate. . . . .	12
1.13	The TF- $\mu$ SR measurements of the vortex state of the high- $T_c$ . . . . .	13
1.14	The coexistence the short -range magnetic ordering in Y-based and La-based high- $T_c$ cuprates . . . . .	14
1.15	Fourier transform of the zero field- $\mu$ SR time spectra of $\text{YBa}_2\text{Cu}_3\text{O}_{6.2}$ and $\text{YBa}_2\text{Cu}_3\text{O}_{6.3}$ . . . . .	15
1.16	The proposed muon sites from dipolar field scanning . . . . .	16
1.17	The proposed muon sites from dipolar field scanning with magnetic moment direction in $\langle 110 \rangle$ . . . . .	17
1.18	The crystal field splitting of the $3d$ orbital . . . . .	18
1.19	The molecular picture of the hybridization of the Cu $3d$ orbital and O $2p$ orbital . . . . .	19
1.20	The covalently hybridized of the unpaired magnetic electron in $\text{Sr}_2\text{CuO}_3$ obtained from the ab initio LDA + U calculation . . . . .	20
2.1	Illustration of the two types of muon beam (a) continuous wave which muons are implanted one by one and (b) pulsed which muons are implanted in a bunch. . . . .	22

2.2	The schematic of the implantation of the muon process in the sample . . . . .	24
2.3	The $\mu$ SR time window for magnetic fluctuations in materials which is complementary to other experimental techniques. . . . .	25
2.4	The Larmor precession of the muon in the magnetic field . . . . .	26
2.5	The illustration $\mu$ SR experiment . . . . .	27
2.6	The asymmetry function . . . . .	28
2.7	The magnetic volume fraction in $\text{CeCu}_{2.2}\text{Si}_2$ . . . . .	29
2.8	The experiment set up at PSI . . . . .	30
3.1	The many body interaction. . . . .	31
3.2	The DFT perspective . . . . .	33
3.3	The illustration of the pseudopotentials . . . . .	35
3.4	The illustration of the parameter in the PAW . . . . .	36
3.5	The flow chart of the self consistent procedure . . . . .	39
3.6	The schematic energy-band diagrams of a Mott–Hubbard insulator . . . . .	40
4.1	The single crystal of $\text{YBa}_2\text{Cu}_3\text{O}_6$ . . . . .	44
4.2	The $\mu$ SR time spectra and its fourier transform . . . . .	44
4.3	The band structure and DOS of $\text{YBa}_2\text{Cu}_3\text{O}_6$ . . . . .	45
4.4	The band gap dependence on the on-site coulomb interaction parameter, $U$ . The size of the gap is proportional with the $U$ value . . . . .	46
4.5	The Initial muon site in $\text{YBa}_2\text{Cu}_3\text{O}_6$ . . . . .	47
4.6	The supercell $4\times 4\times 2$ unit cells . . . . .	48
4.7	The crystal structure (a) unperturbed system, the muon perturbation with (b) muon at M1 (c) muon at M2 and muon at M3 . . . . .	49
4.8	The illustrated of the Lorentz sphere . . . . .	50
4.9	The convergence test of the internal fields . . . . .	51
4.10	The magnetic moment size of Cu as function of the $U$ . . . . .	51
4.11	The calculated internal fields at muon site as function of the $U$ based on point dipole model without any crystal deformation. . . . .	52
4.12	The calculated internal fields at muon site as function of the $U$ based on point dipole model with crystal deformation. . . . .	53
4.13	The illustration of the zero-point energy (ZPE) vibration of muon. . . . .	54
4.14	The muon probability density. . . . .	54
4.15	The muon probability density cross section . . . . .	55
4.16	The calculated internal fields at muon site as function of the $U$ based on point dipole model with crystal deformation and quantum correction. . . . .	56
4.17	The muon perturbation to the spin density . . . . .	57
4.18	The calculated internal fields at muon site as function of the $U$ based on spin density with crystal deformation and quantum correction. . . . .	58
4.19	The polynomial fitting of the difference between experimental results and calculation as function of $U$ . . . . .	59

---

B.1 The folow chart of dipole field program . . . . . 75



# List of Tables

2.1	The properties of the positive muon . . . . .	21
C.1	The internal field at each muon sites as function of the U value. This calculation is on the basis point dipole model . . . . .	81
C.2	The internal field at each muon sites as function of the U value. This calculation is on the basis point dipole model by including lattice deformation	82
C.3	The internal field at each muon sites as function of the U value. This calculation is on the basis point dipole model by including lattice deformation and zero point energy vibration . . . . .	82
C.4	The internal field at each muon sites as function of the U value. This calculation is on the basis spin density (the extended spin in the real space due to the covalency effect) by including lattice deformation and zero point energy vibration . . . . .	83



# Chapter 1

## Introduction

### 1.1 The history of high- $T_c$ superconductor

The history of superconductivity began when H.K. Onnes successfully liquefied helium 1908 for the first time which enable him to study the electrical properties of pure metal at low temperature. In three years later, he found that the resistivity of pure mercury suddenly disappeared below temperature 4.2 K as shown in Fig. 1.1. This phenomena is known as superconductivity and the temperature at which below this temperature the resistivity disappear is known as critical temperature,  $T_c$  [1].

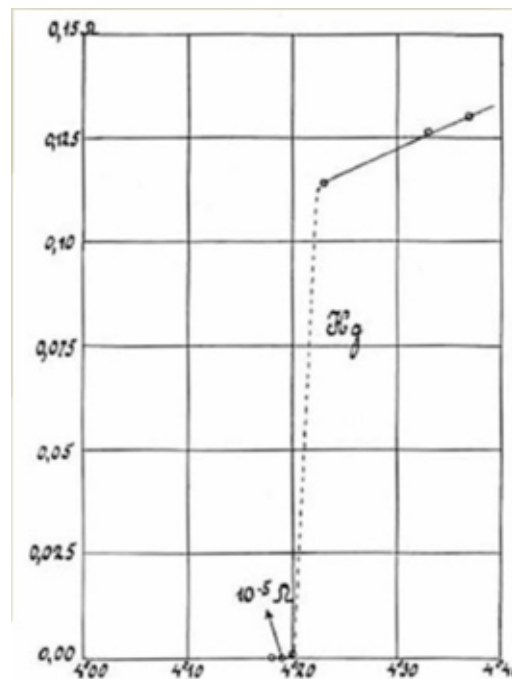


Figure 1.1: plot of resistance ( $\Omega$ ) versus temperature (K) for mercury from the 26 October 1911 experiment shows the superconducting transition at 4.20 K



Since this discovery, the scientists have been searching for new material which has higher  $T_c$  for the potential application as non-dissipation power wire. On the other hand, many scientists also attempted to explain the superconductivity mechanism. The first successfully microscopic theory of superconductivity to explain how the material, like mercury, can show the superconductivity phenomena was given by John Bardeen, Leon Cooper, and Robert Schrieffer in 1957 [2, 3]. This theory is known as BCS theory and one of the most successfully theory in solid-state. The central idea of BCS theory is the formation of electron pair in the conduction process which is known as ‘‘Cooper pair’’. Based on this theory, the first electron passes through the positive ion in the crystal and caused the lattice distortion. As this first electron leave the distortion area, the positive charge concentration is increase and attract the second electron as shown in the Fig. 1.2. Those two electrons are bound together by lattice vibration which is called ‘‘phonon’’. The Cooper pair in the ground state separated from excited states by Superconducting energy gap,  $E_g$ . The binding energy between electron which are form Cooper pair can be written as [4],

$$\Delta = \frac{2\hbar\omega_D}{\exp(1/N_F V) - 1} \quad (1.1)$$

The BCS theory predicted the  $T_c$ ,

$$T_c = 1.13E_D \exp(-1/N(0)V) \quad (1.2)$$

where  $E_D$  is the Debye cut-off energy,  $N(0)$  is the electronic density of states at the Fermi energy,  $V$  is the coupling potential of electron-phonon interaction. This equation could give explanation for the superconductors phenomena at that time. As we can see in the equation,  $T_c$  is directly proportional with  $\omega_D$  which is proportional with inverse square root of the ionic mass  $M$ ,

$$T_c \propto \omega_D \propto M^{1/2} \quad (1.3)$$

which in agreement with experimental observation of the isotope effect in superconductor. The relatively low of  $\Delta(T = 0)$  (in order of a few meV) which is smaller than typical phonon energies lead to the implication that the  $T_c$  on the basis of the BCS theory will never exceed 30 K [5]. The optimize electron-phonon mechanism yields the maximum  $T_c = 39$  K [6].

The new era of superconductivity began with the discovery superconductivity in a copper-oxide, La-Ba-Cu-O compound, at a temperature 35 K [7]. In the following years, the superconductivity was observed in another cuprates, Y-Ba-Cu-O compound, which has critical temperature between 80 and 93 K [8]. This system was the first superconductor with a  $T_c$  higher than the boiling point of liquid nitrogen, 77 K. The  $T_c$  of the cuprates oxides is relatively high compare to the BCS predictions and known as unconventional superconductor or high- $T_c$  superconductors. Therefore it is believed that the superconductivity mechanism is different from the conventional superconductor. Until nowadays, the cuprates is still the class of superconductivity which have highest  $T_c$ . The time of discovery versus  $T_c$  for the high- $T_c$  is shown in the Fig. 1.3. Many theories have been proposed to explain the high- $T_c$  superconductivity mechanism but it is still debatable until now.

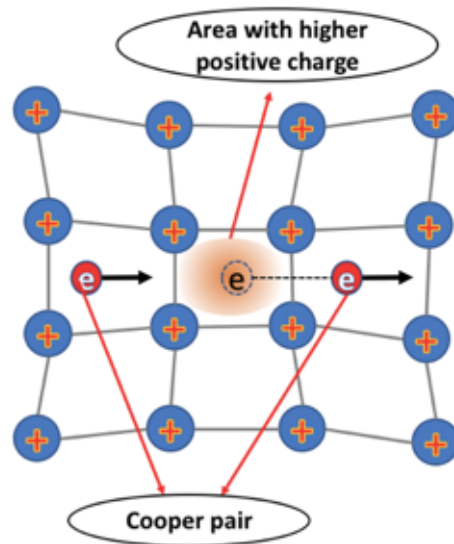


Figure 1.2: The formation of the Cooper pair in conduction process of superconductivity.

## 1.2 Basic properties of high- $T_c$ superconductor

In addition to zero resistivity, another basic property of superconductivity is that the response of superconductor to weak external magnetic field. The superconductor expels the external magnetic field which is known as the Meissner effect. The illustration of the Meissner effect is shown in the Fig. 1.4. A piece of superconductor is placed in a weak external magnetic field. In the normal state,  $T > T_c$ , the magnetic fields penetrate the superconductor. If the temperature is lowering until  $T > T_c$ , the weak external magnetic field is expelled. The magnetic field is zero inside the superconductor.

The  $B = 0$  inside the superconductor, the Meissner effect, is a results of screening current in the surface of superconductor which produce magnetic field equal to the external fields in the opposite direction. Based on the respond the external field, the superconductor is classified in two class as follows:

1. Type I superconductor: The magnetic field inside the superconductor remain zero until superconductivity is destroyed by the external field. The value of external fields that can destroy the superconductivity is known as critical fields.
2. Type II superconductor: In this type, there are two critical fields, the upper critical field ( $H_{c1}$ ) and the upper critical field ( $H_{c2}$ ). In the external field lower than  $H_{c1}$ , the magnetic field inside the sample is zero as the type 1 and the superconductivity is destroyed at the external field is greater than  $H_{c2}$ . In the range external field between  $H_{c1}$  and  $H_{c2}$ , the external field penetrate the superconductor in the form of vortices.

The illustration of the respond of the type I and type II superconductor to the external magnetic field are given in the Fig. 1.5. The first theory to explain the Meissner effect was

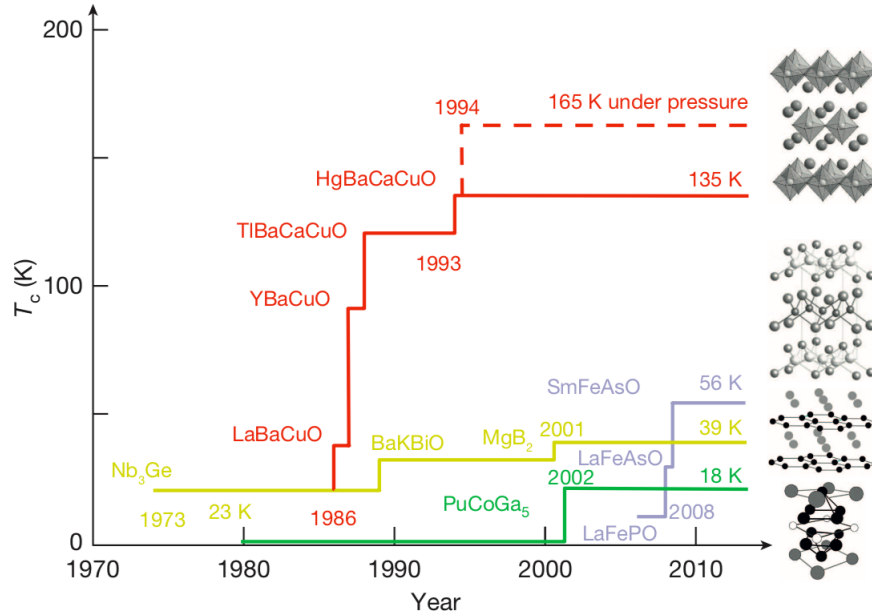


Figure 1.3:  $T_c$  versus time for various classes of superconductor. adapted from [5]

formulated by F. London and H. London[9]. Their theory based on the two fluid model in which some fraction of the electron in the superconducting state which move without resistance,  $n_s$ , and the other electron in the normal state which move with resistance,  $n_n$ . The derivation of this model leads to the formulation of the relation of the electrical current density inside superconductor,  $\mathbf{j}$ , with the magnetic vector potential,  $\mathbf{A}$ . This formulation is well known as **London equation**.

$$\mathbf{j} = -\frac{n_s e^2}{m_e} \mathbf{A} \quad (1.4)$$

This equation was also successfully derived from the microscopic quantum theory of superconductor, 20 years later since it was firstly formulated by Bardeen, Cooper, and Schrieffer. From the London equation, we can get the magnetic field distribution inside the superconductor as follow :

$$\nabla^2 \mathbf{B} = \frac{\mathbf{B}}{\lambda_L^2} \quad (1.5)$$

What we can understand from this equation is that the magnetic fields inside the superconductor is not uniform. the magnetic fields is exponentially damped which maximum value in the surface as shown in the Fig. 1.6. The  $\lambda_L$  is measure the depth of penetration of the external magnetic field and known as **London penetration depth** which is

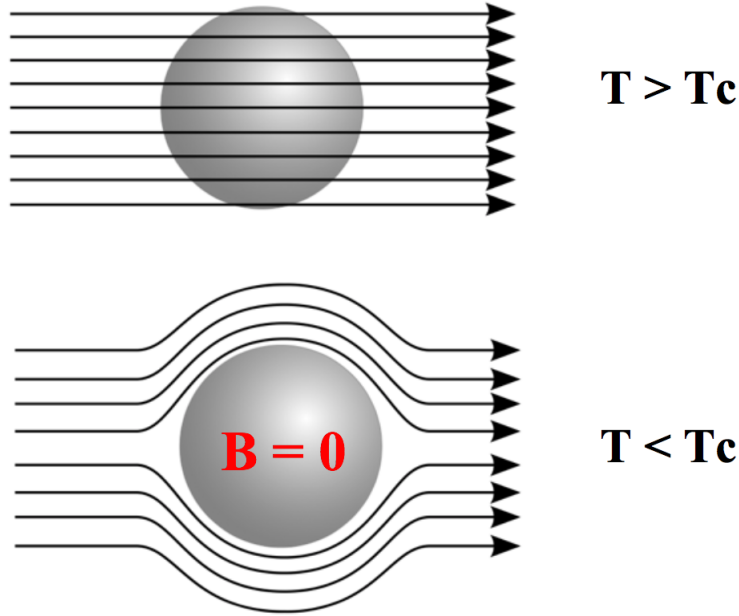


Figure 1.4: The illustration of Meissner effect. The external magnetic field are expelled from the specimen in the superconducting state.

formulated as follow:

$$\lambda_L = \left( \frac{m_e}{\mu_0 n_s e^2} \right)^{\frac{1}{2}} \quad (1.6)$$

In addition to the  $\lambda_L$ , other fundamental length scale that characterize the superconductor is so called **coherence length**  $\xi$ . The  $\xi$  is related to spatial variations in the superconducting order parameters. The theory to describe  $\xi$  is formulated by **Ginzburg-Landau** and **BCS** theory which explains the nature of interface between normal and superconducting phase. The **BCS** theory gives:

$$\xi_0 = \frac{2\hbar v_F}{\pi \Delta} \quad (1.7)$$

The  $v_F$  is the electron velocity at the Fermi surface which increase with the carrier density and  $\Delta$  is superconducting energy gap which related to the binding energy of Cooper pair and in BCS theory  $2\Delta = 3.5T_c$ . The superconductor with high electron density such as Al have long coherence length and the superconductor with low electron density such as  $\text{YBa}_2\text{Cu}_3\text{O}_7$  has short coherence length.

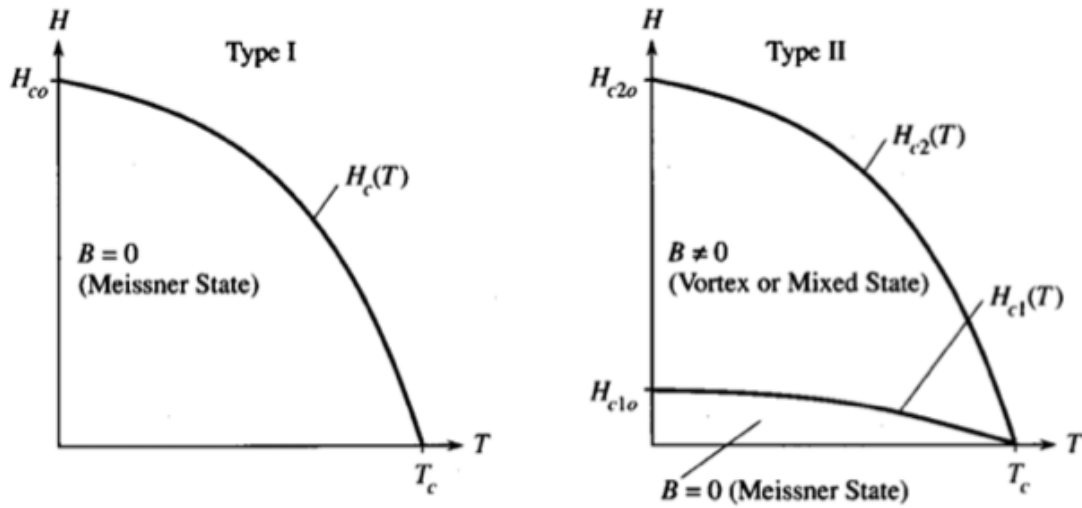


Figure 1.5: The magnetic phase diagram for type I and type II superconductor.

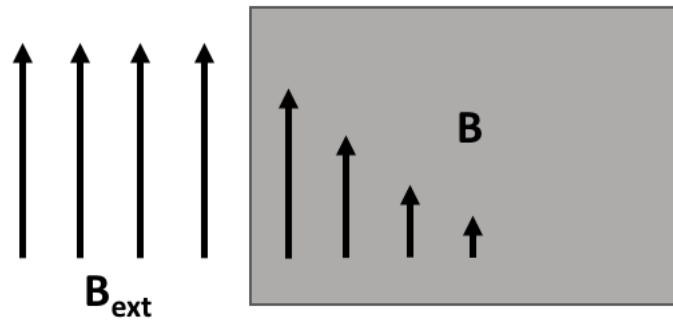


Figure 1.6: The illustration of London penetration depth.

### 1.3 The phase diagram of high- $T_c$ superconductor

The first insight to understand the nature of the high- $T_c$  is to look the detail of the phase diagram. The combination of the some experimental technique was used to construct the phase diagram of the high- $T_c$  superconductors. The typical phase diagram of high- $T_c$  cuprates is shown in Fig. 1.7. The mother compound of the high- $T_c$  cuprates,  $\text{La}_2\text{CuO}_4$  and  $\text{YBa}_2\text{Cu}_3\text{O}_6$ , shows the long range antiferromagnetic ordering and well known as Mott insulator. The  $\text{CuO}_2$  plane is play crucial role in the magnetic properties of the cuprates high- $T_c$ . In a Mott insulator, the on-site coulumb repulsion is strong enough to localize electron at  $\text{Cu}^{2+}$  site which has spin  $1/2$ . The antiferromagnetic long-range ordering arise from superexchange interaction between localized  $\text{Cu}^{2+}$  spins mediated by planar oxygen with  $J \sim 1500$  K [10].

The electron or hole doping into  $\text{CuO}_2$  plane partially destroy the long range AF ordering and superconductivity emergent. The hole concentration at which  $T_c$  has maximum

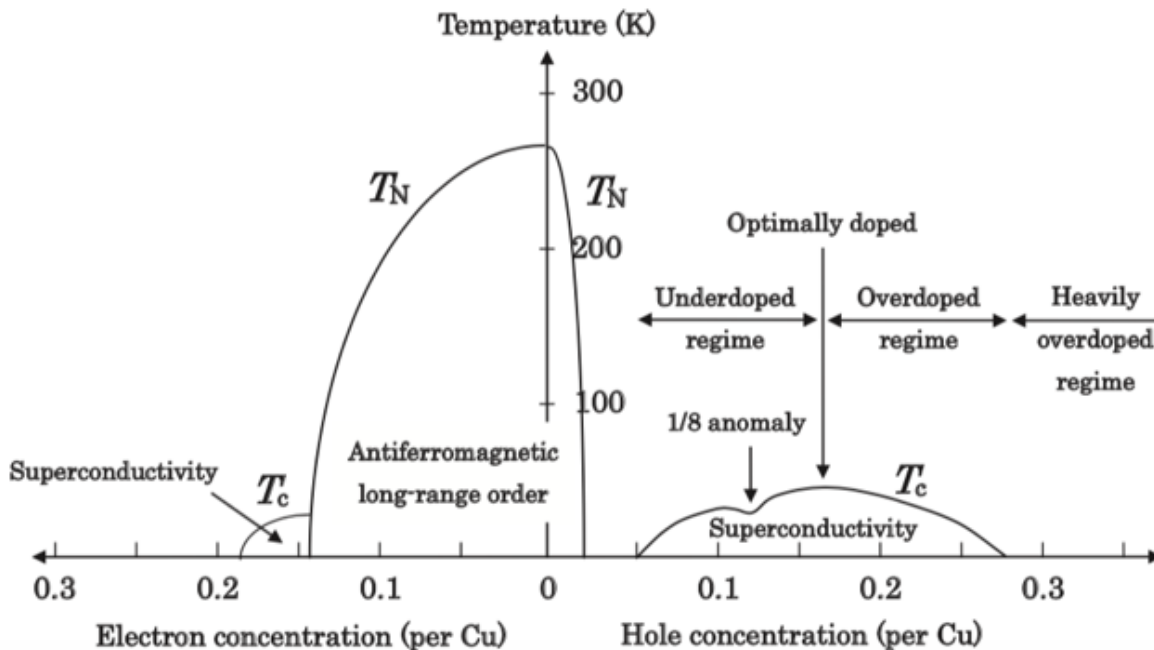


Figure 1.7: Typical phase diagram of high- $T_c$  cuprates.  $T_c$  and  $T_N$  are the superconducting transition temperature and Néel temperature, respectively. Adapted from [10].

value is known as optimally doped. The hole concentration below optimally doped is marked as underdoped regime and the hole concentration over the optimally doped is marked as overdoped regime. The anomaly suppression of  $T_c$  occurs at hole concentration per Cu =  $1/8$  which is originated from the inhomogeneous spin and charge ordering and known as "stripe".

It is well known the superconductivity in conventional superconductivity arises from the attraction between electrons and form "Cooper pair", while in high- $T_c$  cuprates the mother compound shows AF long-range ordering as results from the strong electron repulsion. It is still debatable whether the magnetism mediates the electron pairing in the high- $T_c$  cuprates or just competes with the superconductivity. Over the past 30 years, the magnetic properties of high- $T_c$  cuprates have been studied extensively in both theoretically and experimentally in order to get detail understanding of the nature of superconductivity.

## 1.4 The magnetic properties of the $\text{YBa}_2\text{Cu}_3\text{O}_6$

Looking at detail of the phase diagram of the cuprates, it is shown that that antiferromagnetic order in close proximity to superconductors. Thus the detail understanding of the electronic and magnetic state of the antiferromagnetic phase is one of the key to understand the nature of the superconductivity. The first evidence the long-range AF ordering in  $\text{YBa}_2\text{Cu}_3\text{O}_{6.2}$  which is the nearly mother compound of  $\text{YBa}_2\text{Cu}_3\text{O}_{6+x}$  was given by  $\mu\text{SR}$  as shown in the Fig. 1.8. The oscillation appears at 250 K which indicates the formation

of long range magnetic ordering. At 15 K, the oscillation become clear. From this experimental results, we can deduced the  $T_N$  to be  $\sim 250$  K mostly muon sense internal fields around  $250 \sim 300$  G [11].

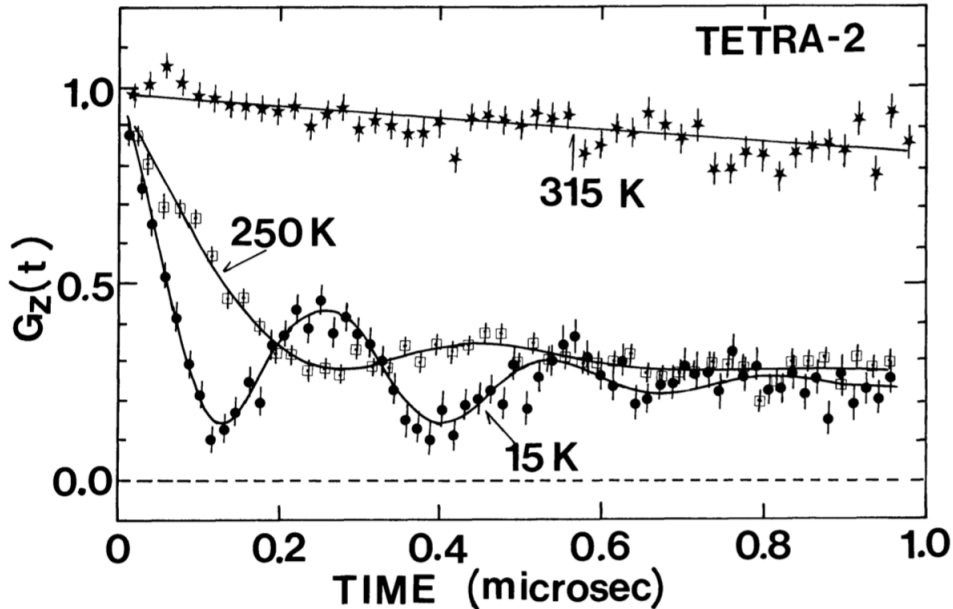


Figure 1.8:  $\mu$ SR spectra of  $\text{YBa}_2\text{Cu}_3\text{O}_{6.2}$  at 315 K, 250 K, and 15 K. Adapted from [11].

Another  $\mu$ SR experiment on  $\text{YBa}_2\text{Cu}_3\text{O}_{6+x}$  shows that the internal field at the muon sites is unchanged with increasing  $x$  up to  $x = 0.30$  and then rapidly decrease after  $x = 0.44$  as shown in the Fig. 1.9 [12]. This result gave the clear evidence of the destroyed the static magnetic ordering by hole doping at which superconductivity appears.

The neutron diffraction also found that the existence the long-range magnetic ordering in  $\text{YBa}_2\text{Cu}_3\text{O}_6$ . It has been found that the antiferromagnetic observed by neutron only in tetragonal phase, nonsuperconducting phase ( $x \lesssim 0.4$ ) [13, 14]. The proposed magnetic structure is given in the Fig. 1.10. For the simplicity, only copper atoms are drawn. cross-hatched circles represent nonmagnetic  $\text{Cu}^{+1}$  ( $\text{Cu(I)}$ ) ions, while solid and open circles indicate antiparallel spins at  $\text{Cu}^{+2}$  ( $\text{Cu(II)}$ ) sites. The oxygen atom located at the middle of the solid line which connected between two Cu ions. A series study neutron diffraction studies determine a maximum Néel temperature  $\sim 500$  K with average ordered magnetic moment  $(0.66 \pm 0.07)\mu_B$  per Cu atoms at  $x \approx 0$  [13]. The spin direction is determined to be perpendicular to the  $c$ -axis, but the direction in the  $a - b$  plane could not be determined. The magnetic order between two  $\text{CuO}_2$  layers, layer (a) and (c) in the Fig. 1.10, has antiferromagnetic ordering. In the  $\text{CuO}$  layer, layer (b) in the Fig. 1.10, there is no magnetic ordering. This AF ordering in  $\text{CuO}_2$  plane arise from the superexchange interaction between Cu ions via oxygen with  $J \sim 1500$  K [10]. The antiparallel spin direction of Cu ions with next nearest Cu ion in  $\text{CuO}_2$  plane implies that the magnetic unit cell volume is double of chemical unit cell as shown in the Fig. 1.11.

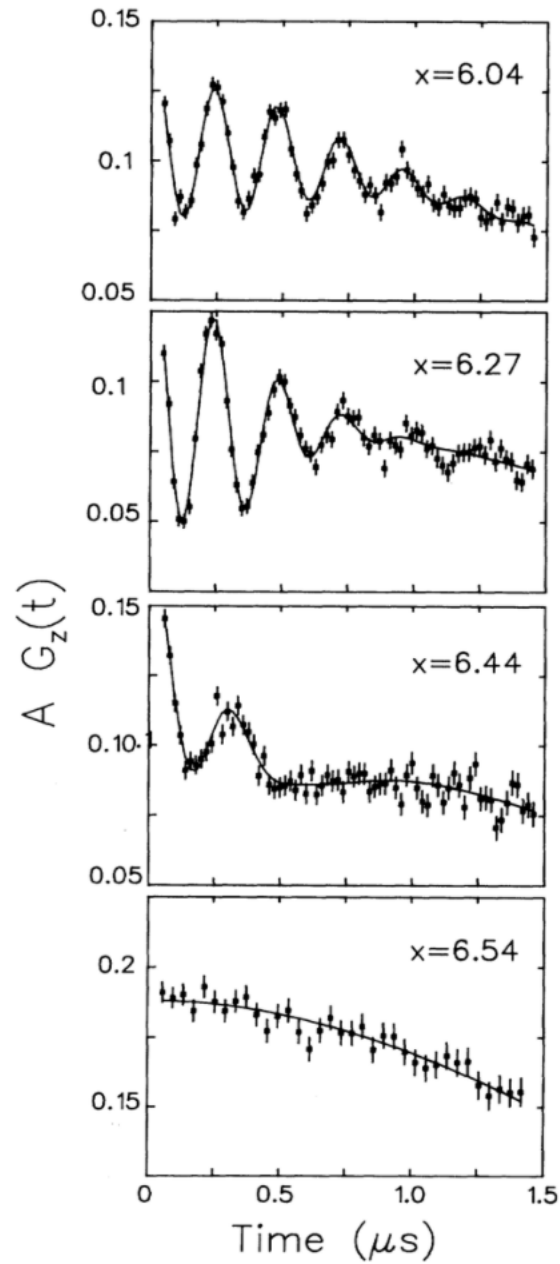


Figure 1.9: The zero-field  $\mu\text{SR}$  time spectra of  $\text{YBa}_2\text{Cu}_3\text{O}_x$  at 20 mK in all cases except for  $x = 6.04$  for which  $T = 90\text{mK}$ . Adapted from [12].



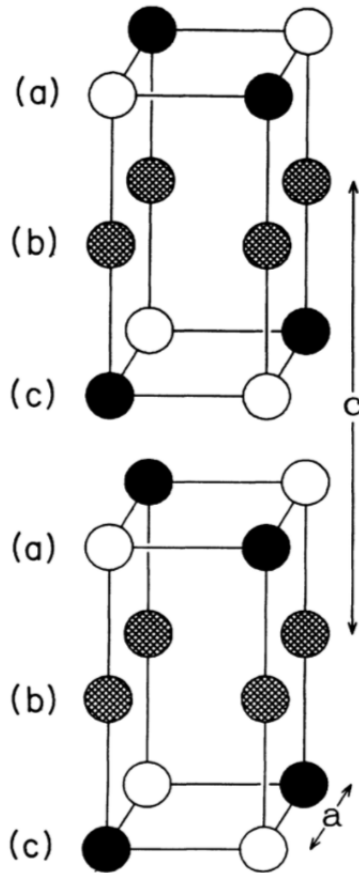


Figure 1.10: Proposed magnetic structure from the neutron diffraction for  $\text{YBa}_2\text{Cu}_3\text{O}_{6+x}$  with  $x \sim 0$ . The black and white circle indicate antiparallel spin ordering of  $\text{Cu}^{2+}$  and cross hatched indicates the non magnetic  $\text{Cu}^{1+}$ . Adopted from [13].

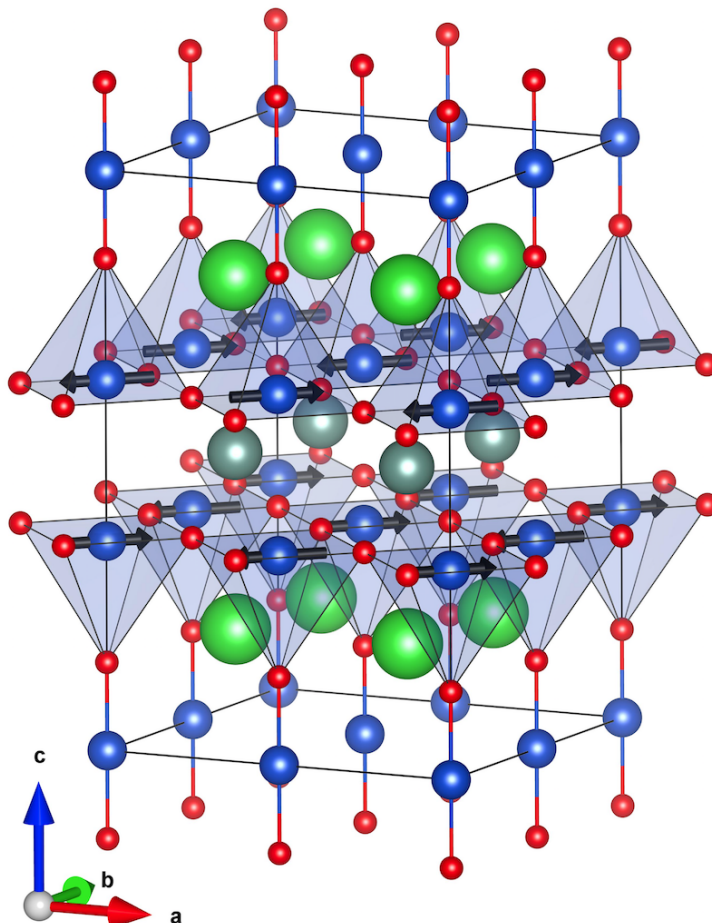


Figure 1.11: The magnetic unit cell of  $\text{YBa}_2\text{Cu}_3\text{O}_6$  which has size  $2 \times 2 \times 1$  conventional unit cell.

As mention above, two fundamental length scale in the superconductor are london penetration depth  $\lambda_L$  and coherence length  $\xi$ . Since moun is local probe and the depth implanted muon can be tuning by changing the energy of implanted muon, we can get the profile of external magnetic penetration depth from a series of experiments. In the limit where london penetration depth  $\lambda_L$  is much larger than the coherence length  $\xi_0$  and the mean free path of electron in the normal state  $l \gg \xi_0$ , If a magnetic field applied parallel to the surface of the superconducting slab decays with depth  $z$  according to the following equation [15]:

$$B(z) = B_0 e^{-z/\lambda_L} \quad (1.8)$$

In this equation  $\lambda_L$  is average of penetration depth. From the  $\mu\text{SR}$  experiment, the measurement of fundamental lenght  $\lambda$  which is related to the  $n_s/m^*$  ( $n_s$  is superconducting carrier density and  $m^*$  is effective mass). A series of  $\mu\text{SR}$  experiment which was done by Uemura, et. al has found the universal relation between  $T_c$  and relaxation rate,  $\sigma$  as shown

in the Fig. 1.12. The relation between the relaxation rate and  $n_s/m^*$  as follows [16]:

$$\sigma \propto 1/\lambda \propto n_s/m^* \quad (1.9)$$

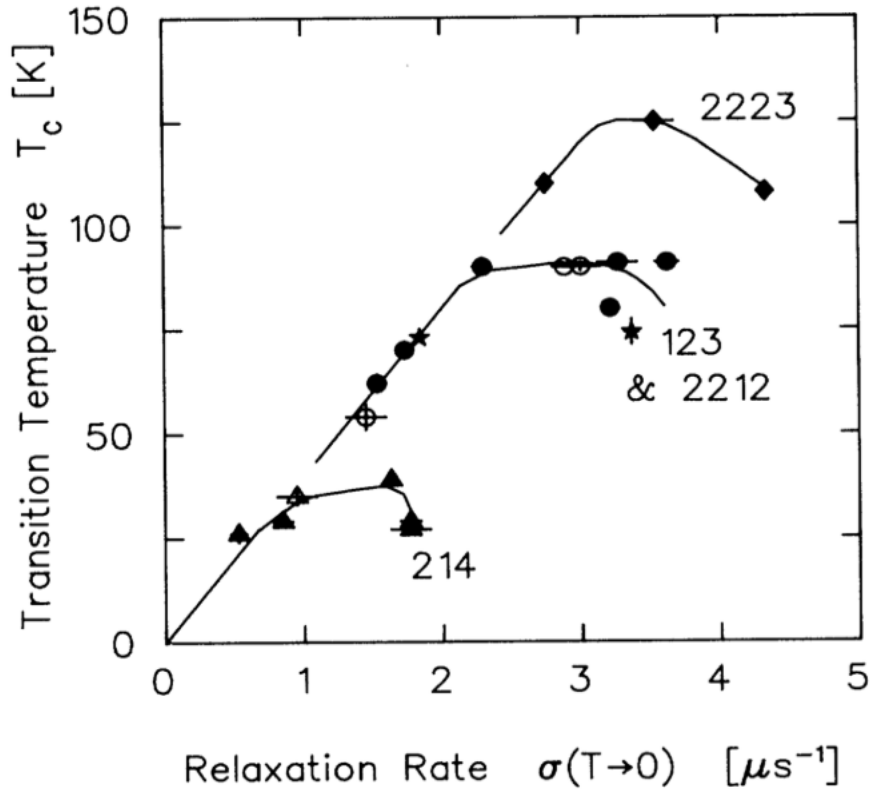


Figure 1.12: The universal relation between  $T_c$  and relaxation rate. Adapted from [16].

The transverse-field  $\mu$ SR measurements of the magnetic penetration depth  $\lambda_L$  in  $ab$  plane of the  $YBa_2Cu_3O_{6.95}$  is shown in the Fig. 1.13. From these results, the  $\lambda_{ab}$  has linear  $T$  dependence at low external magnetic field  $H$  and low  $T$  which corresponds to the  $d_{x^2-y^2}$ -wave superconductor energy gap. These results provided the early evidence for unconventional  $d$ -wave pairing of charge carriers in the vortex state of high- $T_c$  superconductors, which not compatible with the BCS theory.

The precise  $\mu$ SR experiment reported the coexistence the short -range magnetic ordering at low temperature which is called freezing temperature  $T_f$  in Y-based and La-based high- $T_c$  cuprates as shown in the Fig. 1.14. [18, 19, 20].

The close proximity between magnetism and superconductivity implies that the theories considering spin fluctuation is the leading theories to explain the superconductivity.

Although lots of  $\mu$ SR experimental results have been built up to study high- $T_c$  superconductors, the unknown muon stopping sites and the muon perturbation to the host system prevents us from achieving more advanced knowledge on the intrinsic properties magnetic

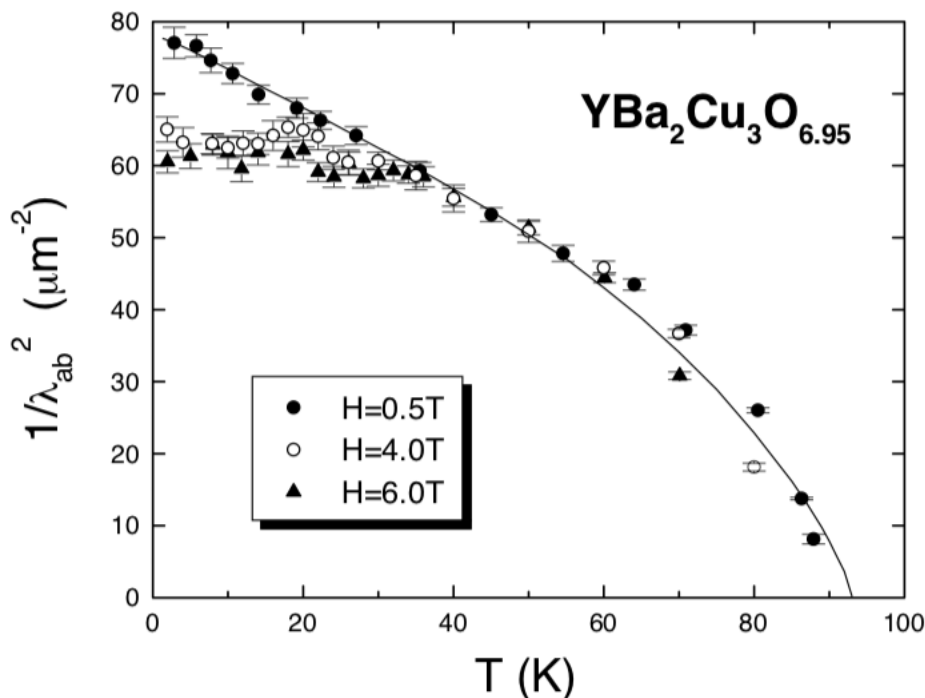


Figure 1.13: The TF- $\mu$ SR measurements of the vortex state of the high- $T_c$ . Adapted from [17].

and electronic state of the system. As described above, even though the  $\text{YBa}_2\text{Cu}_3\text{O}_6$  is well studied by  $\mu$ SR, the muon site in this system is still a puzzle. Especially in describing the complete behaviour of muon in this system and theoretical calculation of the internal fields that muon senses.

## 1.5 The muon-site problem

The main information from  $\mu$ SR experiment is internal fields at the muon site. The detailed analysis of the Fourier transform of zero field- $\mu$ SR time spectra of  $\text{YBa}_2\text{Cu}_3\text{O}_{6.2}$  and  $\text{YBa}_2\text{Cu}_3\text{O}_{6.3}$  as shown in Fig. 1.15, the muon spin precesses with a frequency of about 4 MHz, which corresponds to an internal field of about 300 G, and a broad peak around 1~2 MHz, which corresponds to an internal field of 80~150 G [21]. These experimental results require theoretical justification of the muon sites and related internal fields.

The early attempt to reveal the muon site in  $\text{YBCO}_6$  has already been done since the early days of high- $T_c$ . N. Nishida *et al.* [21] tried to explain the internal field induced by antiferromagnetic ordering of Cu 3d-moment by dipolar field calculations. This calculation is based on the point dipole model, ionic picture of magnetism, where the magnetic moment resides in the particular ion. In this case, spins reside at Cu sites. The

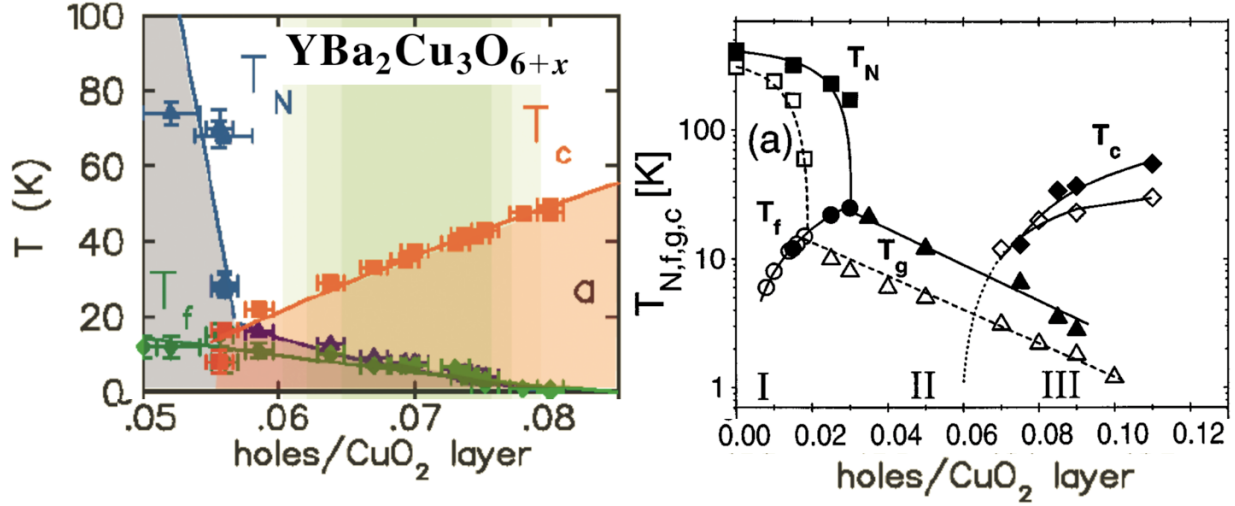


Figure 1.14: The coexistence of the short-range magnetic ordering in both Y-based and La-based high- $T_c$  cuprates. Adapted from [18, 19].

magnitude of the Cu moment as determined from the neutron diffraction but the direction was determined from the calculations. The proposed muon sites on the basis of this calculation is given in the Fig. 1.16. As mentioned above, the muons in  $\text{YBa}_2\text{Cu}_3\text{O}_6$  feel an internal field  $\sim 300$  G. The corresponding muon site is the  $b$ -site, which is located in the  $a$ - $c$  plane and about  $1 \text{ \AA}$  from the apical oxygen. The dipolar scanning yielded an internal field of 200 to 300 G. The magnetic moment direction was set to be parallel to the  $a$  axis [21].

The dipolar field scanning was also done by Weber *et al.* This dipolar scanning was restricted to the  $\mu$  distance to Oxygen to vary from  $0.9 \text{ \AA}$  to  $1 \text{ \AA}$  as shown in the Fig. 1.17, which is marked with a black dot. The calculation results show that an internal value of  $\sim 300$  G is only obtained if the magnetic moment direction is assumed to be aligned along  $\langle 110 \rangle$ , which is contradictory to the Nishida *et al.* results [22].

The combination of dipolar field simulation with electrostatic potential was done by Q. Li *et al.* [23]. The potential calculation was done on the basis of a Morse-like potential with the form:

$$V_M(r) = \frac{Q}{r} + \frac{|Q|}{r_0} e^{(10-25r[\text{\AA}])} \quad (1.10)$$

where  $Q$  is the valence of the ion and  $r_0$  is the ion's hard core radius. The attractive Coulomb potential is given in the first term, and the repulsive hard-core potential is given in the second term. The potential calculation was done around the oxygen site with the assumption that the muon will be located around  $1 \text{ \AA}$  from the oxygen. The dipolar field scanning was also done in the same location. The coincidence between the minimum potential and the internal field of  $\sim 300$  G is regarded as a candidate muon site in  $\text{YBa}_2\text{Cu}_3\text{O}_6$ . Another local minimum potential was also found in the same calculation but cannot be explained by internal fields from the experiment. The limitation of computational resources and technique was a prevent

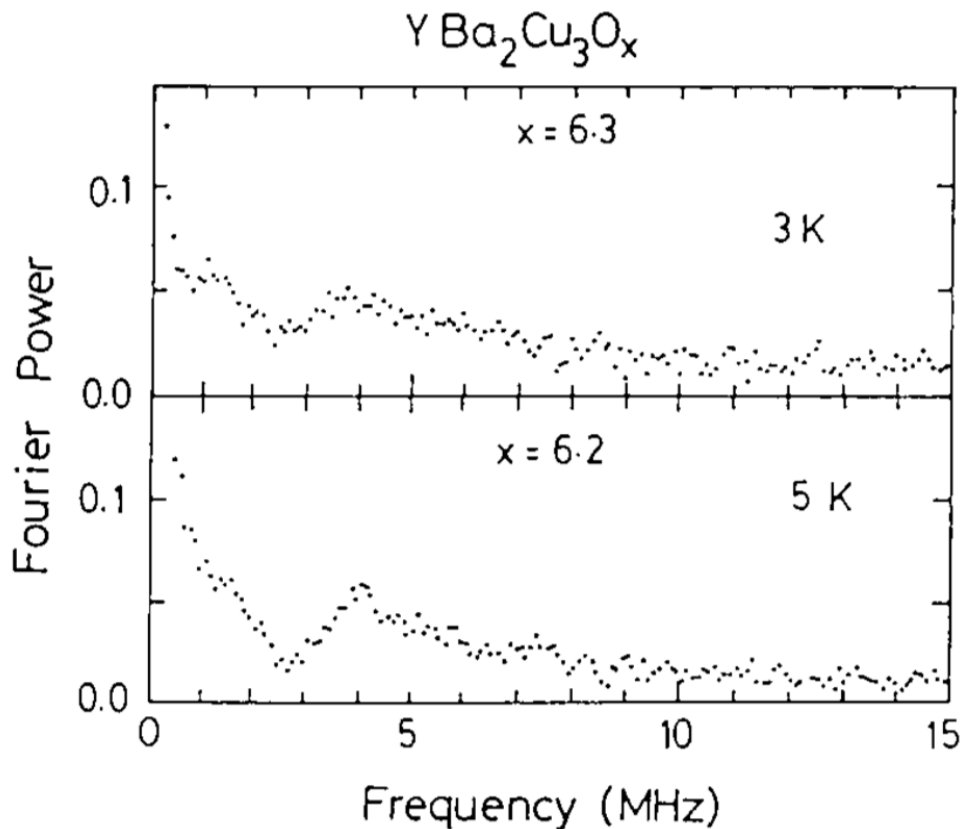


Figure 1.15: Fourier transform of the zero field- $\mu$ SR time spectra of  $\text{YBa}_2\text{Cu}_3\text{O}_{6.2}$  and  $\text{YBa}_2\text{Cu}_3\text{O}_{6.3}$ . Adapted from [21].

this attempt to get the realistic electrostatic map inside the sample.

Even though many attempts to reveal muon site and explain the electronic state in  $\text{YBCO}_6$ , there is no comprehensive description of the muon state in the system. The quantitative information about the muon perturbation to the host system is also the main problem in the muon site estimation which cannot be captured in the previous calculation especially in  $\text{YBCO}_6$  system due to the limitation of calculation technique and computer power.

Nowadays, the utilize of density functional theory (DFT) become trend to search muon stopping site. The fast development of supercomputing power triggers this research field. The DFT technique is known to have great success in studying electronic structure of solid which provide insights in to properties of solid. The DFT calculation is unable to give correct electronic structure for the strongly correlated system. The  $\text{YBCO}_6$  is well known as a Mott insulator which its insulator behavior caused by strong correlated between electron. The Hubbard  $U$  is needed to add in the Hamiltonian in order to accommodate the strong correlation effect, DFT+ $U$  [24, 25]. The detail description of the DFT+ $U$  implementation is given in the chapter 3.

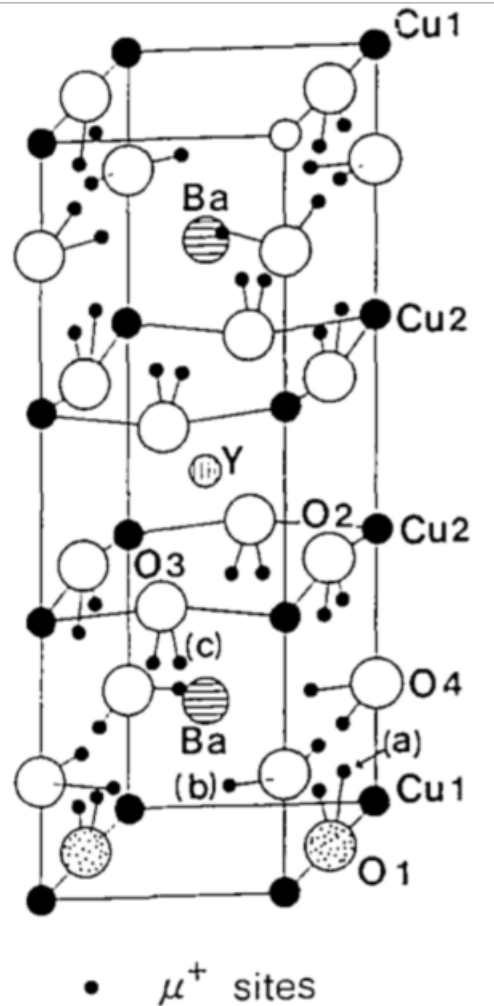


Figure 1.16: The proposed muon sites from dipolar field scanning. Adapted from [21].

Two distinct approaches for initial muon site identification on the basis of DFT calculations:

1. Place muon in the randomly chosen low-symmetry site [26, 27, 28]. This approach argues that the identification of the local minimal potential is not an accurate method to investigate the muon site due to the zero point energy (ZPE) vibration which is the energy of the muon in the ground state. Due to the ZPE, muon will not precisely sit at the local minimum potential.
2. The muon site identification in the basis of the search for the local minimum potential. The basic assumption of this approach is that muon has a positive charge and tends to stop in the local minimum potential [29, 30]. This approach was used in this thesis. To consider the ZPE effect, the muon probability density was calculated by solving the Schrödinger equation for muon, which can quantify how much muon probability is distributed

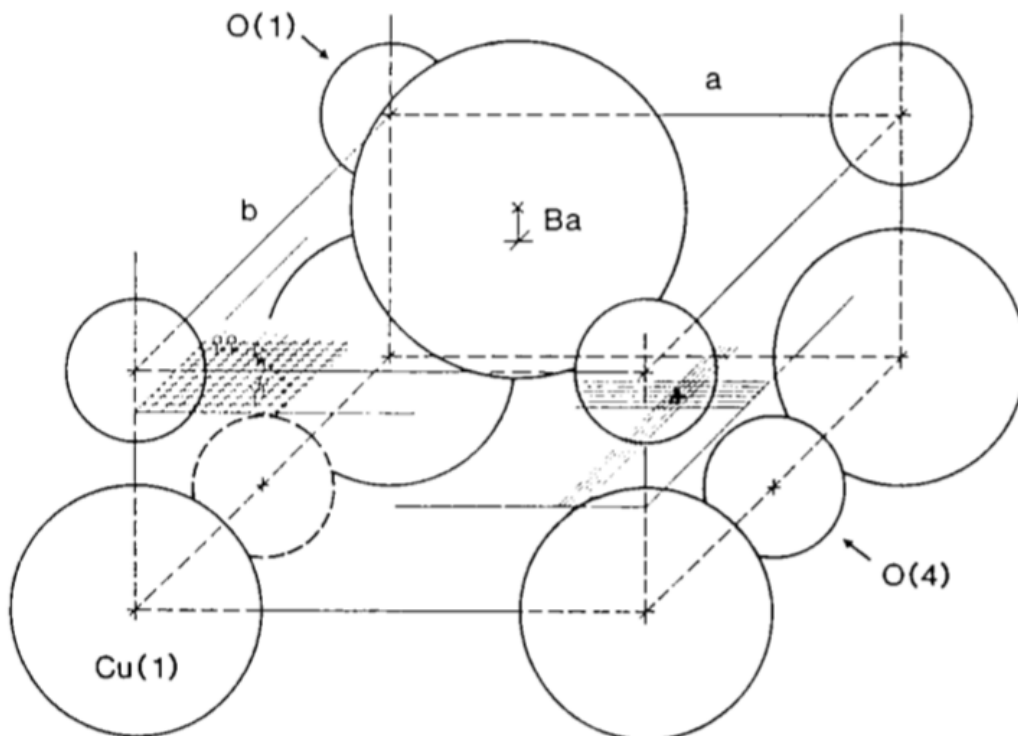


Figure 1.17: The proposed muon sites from dipolar field scanning with magnetic moment direction in  $\langle 110 \rangle$ . The dipolar scanning was done in the black dot. Adapted from [22].

around the local minimum potentials. Such as calculation was done on the basis of the toy potentials [31]. In this thesis, the potential is interpolated from the potential on the basis of the DFT calculation.

In order to address the perturbation of the muon to the local environment inside the system, the muon behaviour inside the system is modelled as hydrogen ion due to the muon has positive charge. The muon also behave as ultradilute impurity, thus the supercell approach is mandatory to simulate real experimental conditions.

The  $\mu$ SR has greatly contributed to reveal unique feature of high- $T_c$  superconductor which also contribute to the constructing the phase diagram. The knowing the implantation site and the muon perturbation to the system will be enhanced the contribution of the  $\mu$ SR in understanding the high- $T_c$  superconductivity mechanism.

## 1.6 The covalent bonding

The superexchange interaction between Cu(II) ion via oxygen play crucial role on the magnetism  $\text{YBa}_2\text{Cu}_3\text{O}_6$  which directly correspond to the nature of chemical bonding between Cu-O-Cu. The crystal fields, which is caused by electrostatic repulsion from negatively



charged electrons in the oxygen orbital, split  $3d$  orbital into two classes, the  $t_{2g}$  orbital ( $d_{xy}, d_{xz}$  and  $d_{yz}$  orbital) and the  $e_g$  ( $d_{x^2-y^2}$  and  $d_{z^2}$ ) orbitals as shown in the Fig. 1.18 [32, 33].

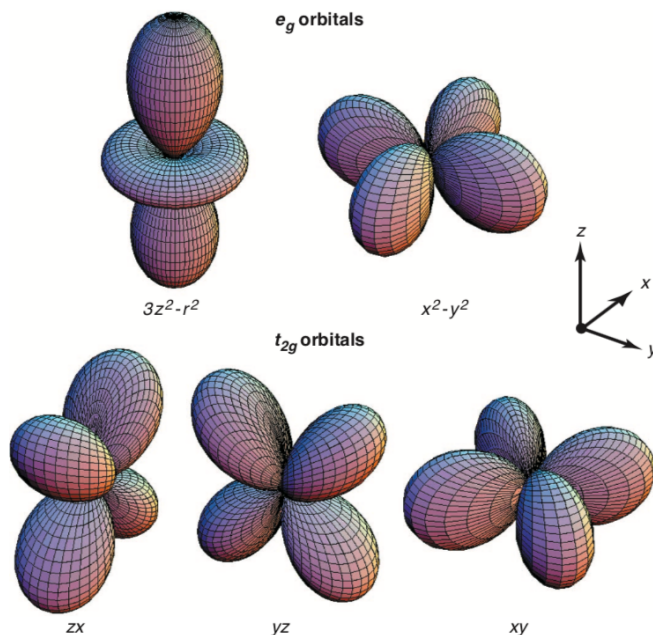


Figure 1.18: The crystal field splitting of the  $3d$  orbital. Adapted from [32].

The Jahn-Teller distortion split  $e_g$  and  $t_{2g}$  states as well as O  $2p$  states. In case  $\text{Cu}^{2+}$  states, there is one electron hole in  $d_{x^2-y^2}$ . This strong hybridization between  $3d$  orbital and  $2p$  orbital yields bonding orbital ( $\sigma$ ) and antibonding orbital ( $\sigma^*$ ) as shown in the Fig. 1.19 [34]. This orbital hybridization orbital is known as the covalency effect and can be described in first principle calculations. The systematic ARPES studies combining with first principle calculation provide strong evidence the presence the hybridization in cuprates [35] which is usually ignored in ionic picture of Cu-O-Cu bonding [36].

As  $\text{CuO}_2$  plane is central player in magnetism and superconductivity in high- $T_c$ , the covalency can not be easily ignored. The first principle calculation through density functional theory (DFT) has ability to provide the collective behaviour of the orbital and spin by including the covalency effect. This information is available in the charge and magnetization density. The calculation shows that extension of the spin in to oxygen sites as shown in the Fig. 1.20 which is successfully explained the ambiguous neutron results [37]. The extension of the spin due to the covalency effect is also observed in the NMR results [38].

The extension of the spin in the real space is contradictive with ionic picture of magnetism which is spin reside in the  $\text{Cu}^{2+}$ . The ionic picture is mainly used to confirm the internal fields from  $\mu\text{SR}$  experiment and to analyse the neutron diffraction. The neutron is difficult to sense spin at oxygen site due to the symmetry of the spin density in  $\text{YBa}_2\text{Cu}_3\text{O}_6$ .

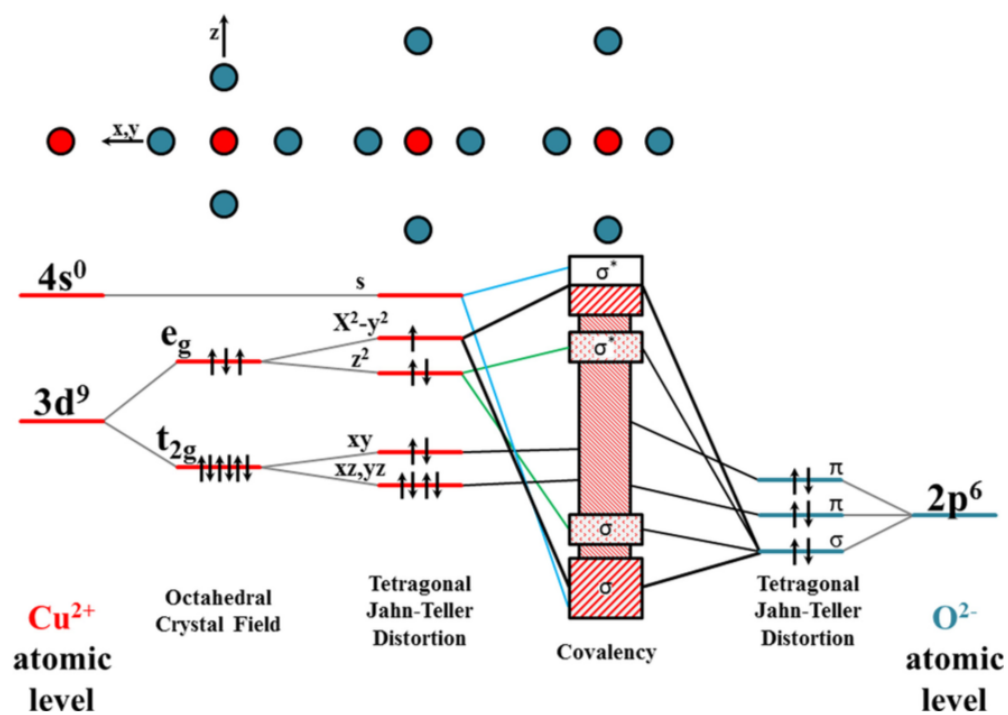


Figure 1.19: The molecular picture of the hybridization of the Cu  $3d$  orbital and O  $2p$  orbital. Adapted from [34].

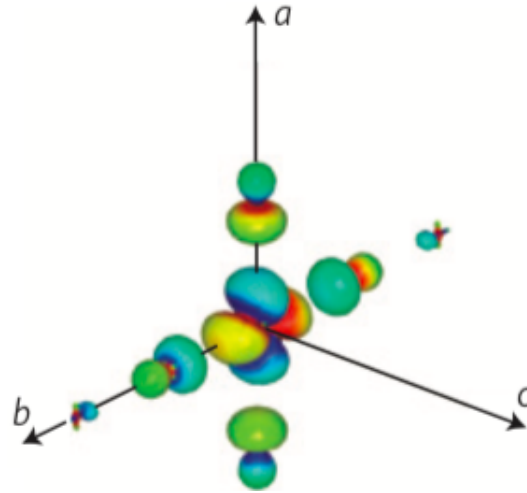


Figure 1.20: The covalently hybridized of the unpaired magnetic electron in  $\text{Sr}_2\text{CuO}_3$  obtained from the ab initio LDA + U calculation. Adapted from [37].

In this thesis, the covalency effect is carefully consider to expalin the magnetic state that interact with muons in  $\text{YBa}_2\text{Cu}_3\text{O}_6$ .

## 1.7 The thesis outline

In chapter 2 and 3 give the brief description of the  $\mu\text{SR}$  experiment technique and DFT calculation, respectively. The calculation scheme in muons site estimation by utilizing DFT is also described in chapter 3. The chapter 4 begins with the new  $\mu\text{SR}$  experimental results following the muon site identification. The band structure calculation provide the correct calculation parameter for muon site calculations. The quantify of the muon perturbation is given on the basis supercell calculation. Internal fields evaluation at muon site is carefully described with considering the muon perturbation and zero pinr energy vibration of muon. The results suggest new interpretation of the  $\mu\text{SR}$  experimental data which the covalency effect can not be easily ignored. In chapter 5, the summary and further work are given.

# Chapter 2

## The muon-spin rotation

### 2.1 The muon production and implantation process

The muon is elementary particle which can be found in nature. It exists in the cosmic ray that arrive in the sea level and a few hit people on the earth. The muon has mass 200 havier than electron, positive/negative charge and carry spin  $S = 1/2$ . It is unstable particle with a mean lifetime  $2.2 \mu s$ . Eventhough the positive and negative muon are exist, the negative muon in the matter is capture by nuclear and fall to very close orbital to the nucleus. For this reason  $\mu^+$  is more common use to study the properties of the matter. Its properties as summarize in the table 2.1. However, to use natural muon to be implanted to the sample is very difficult due to the limitation of its intensity. Instead, the intense muon can be produced artificially by using accelerator and available to study the condensed matter physics in a number place in the world.

To produce muon, the high-energy protons are bombarded in to carbon target and produce pion.



Mass, $m$	$1.8835 \times 10^{-28} \text{ kg}$ $105.66 \text{ MeV}/c^2$ $207 m_e$ $0.11 m_p$
charge, $q$	$+e$
spin, $S$	$1/2$
magnetic moment, $\mu$	$0.00488 \mu_B$
gyromagnetic ratio, $\gamma$	$135,53 \text{ MHz/T}$
mean lifetime, $\tau_\mu$	$2.19714 \mu s$

Table 2.1: The properties of the positive muon

The pion has half time 26 ns and decay to a positive muon and neutrino.



The pion has zero spin and produced at rest in the laboratory frame. Based on the conservation momentum law, the muon and neutrino must have equal momentum with opposite direction. The neutrino and muon has negative helicity in which its momentum is antiparallel with its spin [39]. From this process, 100 % spin-polarized muons are produced. Two types of  $\mu^+$ -beams are available for  $\mu$ SR experiment according to the pion momentum regimes :

**The first type** of muons are produced from  $\pi^+$  near the surface of inside production target. The muons are 100 % polarized and has energy  $\sim 4.1$  MeV. These type of muons are suitable for study the relatively thin sample due to the low momentum, 29.8 MeV/c. This type of muon is known as "surface" or "Arizona" beam.

**The second type** of muons are produced from the  $\pi^+$  which leave the production target and collected by quadrupole magnet. The typical polarization of this type of beam is less than 100 % with energy 40-50 MeV. Such beam very useful to study the sample at extreme pressure and temperature because it can overcome the cryostat.

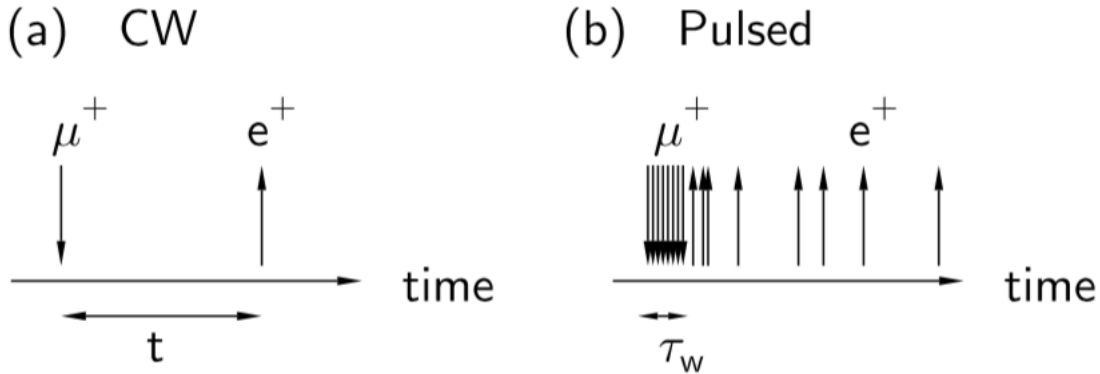


Figure 2.1: Illustration of the two types of muon beam (a) continuous wave which muons are implanted one by one and (b) pulsed which muons are implanted in a bunch.

In addition to the above classification, muon-beam is also classified based on the time structure. Two types of muon beam are available based on this classification:

**Continuous muon beam :** The muons arrive to the sample one by one continuously. The main advantage of continuous beam is that it has very good time resolution but has limitations due to the random background signal and limits the maximum incident muon rate.

**Pulsed muon beam :** The muons are bunched into pulses. Two conditions must be considered : the length of pulse must be shorter than muon's lifetime and the repetition time must be larger than the muon's lifetime. The time window for measurement up to  $10\tau_\mu$  thanks to the negligible background and the higher rate compare to the continuous beam. The time resolution is limited by the width of pulse. A pulse width 70 ns only can detect local field maximum 600 G.

The illustration of the continuous beam and pulse muon are shown in the Fig. 2.1. The continuous beam is available at TRIUMF Centre for Molecular and Materials Science Vancouver, Canada and Paul Scherrer Institut (PSI), Villigen, Switzerland. While the pulsed beam available at Rutherford Appleton Laboratory (RAL), Didcot, Oxfordshire, UK and at J-PARC in Tsukuba, Japan.

The main advantage of the muon spin resonance technique is that it is wide range material can be studied as muon can be implanted to the any material. This properties is contrast with the NMR technique which require specific nuclei. The muons are implanted with energy 4-100 MeV and rapidly thermalized very rapidly as shown in the Fig.2.2 [40].

In the thermalisation process, the muon-spin do not interact with coulombic potential and muon do not loss its polarisation. Instead the muons interact with local magnetic environment in the sample under studied.

The lifetime of muon in the sample provide unique capability to sense fluctuation rate in the range  $10^4$  to  $10^{12}$  Hz. This time window acts as bridge between NMR and neutron scattering technique as shown in the Fig. 2.3.

## 2.2 The $\mu$ SR experiment

The full polarized muons with large magnetic moment are implanted in to the sample and interact only with the magnetic environment at the muon stopping site. The muon stop in the interstitial site inside the sample at where the electrostatic potential is minimum. The muon-spin precess in the presence the magnetic fields with the angle  $\theta$  with muon-spin, Larmor precession, as illustrated in the Fig. 2.4.

The angular frequency of muon Larmor precession is given by

$$\omega = \gamma_\mu |\mathbf{B}| \quad (2.3)$$

A positive muon decay with three body process

$$\mu^+ \longrightarrow e^+ + \nu_e + \bar{\nu}_\mu \quad (2.4)$$

The emitted positron  $e^+$  direction has highest probability at direction of the muon-spin at the moment of decay. By placing two detector, backward and forward as illustrated in the Fig. 2.5 (a), we can detect the time evolution of the number of the positron. The

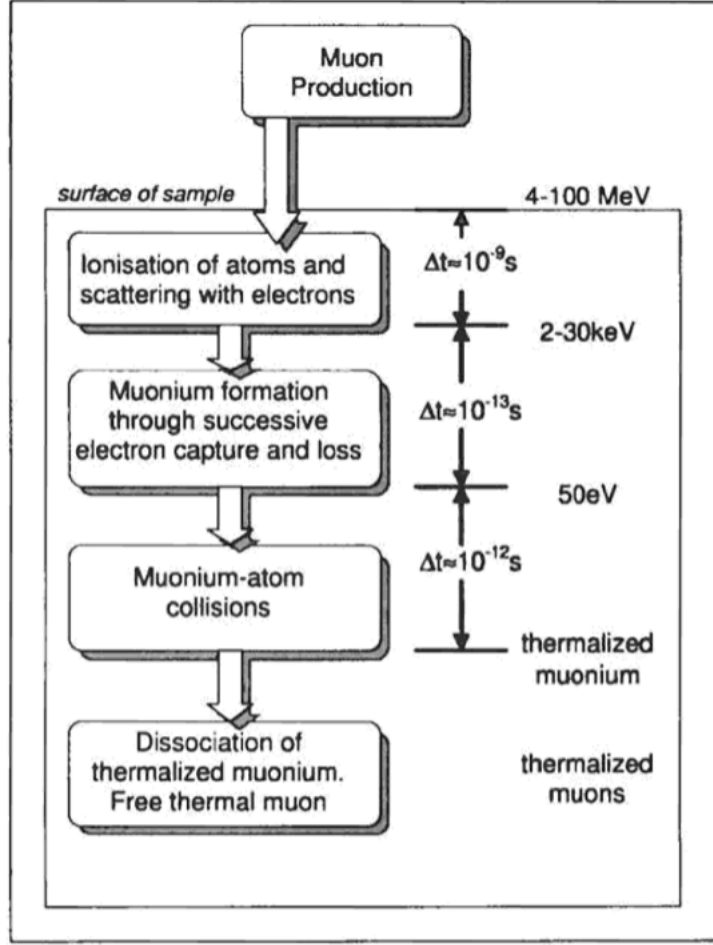


Figure 2.2: the schematic of the implantation process of the muon in the sample.

number of positron that detect by forward and backward detector as function of time is given by  $N_F(t)$  and  $N_B(t)$ ,

$$N_F(t) = N_F^0 \{ e^{-t/\tau_\mu} [1 + \tilde{A}P^{(F)}(t)] + B_0^{(F)} \} \quad (2.5)$$

$$N_B(t) = N_L^0 \{ e^{-t/\tau_\mu} [1 + \tilde{A}P^{(B)}(t)] + B_0^{(B)} \} \quad (2.6)$$

Where  $B_0$  is random background,  $N^0$  is a normalization constant,  $\tilde{A}$  is maximum precession amplitude and  $P(t)$  is the time evolution of the muon spin polarization component, which are given by

$$P^{(B)}(t) = \cos(\omega_\mu t + \theta_B) \quad (2.7)$$

$$P^{(F)}(t) = \cos(\omega_\mu t + \theta_F) \quad (2.8)$$

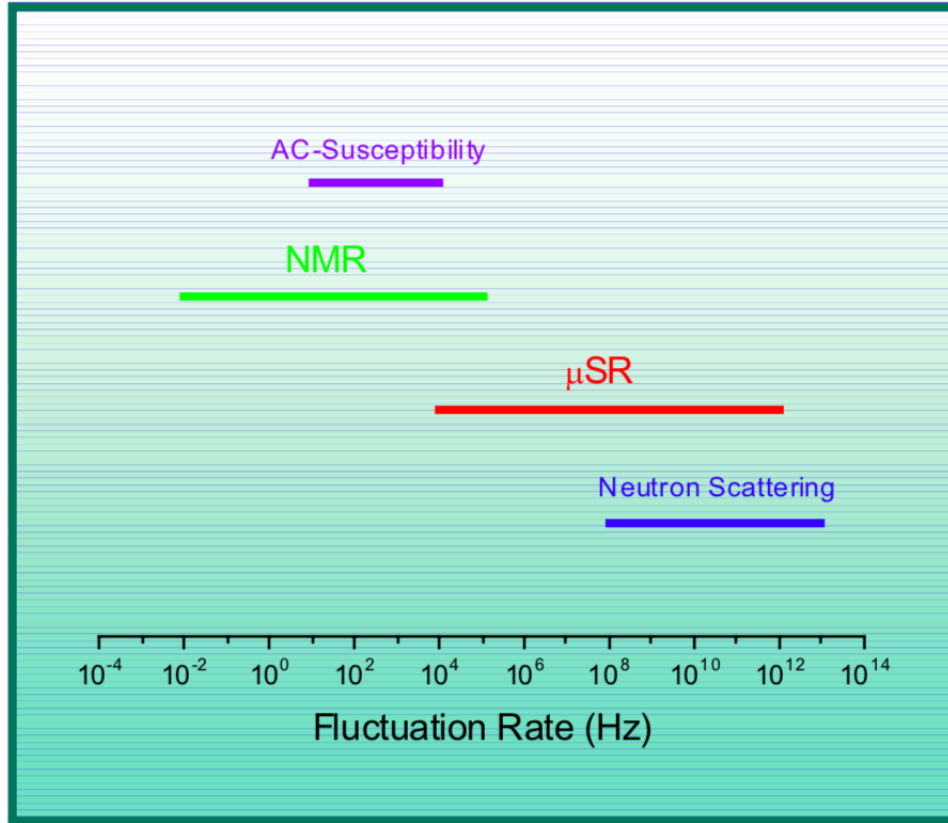


Figure 2.3: The  $\mu$ SR time window for magnetic fluctuations in materials which is complementary to other experimental techniques. Adopted from [41].

The typical signal that backward and forward detect are illustrated in the Fig 2.5 (b). The exponential dependence of the equation 2.5 and 2.6 can be removed by introducing normal difference between  $N_F(t)$  and  $N_B(t)$  which is known as symmetry function.

$$A(t) = \frac{N_B(t) - N_F(t)}{N_B(t) + N_F(t)} \quad (2.9)$$

The asymmetry function describe the time evolution of the muon-spin polarization as shown in the Fig. 2.5 (c).

In the  $\mu$ SR experiment, three possible experimental set up depend on the relative direction of the applied external field to the initial muon-spin.

- a. The first configuration is under zero external fields conditions, zero-field  $\mu$ SR. This technique is usually applied to the system with spontaneous magnetic properties.
- b. The second configuration is that applied the external field parallel to the initial muon-spin, Longitudinal field (**LF- $\mu$ SR**). This technique usually combine with the zero field to study the distribution of the internal field.



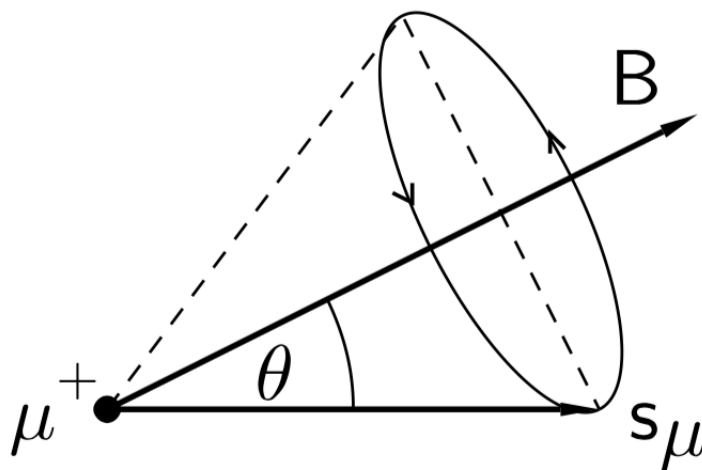


Figure 2.4: The Larmor precession of the muon in the magnetic field.

- c. The last one is that the external fields is applied in direction perpendicular with initial muon-spin, transverse field (TF- $\mu$ SR). The muon spin precess in both transverse field and internal field. This technique is very usefull to study the vortex state type-II superconductor.

Several asymmetry function can be produced from the  $\mu$ SR experiment due to the local environment at the muon stopping site in the sample :

1. In absence of the internal magnetic field, there is no polarization of the muon-spin which lead to the  $\mu$ SR time spectra as shown in the Fig. 2.6 (a).
2. When electron-spin fluctuate fast, paramagnetic state, muon cannot sense the internal field from the electron spin. Instead muon sence small nuclear dipolar field due to the very slow nuclear spin fluctuation and produces asymmetry curve as shown Fig 2.6 (b). The asymmetry function can be espressed by Kubo-Toyabe function since the muon feel random nuclear spin.
3. At low temperature, the electron spin fluctuation is slowing down. The muon sence the random and time dependent of the electron-spin ( 1000 time nuclear spin). The asymetry function of this state is shown in the Fig. 2.6 (c) where very fast muon-spin depolarisation occur. The longitudinal field recover  $A(t)$  to the unity.
4. In a system which shows the long-range magnetic ordering, muon sence large internal field and undergo Larmor precession before decay. If all implanted muon feel same internal magnetic field, single muon site, muon precess in single frequency and asymmetry become Fig. 2.6 (d). In the case more than one muon site, the damped oscillation of muon polarisation takes place as shown in the Fig. 2.6 (e).

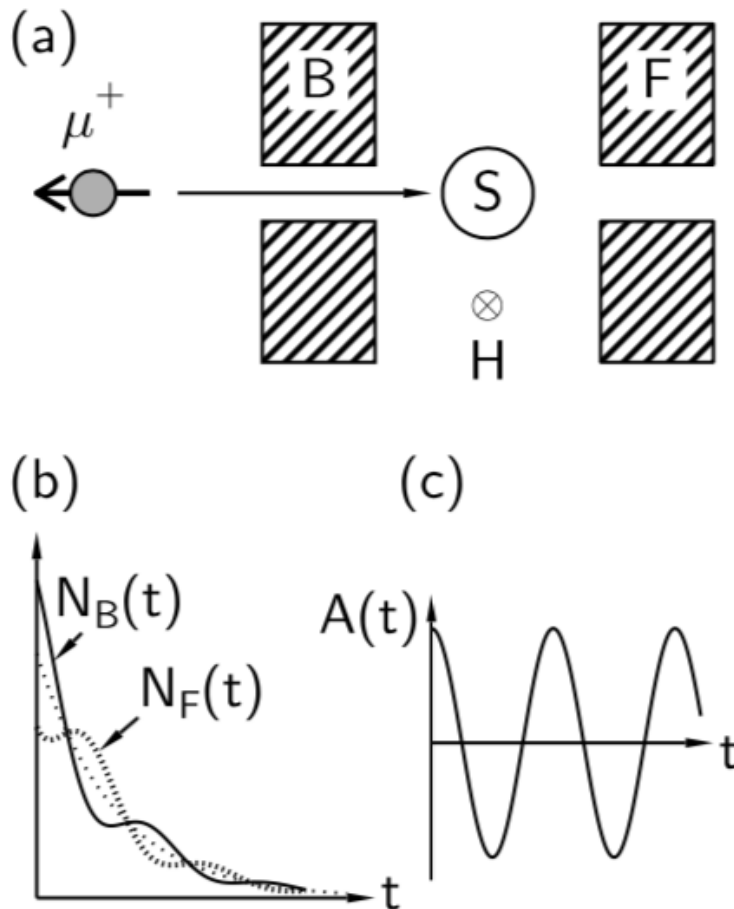


Figure 2.5: The illustration of the  $\mu$ SR experiment (a) Muons are implanted with the 100% polarisation into sample S (b) The time evolution of the number of positrons that are detected by backward and forward detector (c) Asymmetry function. Adapted from [39].

5. In a system which shows short-range magnetic ordering such as spin glass, muons feel large internal fields in random distribution. The oscillation damped rapidly and asymmetry decays rapidly to the 1/3 as shown in Fig. 2.6 (e). The 1/3 value arises from the average muon-spin polarisation due to the 1/3 of the static random fields parallel to the direction of the injected muon. The rest of the number of muons are perpendicular to the muon injection direction and precess at various frequencies.

The  $\mu$ SR is also very sensitive to distinct magnetic and non-magnetic phases in the same system. The magnetic phase is measured in the zero-field condition and the non-magnetic phase is measured in the transverse field experiment set up. The amplitude of the  $\mu$ SR signal is related to the volume fraction of the related phase in the system. A typical example is shown in Fig. 2.7 in which the magnetic ordering in  $\text{CeCu}_{2.2}\text{Si}_2$  is measured by ZF- $\mu$ SR.

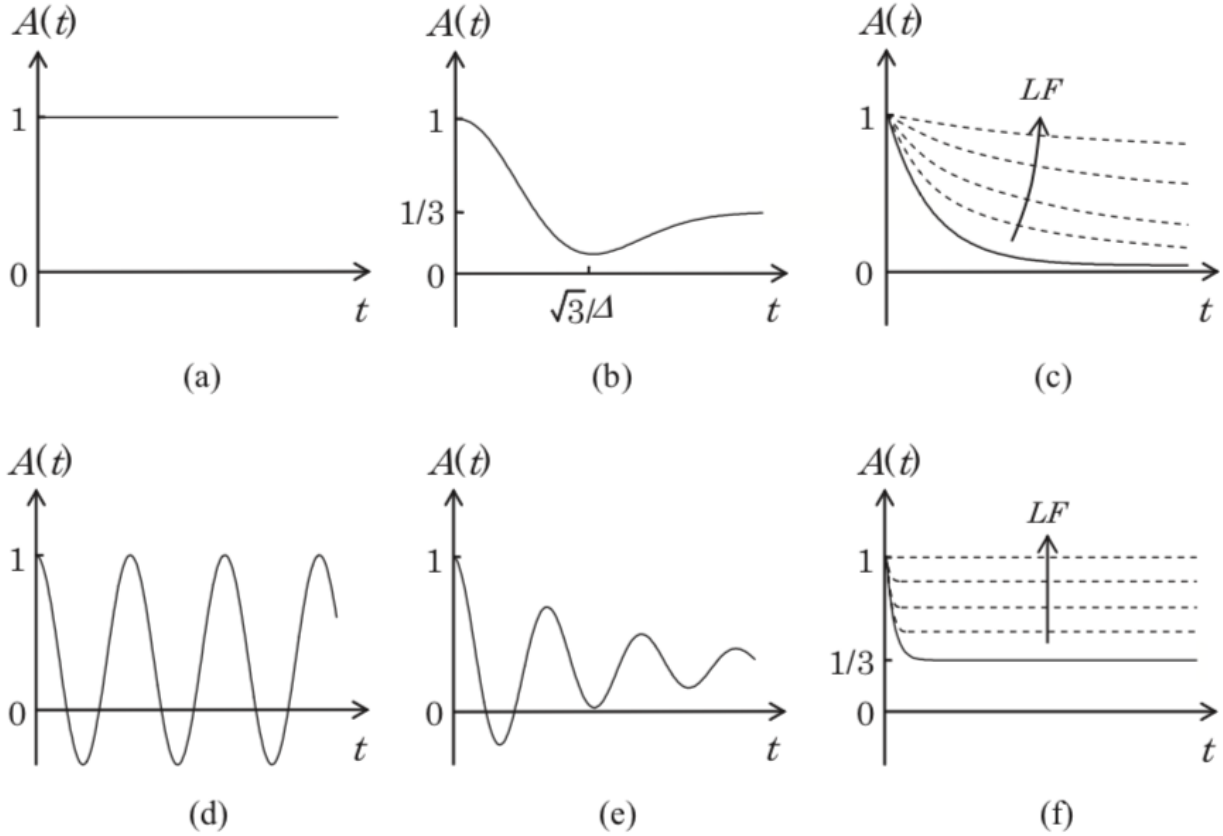


Figure 2.6: The asymmetry function (a) Paragnetic state (b) Gaussian distribution of the nuclear spin (c) Dynamic internal fields (d) Single muon site in the long range magnetic ordering (e) More than one muon site in the long range magnetic ordering (f) Random static electron-spin. Adapted from [10]

(squares) and non magnetic phase is measured by TF- $\mu$ SR (circles) [42].

The  $\mu$ SR experiment that presents in thesis using continous beam at PSI. In the experiment set up, the muon counter is installed to control the rate of the implantation muon as shown in the Fig. 2.8 (a). During the observation time window,  $\sim 10 \mu\text{s}$ , The first muon injected to the sample and the second muon is rejected by muon counter. Thus only one muon and detect one positron in observation window as illustrated in Fig. 2.8 (b) [43]. Thus, muon behave as ultradilute impurity inside the system.

### 2.3 Internal field at the muon site

The main parameter from the  $\mu$ SR experiment is local internal field which can be extrated from the muon spin polarization. The distribution of the internal field at the muon site is

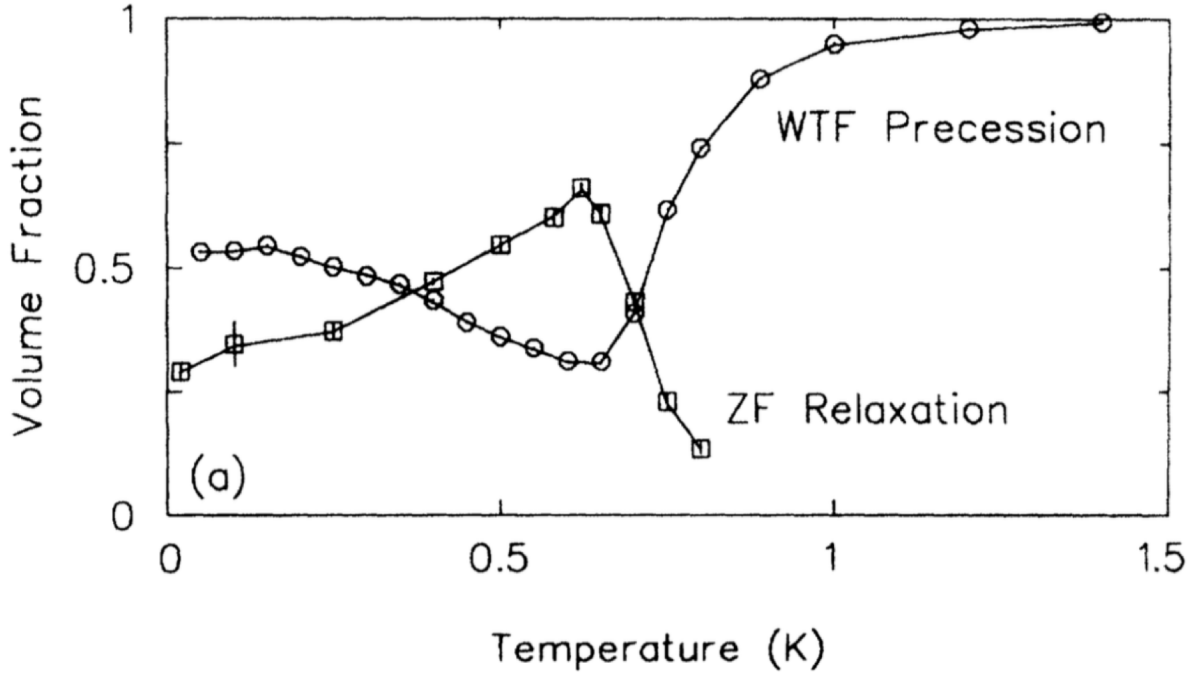


Figure 2.7: The magnetic volume fraction in  $\text{CeCu}_{2.2}\text{Si}_2$ . The squares indicate magnetic volume fraction and circles indicates non-magnetic volume fraction. Adapted from [42].

given by Fourier transform of the muon polarisation  $P(t)$ . The Fourier transform is

$$n(B) = \int_0^{\infty} \tilde{P}(t) e^{-i(\gamma_{\mu} B t + \theta)} dt \quad (2.10)$$

In order to remove the statistical noise, the Fourier transform is apodized by the gaussian function,

$$n_A(B) = \int_0^{\infty} \tilde{P}(t) e^{-i(\gamma_{\mu} B t + \theta)} e^{-\sigma_A^2 t^2 / 2} dt \quad (2.11)$$

The Fourier transform with the gaussian filter of the  $\mu\text{SR}$  time spectra in this thesis was done by using software WIMDA [44].

From the theoretical point of view, the total local magnetic field at the muon site is given by

$$\mathbf{B}_{\mu} = \mathbf{B}_a + \mathbf{B}_{dip} + \mathbf{B}_L + \mathbf{B}_{dem} + \mathbf{B}_{hyp} \quad (2.12)$$

$\mathbf{B}_a$  is applied external field.  $\mathbf{B}_L$  is Lorentz field which arise from in the evaluation of local field by constructing Lorents sphere with radius  $r_L$  from the muon site. This sphere is regarded as single magnetic domain and magnetic moment outside this sphere is contributed to the  $\mathbf{B}_L$ .  $\mathbf{B}_{dem}$  is magnetic field originated from the magnetic moment in sample surface. since this thesis focus on the study antiferromagnetic phase of  $\text{YBCO}_6$ , both  $\mathbf{B}_L$  and  $\mathbf{B}_{dem}$  vanish.

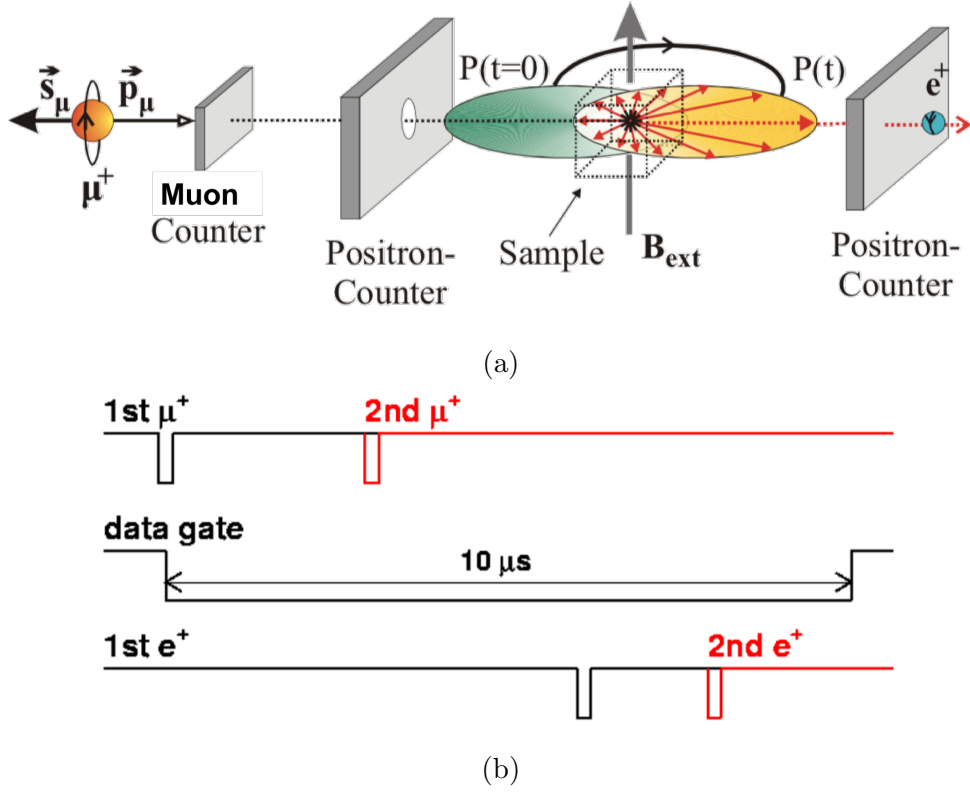


Figure 2.8: (a) The experiment set up at PSI. The muon counter is installed to control the rate of the muon and (b) The observation time window. The first muon is injected into the system and the second muon is rejected by muon counter during  $10 \mu\text{s}$ . Adapted from [43].

The  $\mathbf{B}_{hyp}$  is the contact hyperfine field which arises from overlapping muon's wavefunction with the spin density. The implanted muon in the insulator system, diamagnetic muon, the contact hyperfine  $\mathbf{B}_{hyp}$  coupling is negligible and muon causes short-range perturbation [26]. The remaining term is  $\mathbf{B}_{dip}$  which is dipolar fields arising from electron spin. Assuming a classical moment at the magnetic ion,  $\mathbf{B}_{dip}$  can be written as

$$\mathbf{B}_{dip}(r) = \frac{\mu_0}{4\pi} \sum_i \left( \frac{3\mathbf{r}_i(\mathbf{m}_i \cdot \mathbf{r}_i)}{r_i^5} - \frac{\mathbf{m}_i}{r_i^3} \right) \quad (2.13)$$

Where  $\mathbf{m}_i$  is magnetic moment of magnetic ion and  $\mathbf{r}_i$  is the distance of the magnetic ion  $i$  from the muon site.

# Chapter 3

## The density functional theory

In this chapter, I will briefly describe the density functional theory (DFT) which is the complementary tool with  $\mu$ SR experiment to get deeper understanding the magnetic properties. I discuss practical implementation to muon-site calculation and study the magnetic properties of  $\text{YBa}_2\text{Cu}_3\text{O}_6$ .

### 3.1 Many-body problem

The main heart of the quantum mechanics is Schrödinger equation which can give the microscopic behaviour electron in the system. Unfortunately Schrödinger equation can be exactly solved only in few system due the complicated electron-electron, electron-nuclei and nuclei-nuclei interaction as shown in the Fig 3.1.

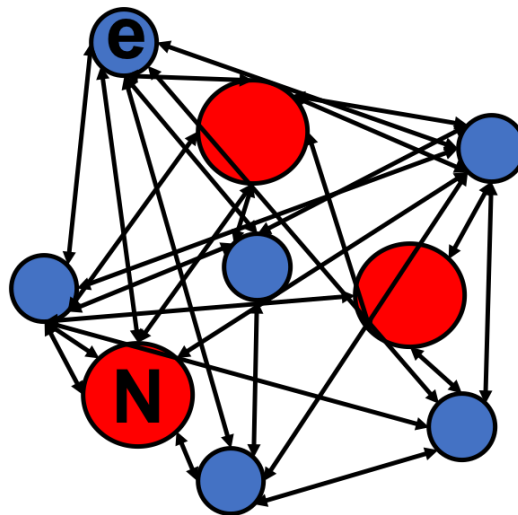


Figure 3.1: The many body interaction.

The time independent Schrödinger equation for many-body system

$$\hat{H}|\Psi\rangle = E|\Psi\rangle \quad (3.1)$$

with the hamiltonian can be expressed as

$$\hat{H} = -\sum_i \frac{\hbar^2}{2m_e} \nabla_i^2 - \sum_I \frac{\hbar^2}{2M_I} \nabla_I^2 - \sum_{i,I} \frac{Z_I e^2}{|\mathbf{r}_i - \mathbf{R}_I|} + \sum_{i \neq j} \frac{e^2}{2|\mathbf{r}_i - \mathbf{r}_j|} + \sum_{i \neq I} \frac{Z_I Z_j e^2}{2|\mathbf{R}_i - \mathbf{R}_j|} \quad (3.2)$$

The first and second term is kinetic energy of electron and nuclei, respectively. The third, fourth and fifth term are electron-nuclei, electron-electron and nuclei-nuclei interaction, respectively. Based on the fact that mass of the nuclei is much larger than mass of electron which allow us to neglect the kinetic term of the nuclei, second term. This approximation is known as Born-Oppenheimer approximation. Because, the focus study is electronic properties of the system, the hamiltonian for the electron can be written as

$$\hat{H}_e = -\sum_i \frac{\hbar^2}{2m_e} \nabla_i^2 - \sum_{i,I} \frac{Z_I e^2}{|\mathbf{r}_i - \mathbf{R}_I|} + \sum_{i \neq j} \frac{e^2}{2|\mathbf{r}_i - \mathbf{r}_j|} \quad (3.3)$$

The equation 3.3 is solvable for the simple system such as He or H<sub>2</sub> but for the more than two nuclei and two electrons is almost impossible to solve analytically. Thus for many body system, n-electron system, the approximation is absolutely needed [45].

## 3.2 The electron density

This section will be focused on the reformulation of the equation 3.3 in which electron density plays the central role. The formulation was firstly reported in two seminal papers [46] and [47]. The main idea is to replace the complicated many-body interaction with the electron density as shown in the Fig. 3.2.

The Kohn-Sham formula in Hartree atomic unit ( $m = \hbar = 4\pi/\epsilon_0 = 1$ ) of the equation 3.3 for the one-electron orbital is written as

$$\left( -\frac{1}{2} \nabla^2 + V_{ext}(\mathbf{r}) + \int \frac{\rho(\mathbf{r}')}{|\mathbf{r} - \mathbf{r}'|} d\mathbf{r}'^3 + V_{xc}(\mathbf{r}) \right) \psi_i = \epsilon_i \psi_i, \quad (3.4)$$

Where the  $V_{ext}$  is the external potential including nuclei potential, the third term is known as Hartree potential,

$$V_H = \int \frac{\rho(\mathbf{r}')}{|\mathbf{r} - \mathbf{r}'|} d\mathbf{r}'^3 \quad (3.5)$$

$V_{xc}$  arise from the exchange-correlation among electrons, and  $\rho(\mathbf{r})$  is the electron density. The electron density is obtained from the one electron orbital :

$$\rho(\mathbf{r}) = \sum_i^N |\psi_i(\mathbf{r})|^2 \quad (3.6)$$

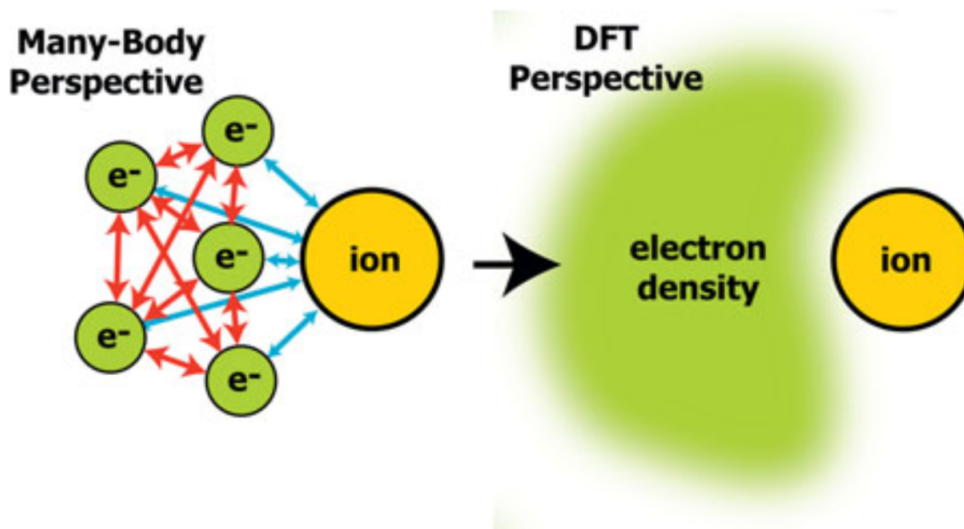


Figure 3.2: The DFT perspective. The complicated interaction of the ion with electron inside the system is replaced by interaction of one ion with electron density. Adapted from [48].

The exchange-correlation interaction as functional of the density is expressed as,

$$V_{xc}(\mathbf{r}) = \frac{\delta E_{xc}[\rho(\mathbf{r})]}{\delta \rho(\mathbf{r})} \quad (3.7)$$

The  $E_{xc}$  is very complicated and prevent us to get straightforward solution of this equation. Thus we need approximation of exchange-correlation approximation. Nowadays, many kinds of the exchange-correlation functions are available. The self-consistently solution of the equation 3.4 will yield the ground state energy of the system,

$$E_0 = \sum_i \epsilon_i + E_{xc}[\rho_0(\mathbf{r})] - \int V_{xc}\rho_0(\mathbf{r})d^3\mathbf{r} - \frac{1}{2} \int \frac{\rho_0(\mathbf{r})\rho_0(\mathbf{r}')}{|\mathbf{r} - \mathbf{r}'|} \quad (3.8)$$

### 3.3 The exchange-correlation function

In this section, I will briefly describe the most common of exchange-correlation function. One of them, the generalized gradient approximation (GGA), is used in this thesis.

#### 3.3.1 The local density approximation (LDA)

The local density approximation (LDA) is the simplest exchange-correlation function. The main idea of this approximation is that the exchange-correlation energy at a point  $\mathbf{r}$  is



determined by exchange-correlation energy of homogeneous electron gas at the point  $\mathbf{r}$  [49] and can be written as

$$E_{xc}^{LDA}[\rho(\mathbf{r})] = \int \rho(\mathbf{r})\epsilon_{xc}^{hom}[\rho(\mathbf{r})]d\mathbf{r} \quad (3.9)$$

The parameterization of the  $\epsilon_{xc}^{hom}[\rho(\mathbf{r})]$  by using stochastic method of the homogeneous electron gases at various densities [50] was given by Perdew and Zunger [51] which is later interpolated by Vosko, Wilk and Nusair [52].

The extension of LDA to the spin-polarized system is so called local spin density approximation (LSDA) which employ two spin densities,  $n^\uparrow$  and  $n^\downarrow$ , and can be write down as

$$E_{xc}^{LSDA}[\rho^\uparrow(\mathbf{r}), \rho^\downarrow(\mathbf{r})] = \int \rho(\mathbf{r})\epsilon_{xc}^{hom}[\rho^\uparrow(\mathbf{r}), \rho^\downarrow(\mathbf{r})]d\mathbf{r} \quad (3.10)$$

The LSDA is very good for the isotropic and homogenous system such as metal but sometimes give wrong description for the binding energy especially in molecules, underestimates lattice parameters, phase stability incorrect order, and energetics of magnetic materials in error.

### 3.3.2 The generalized gradient approximation (GGA)

The homogenous electron-gas (LDA) is not appropriate model for the system at which electron density can vary over small region. The generalized gradient approximation (GGA) is the improvement version of LDA which its functional depend on both the density and the gradient of the density. The espression of the GGA can be written as

$$E_{xc}^{GGA}[\rho(\mathbf{r})] = \int \rho(\mathbf{r})\epsilon_{xc}^{hom}[\rho(\mathbf{r})]F_{xc}[\rho(\mathbf{r}), \nabla\rho(\mathbf{r})]d\mathbf{r} \quad (3.11)$$

Where  $F_{xc}[\rho(\mathbf{r}), \nabla\rho(\mathbf{r})]$  is known as the enhancement factor. The GGA greatly reduce the bond dissociation energy error, and generally improve transition-state barriers. But, unlike LDA, many possible variations are possible, each corresponding to a different enhancement factor. The familiar GGA functionals are given as follows:

- Perdew Wang 91 (PW91) [53]  
PW91 is obtained from full *ab-initio* which is applicable for wide range materials.
- Perdew, Burke and Ernzerhof (PBE) [54]  
PBE is contain minor change of the PW91 by simplify its derivation
- Revised PBE (RPBE) [55]  
RPBE is improvement of the atomisation energies of small molecules and chemisorption energies of atoms and molecules on transition metal surfaces of the PBE by semi-empirical change of the PBE.

## 3.4 Pseudopotential

In order to simplify the calculation, it is very efficient to divide the electron in two categories, core/inner and valence electron, and replace the full potential from nuclei and core electron by pseudopotentials (PPs). In other words, pseudopotential is effective potential that the valence electron feel. The pseudo wavefunctions and pseudopotential are identical to the all electron wavefunction and potential outside a radius cut-off  $r_c$  as illustrated in the Fig 3.3.

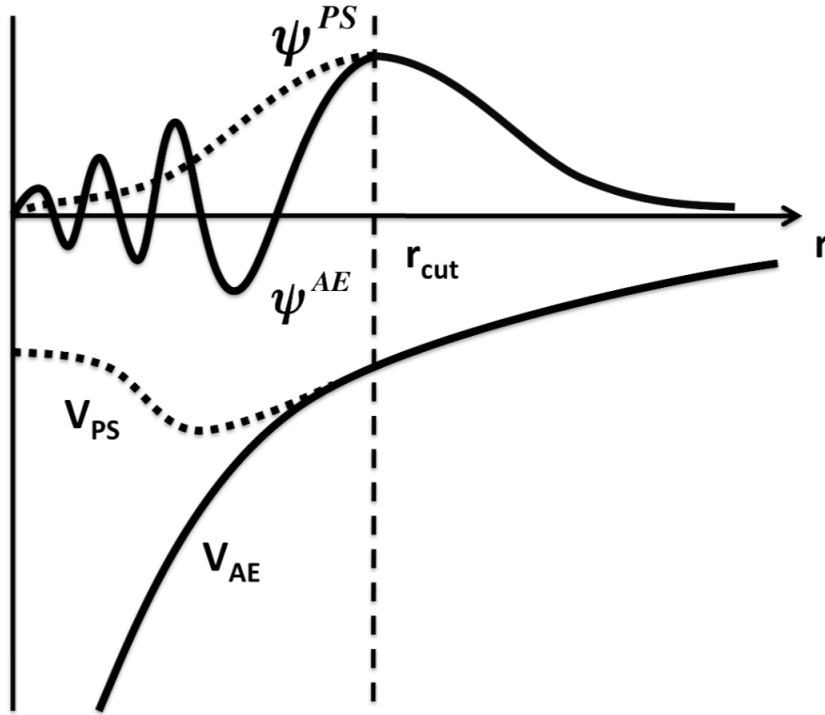


Figure 3.3: The illustration of the pseudopotentials which the effective potential for nucleus and core electrons. The solid (dashed) line is the all electron wavefunction and potential (pseudo wavefunction and pseudopotentials).

There various PPs are available which are given as follows:

### 1. Norm-conserving PPs [56].

The first type of the norm-conserving PPs is so-called in which the charge densities of the core is equal to the all electron (AE) charge densities within cutoff radius  $r_c$ . The generation of the PPs is given as follows :

$$\int_0^{r_c} |\Psi_{PPs}(\mathbf{r})|^2 = \int_0^{r_c} |\Psi_{AE}(\mathbf{r})|^2 \quad (3.12)$$

Where  $\Psi_{PPs}$  is the pseudo wavefunction and  $\Psi_{AE}$  is all electrons potentials.

## 2. Ultrasoft PPs [57].

The ultrasoft PPs is generated in a much smaller planewave cutoff. The electronic density is augmented. The charge which has been removed has to be put back to compute the density functional augmentation charges and the wavefunctions are smoother. The electron density is

$$\rho(\mathbf{r}) = \sum_n \left[ |\phi_n(\mathbf{r})|^2 + \sum_{ij} \langle \phi_i | \beta_n \rangle \langle \beta_i | \phi_n \rangle \right] \quad (3.13)$$

where  $\beta_i$  are projector functions and the augmentation function  $Q_{ij}(\mathbf{r})$  is given by

$$Q_{ij}(\mathbf{r}) = \psi_i^*(\mathbf{r})\psi_j(\mathbf{r}) - \phi_i^*(\mathbf{r})\phi_j(\mathbf{r}), \quad (3.14)$$

$\psi_i(\mathbf{r})$  are the all-electron wavefunctions, and  $\phi_i(\mathbf{r})$  are ultrasoft wavefunctions.

## 3. Projector-augmented Wave (PAW) PPs .

The PAW is introduced by Blöchl [58] and then adopted by Kresse and Joubert [59]. In this scheme, the wave function of all electron is given by

$$|\psi_n\rangle = |\tilde{\psi}_n\rangle + \sum_i (|\phi_i\rangle - |\tilde{\phi}_i\rangle) \langle \tilde{p}_i | \tilde{\psi}_n \rangle \quad (3.15)$$

where  $|\tilde{\psi}_n\rangle$  is the pseudo orbitas and  $|\phi_i\rangle$ ,  $|\tilde{\phi}_i\rangle$  and  $\langle \tilde{p}_i | \tilde{\psi}_n \rangle$  are atom-centered localized functions. The second term in the equation 3.14 is pseudo onsite wavefunction and the last term is exact onsite wavefunction. The illustration of those parameter are given in the Fig. 3.4.

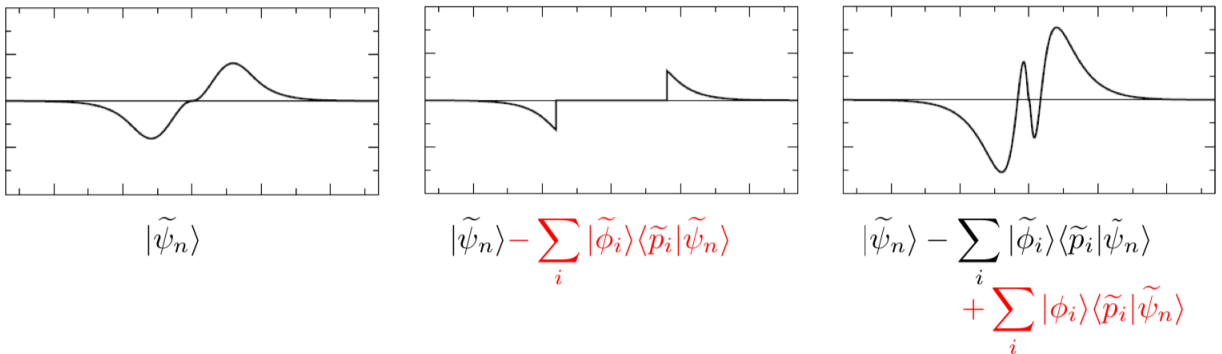


Figure 3.4: The illustration of the parameter in the PAW.

## 3.5 Plane wave basis set

In crystalline solid, the potential that electron feels is periodic and invariant under translation vector  $\mathbf{R}$ ,

$$V(\mathbf{r}) = V(\mathbf{r} + \mathbf{R}) \quad (3.16)$$

Where  $\vec{R}$  is the any translational vector which is defined by,

$$\mathbf{R} = n_1 \mathbf{a}_1 + n_2 \mathbf{a}_2 + n_3 \mathbf{a}_3 \quad (3.17)$$

Based on the **Bloch's** theorem, an electron in a periodic potential has the wavefunctions,

$$\Psi_{n,\mathbf{k}}(\mathbf{r}) = u_j(\mathbf{r})e^{i\mathbf{k}\mathbf{r}} \quad (3.18)$$

The  $\mathbf{k}$  is quantum number which correspond to the vector in the Brillouin zone.  $u_{\mathbf{k}}$  is also periodic in the crystal and it can be expanded in a Fourier series,

$$u_j(\mathbf{r}) = \frac{1}{\sqrt{\Omega}} \sum_{\mathbf{G}} c_{j,\mathbf{G}} e^{i\mathbf{G}\cdot\mathbf{r}} \quad (3.19)$$

where  $\mathbf{G}$  is reciprocal lattice vector,  $\mathbf{G} \cdot \mathbf{R} = 2\pi m$  and  $m$  is an integer,  $c_{j,\mathbf{G}}$  is the plane-wave coefficient. The expansion of the electron's wavefunction can be written as linear combination of the plane waves,

$$\psi_{j,\mathbf{k}}(\mathbf{r}) = \frac{1}{\sqrt{\Omega}} \sum_{\mathbf{G}} c_{j,\mathbf{k}+\mathbf{G}} e^{i(\mathbf{k}+\mathbf{G})\cdot\mathbf{r}} \quad (3.20)$$

The charge density is calculated by integrating the equation 3.19 over the first Brillouin zone,

$$\rho(\mathbf{r}) = \frac{1}{\Omega_{BZ}} \sum_n \int_{BZ} f_{n\mathbf{k}} |\psi_{j,\mathbf{k}}(\mathbf{r})|^2 d\mathbf{k} \quad (3.21)$$

and various contribution to the potential in the Kohn-Sham equation can be written as,

$$V(\mathbf{r}) = \sum_{\mathbf{G}} \bar{v}(\mathbf{G}) e^{i\mathbf{G}\cdot\mathbf{r}} \quad (3.22)$$

where  $\bar{v}(\mathbf{G})$  represents the Fourier transform of the corresponding real-space quantity. Thus the Kohn-Sham equation can rewrite in the reciprocal space representation,

$$\sum_{\mathbf{G}'} \left[ -\frac{1}{2} |\mathbf{k} + \mathbf{G}'|^2 \delta_{\mathbf{G},\mathbf{G}'} + \bar{v}_{\text{ext}}(\mathbf{G} - \mathbf{G}') + \bar{v}_{\text{H}}(\mathbf{G} - \mathbf{G}') \right] \psi_j(\mathbf{k} + \mathbf{G}') = \epsilon_j \psi_j(\mathbf{k} + \mathbf{G}') \quad (3.23)$$

The expansion of the plane-wave basis set should be infinite in the exact calculation. In practical, kinetic energy cut-off  $E_{cut}$  in order to achieve a finite basis set. The kinetic energy cut-off is defined as

$$\frac{1}{2}|\mathbf{k} + \mathbf{G}|^2 \leq E_{cut} \quad (3.24)$$

The plane wave that included in the basis set has the kinetic energy smaller than  $E_{cut}$ . There are several advantages to use the plane wave basis set as follows :

- It is independent of atom position and species.
- The forces acting on atoms are equal to Hellmann-Feynman forces, no basis-set corrections to the forces (no Pulay forces).
- The efficient calculation of convolutions, use FFT to switch between real space mesh and reciprocal space.
- The basis-set convergence can be easily control by cut-off energy.

### 3.6 Solve the Kohn-Sham self consistently

We can write the equation 3.4 by,

$$\hat{\mathbf{H}}_{KS}\psi_i(\mathbf{r}) = \epsilon_i\psi_i(\mathbf{r}) \quad (3.25)$$

with  $\hat{\mathbf{H}}_{KS}$  is the effective Hamiltonian,

$$\hat{\mathbf{H}}_{KS} = -\frac{1}{2}\nabla^2 + V_{KS}(\rho(\mathbf{r})) \quad (3.26)$$

where the  $V_{KS}$  is the effective Kohn-Sham potential,

$$V_{KS}(\rho(\mathbf{r})) = V_{ext}(\rho(\mathbf{r})) + V_H(\rho(\mathbf{r})) + V_{xc}(\rho(\mathbf{r})) \quad (3.27)$$

Once the PPs, exchange-correlation function, and energy cut are decided, the Kohn-Sham equation can be solved by self-consistent procedure as shown in the Fig. 3.5.

### 3.7 The DFT+U

In a system that the highest energy orbital half filling/empty, the band theory predicts that it will show conductor state. If the on-site coulomb repulsive interaction between electron is strong enough to block the electron conduction, the system become insulator. This kind of system is known as Mott insulator [32, 60]. The typical strong on-site coulomb interaction is observed in localized  $d$  and  $f$  electrons.

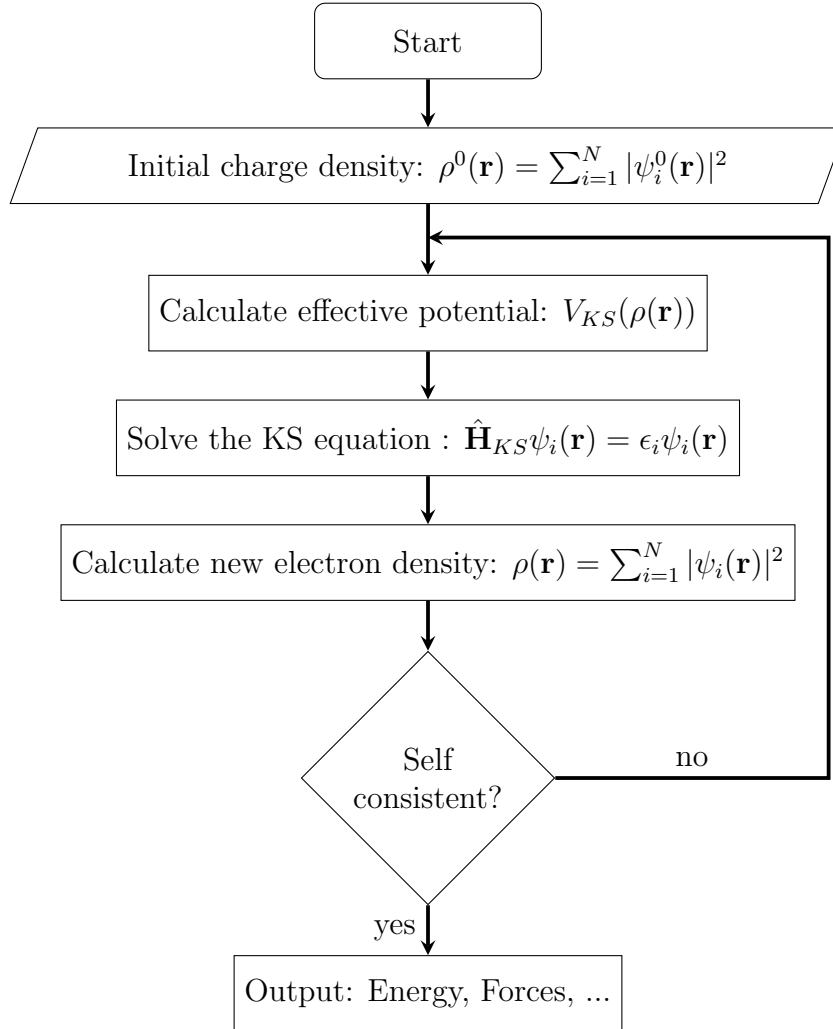


Figure 3.5: The folow chart of the self consistent procedure.

The LDA/GGA functional gives the poor description of a Mott insulator. The GGA/LDA need an additional on-site coulumb interaction parameter,  $U$ , in the Hamiltonian in order to open the gap around the fermi surface as shown in the Fig. 3.6.

The on-site interactions can be expressed in two parameters, on-site coulumb interaction  $U$  and on-site exchange interaction/Hund coupling  $J$ . The on-site interaction can be introduced in to the DFT calculation in two different ways,

- The rotationally invariant LSDA+U [61]. In this scheme, the  $U$  and  $J$  are introduced independently. The total energy is given by,

$$E_{tot}(n, \hat{n}) = E_{DFT}(n) + E_{HF}(\hat{n}) - E_{dc}(\hat{n}) \quad (3.28)$$

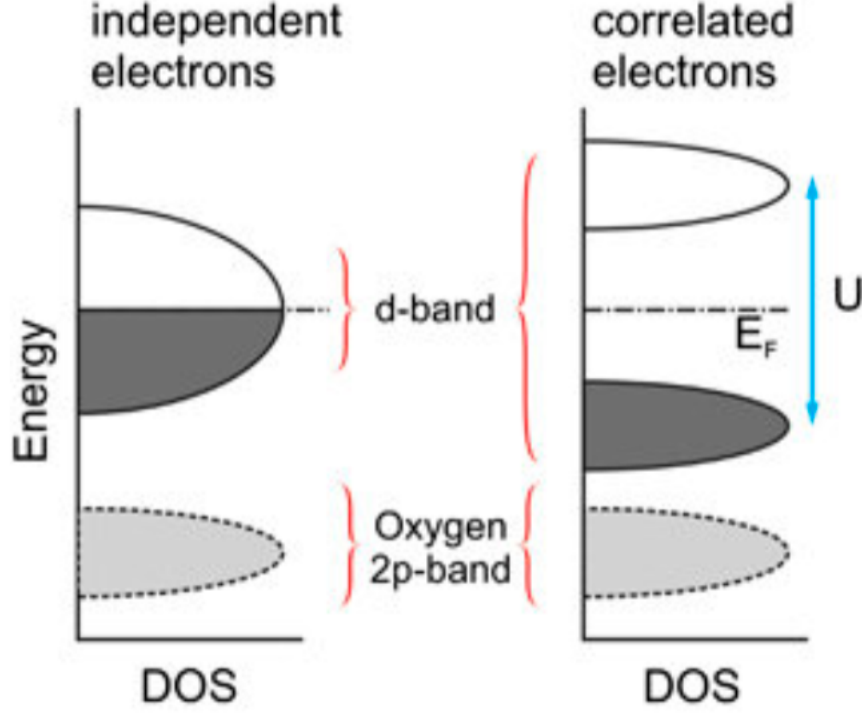


Figure 3.6: The schematic energy-band diagrams of a Mott–Hubbard insulator. The  $d$ -band are separated in to lower and upper Hubbard band by on-site coulumb interaction.

where the  $E_{HF}(\hat{n})$  is Hartree-Fock like interaction and given by,

$$E_{HF} = \frac{1}{2} \sum_{\{\gamma\}} (U_{\gamma_1\gamma_3\gamma_2\gamma_4} - U_{\gamma_1\gamma_3\gamma_4\gamma_2}) \hat{n}_{\gamma_1\gamma_2} \hat{n}_{\gamma_3\gamma_4} \quad (3.29)$$

where  $U_{\gamma_1\gamma_3\gamma_2\gamma_4}$  is the unscreened electron-electron interaction. The  $E_{dc}$  is double counting energy correction,

$$E_{dc}(\hat{n}) = \frac{U}{2} \hat{n}_{tot}(\hat{n}_{tot} - 1) - \frac{J}{2} \sum_{\sigma} \hat{n}_{tot}(\hat{n}_{tot} - 1) \quad (3.30)$$

- The simplified (rotationally invariant) approach to the LSDA+U [62]. In this scheme the  $U$  and  $J$  are introduced simultaneously as  $U_{eff} = U - J$ .

$$E_{LSDA+U} = E_{LSDA} + \frac{(U_{eff})}{2} \sum_{\sigma} (n_{m,\sigma} - n_{m,\sigma}^2), \quad (3.31)$$

The total number of the electron is given by  $N_{\sigma} = \sum_m n_{n,\sigma}$ . This approach is used in this thesis.

## 3.8 The muon site calculation

The muon-site calculation procedure in this thesis was done with the following steps:

1. Choose the pseudopotential and exchange-correlation function.
2. Get the optimum parameter in the DFT+U calculation which can explain the Antiferromagnetic Mott insulator behaviour of the YBCO<sub>6</sub>.
3. Calculate the potential in the unit cell of the YBCO<sub>6</sub>, without muon/unperturbed, and find the local minimum potential which can be regarded as initial muon position.
4. Introduce muon in to the system by placing muon which is modelled as hydrogen pseudopotential in the local minimum potentials.
5. The structural relaxation in which all ion and atom are allow to relax until the force convergence achieved was done in the large supercell to compensate muon as ultradilute impurity.
6. The final ion and muon position are extracted for next postprocessing calculation. The magnetization density from the DFT+U calculation was also extracted for the internal fields calculation at each muon sites.

The DFT calculation is done by *Vienna Ab initio Simulation Package* (VASP) [63, 64]. The implementation of parallel computing algorithm MPI (Message Passing Interface) on VASP allows us to perform a fast and efficient calculation in a supercomputer. In this thesis, the DFT calculation was done in HOKUSAI supercomputer [65].





# Chapter 4

## Results and discussion

### 4.1 The $\mu$ SR experiment

The zero-field  $\mu$ SR measurement of the high-quality single crystal of  $\text{YBa}_2\text{Cu}_3\text{O}_6$  as shown in the Fig. 4.1(a) was performed at Paul Scherrer Institute (PSI) by using DOLLY spectrometer. The DOLLY spectrometer has four positron detectors, forward (F), backward (B), left (L) and right (R), and two veto detectors that are placed in the forward and backward directions along the muon beam. The backward veto detector collimates the muon beam and rejects muons missing the aperture, while the forward veto detector reject muons missed to hit the sample. This spectrometer is equipped by Oxford Variox cryostat. The mercury temperature controller was used to control the sample's temperature. In order to reach a temperature below 2 K, the carefully control the exchange  $^4\text{He}$  was done. To reach temperature lower than 2 K, the Heliox-VT system was used to insert  $^3\text{He}$  which has lighter mass than  $^4\text{He}$  and liquefies at 3 K. The lowest temperature that can be achieved is 0.3 K by pumped under its own vapour pressure. The continuous muon beam was directed perpendicular to a-b plane of the single crystal as shown in the Fig. 4.1(b). The orange sphere is muon, the black arrow indicates the muon's spin and the red broken line indicates the direction of implanted muon. The high-statistics data, 629 million events, were collected at temperature 1.5 K. The time spectra of the  $\mu$ SR and its fourier transform are shown in the Fig. 4.2.

The clear muon spin precession is clearly observed in this sample which indicate a static long-range magnetic ordering. The fourier transform was fitted by three distinct gaussian functions which indicate three distincts muon spin precession which correspond to the three different muon site in this system. The average internal fields at each muon site are 118.8 G, 214.7 G and 293.6 G. The Fourier power has highest intensity at muon-site with internal fields 293.6 G that reveal that after implantation process the dominant muon stop in this site. The internal fields around 300 G is typical value for the  $\text{YBa}_2\text{Cu}_3\text{O}_6$  [11, 66]. A broad peak around 1 ~ 2 MHz was also pointed out by Nishida, et.al [21]. The high-quality single crystal and the collected high-statistic data allow us to observed more detail the muon-spin precession. The additional muon site owning internal fields 214.7 G has never

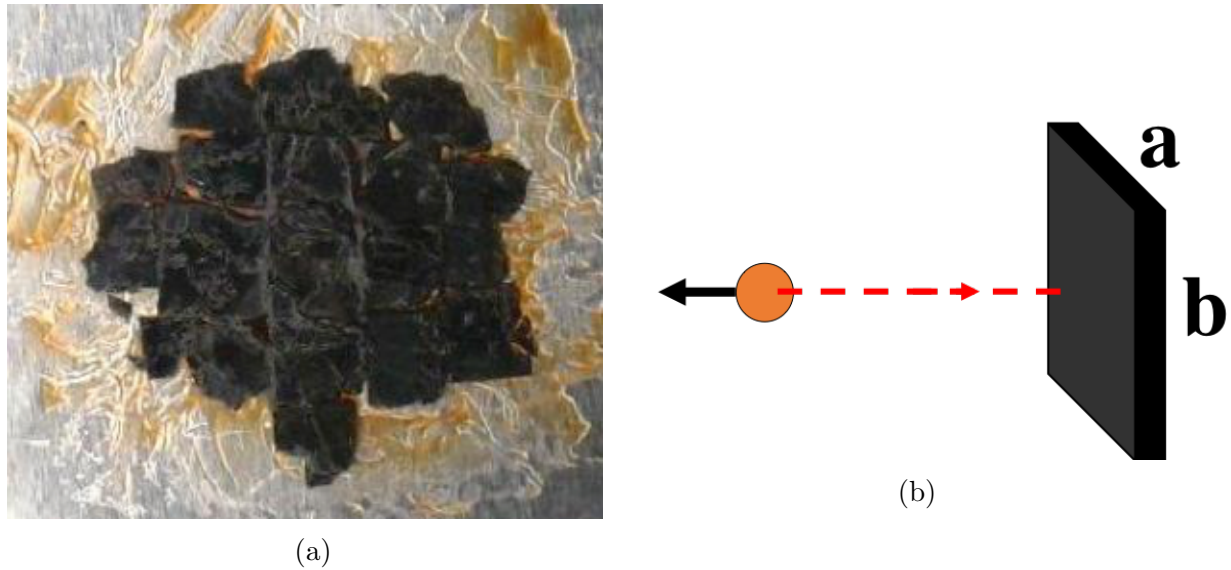


Figure 4.1: (a) The single crystal of  $\text{YBa}_2\text{Cu}_3\text{O}_6$  for the  $\mu\text{SR}$  experiment and (b) The experimental set up. the muon beam is directed perpendicular to the a-b plane of the single crystal.

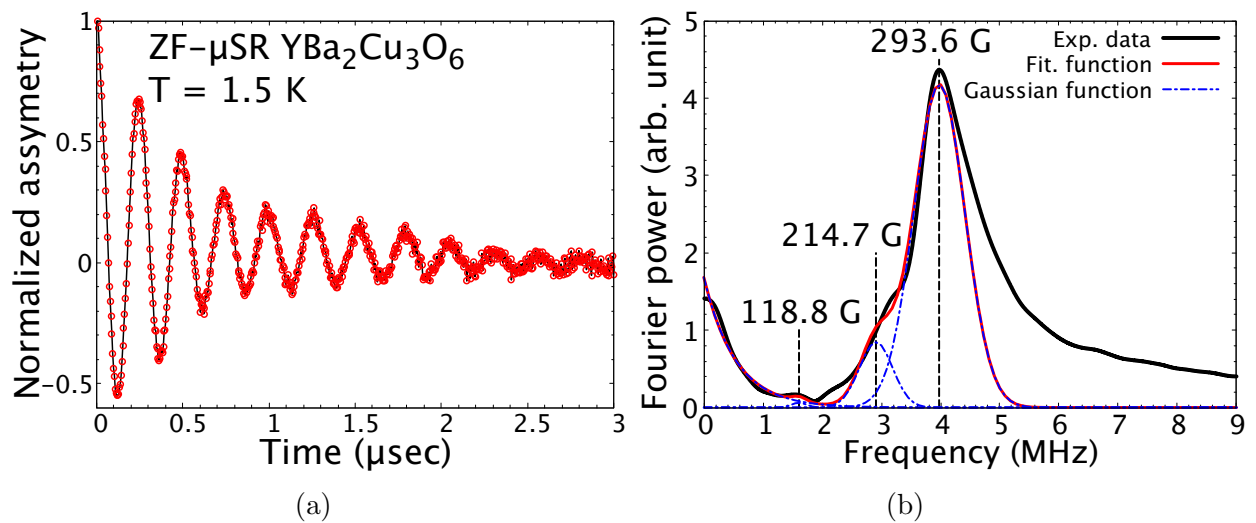


Figure 4.2: (a) The  $\mu\text{SR}$  time spectra of the  $\text{YBa}_2\text{Cu}_3\text{O}_6$  at  $T = 1.5$  K which measured by continuous beam in PSI and (b) its Fourier transform which fitted by three distinct Gaussian components.

been reported before. The further understanding of this results require the knowing the muon-site and the complete description of the muon inside the sample.

## 4.2 The muon-site calculation

### 4.2.1 The band-structure calculations

The density functional theory (DFT) needs additional on-site coulomb interaction parameter,  $U$ , in order to give realistic description electronic and magnetic properties of the  $\text{YBa}_2\text{Cu}_3\text{O}_6$  as a Mott insulator in which the energy gap around Fermi level in band structure and density of states (DOS) must be exist. The band structure DOS calculation were done by using supercell which contains  $2 \times 2 \times 1$  (=4) unit cells. This supercells is required to accomodate the magnetic unit cell of the  $\text{YBa}_2\text{Cu}_3\text{O}_6$ .

The calculation was performed by using exchange corelation function generalized gradient approximation (GGA) in the Perdew Wang 91 formulation [53]. The on-site coulomb electron repulsive,  $U$ , was introduced by Duradev approach [62]. In order simplify the calculation, the projected augmented wave (PAW) pseudopotential is used to separate the core and valence electrons [58, 59]. The DFT calculation was performed by plane-wave method as implemeted in the *Vienna ab-initio software package* (VASP) [64, 63]. The crystal structure of  $\text{YBa}_2\text{Cu}_3\text{O}_6$  was set to be tetragonal with the space group  $P4/mmm$ . The lattice parameters of the unit cell were  $a=b=3.865(1) \text{ \AA}$  and  $c=11.854 \text{ \AA}$  [67].

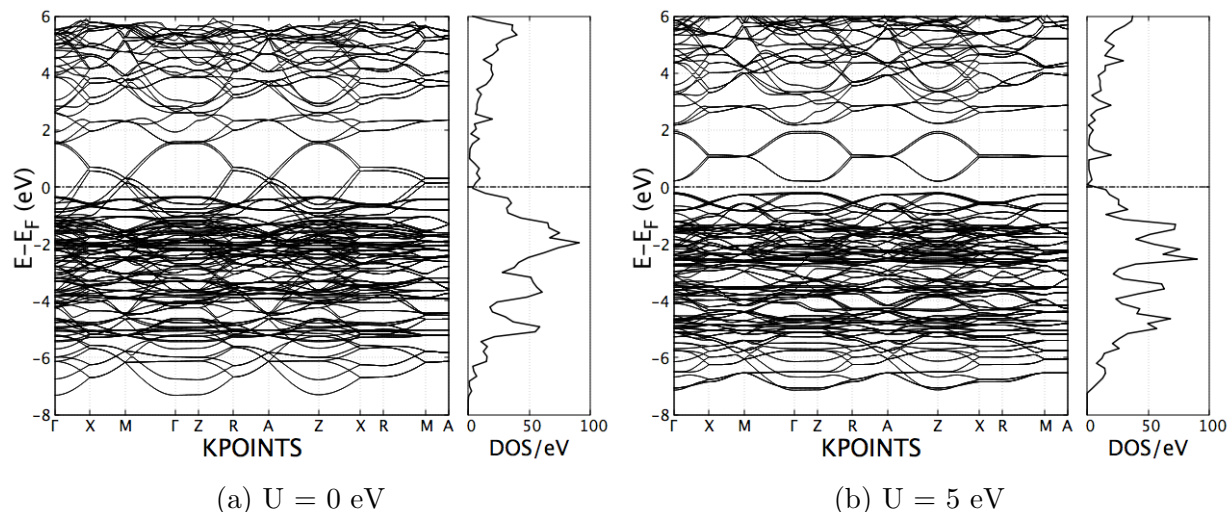


Figure 4.3: The band structure and DOS of  $\text{YBa}_2\text{Cu}_3\text{O}_6$  for (a)  $U = 0 \text{ eV}$  which no energy gap around Fermi level and (b)  $5 \text{ eV}$  which energy gap exists around Fermi level.

The typical band structure and DOS for the  $U$  value  $0 \text{ eV}$  and  $5 \text{ eV}$  are shown in the Fig 4.3 (a) and (b), respectively. The DFT without Hubbard correction ( $U=0$ ) showed the metal behaviour as band theory prediction. In the Fig 4.3 (b), the clear gap is observed

around the Fermi level. It is clearly shown that the Hubbard  $U$  is mandatory to give realistic electronic structure of the  $\text{YBa}_2\text{Cu}_3\text{O}_6$ .

The energy gap dependence on the  $U$  value is shown in the Fig 4.4. The energy gap is start to open at  $U = 4$  eV and increase monotonically as the  $U$  value increase. From this results, the  $U$  value for  $\text{YBa}_2\text{Cu}_3\text{O}_6$  must be greater than 3 eV.

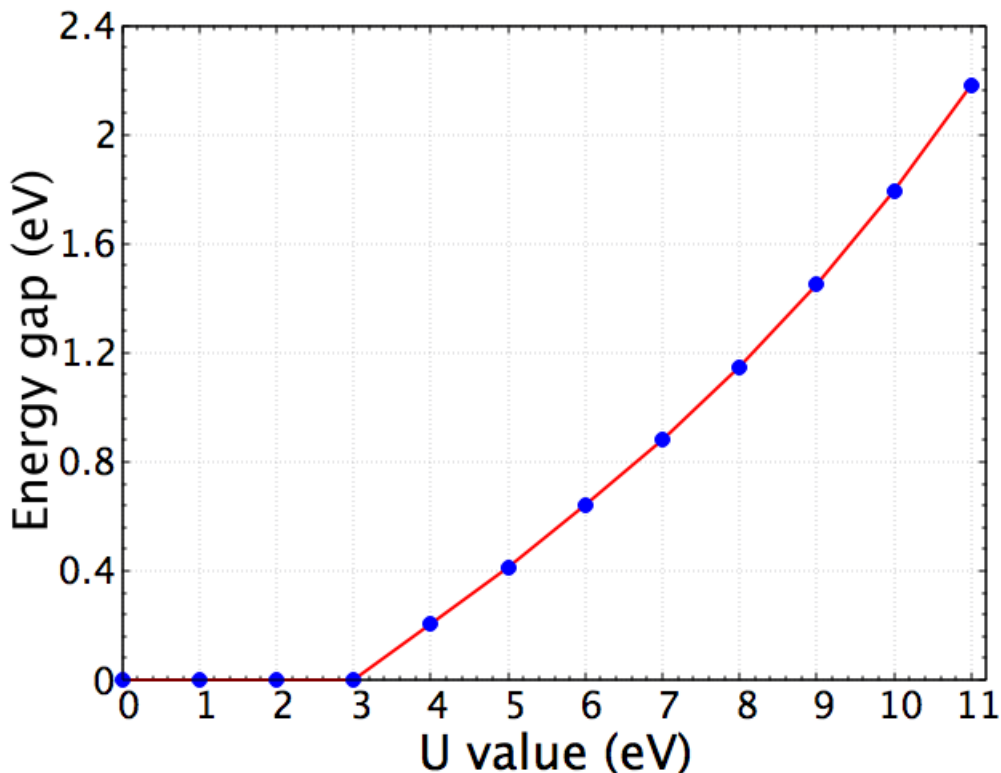


Figure 4.4: [The band gap dependence on the on-site coulomb interaction parameter,  $U$ . The size of the gap is proportional with the  $U$  value.

### 4.2.2 Initial muon site

Since the muon has a positive charge, the implanted muon will stop at local minimum potential. Based on the DFT+ $U$  calculation with same condition in the band structure and DOS calculation, three different local minimum potential side which can be regarded as initial muon site are identified in the unit cell of  $\text{YBa}_2\text{Cu}_3\text{O}_6$ , marked as M1, M2 and M3, as shown in the of the Fig. 4.5 (a). The red area indicate the isosurface of the potential at the level 700 meV. The Fig. 4.5 (b) shows the detail of the potential map around the muon site. The M1 position has lowest potential energy and the potential barrier between M1 and M2 is 0.09 eV. The M2 and M3 is separated by potential barrier 0.54 eV. The initial muon position is not altered by changing the  $U$  value.

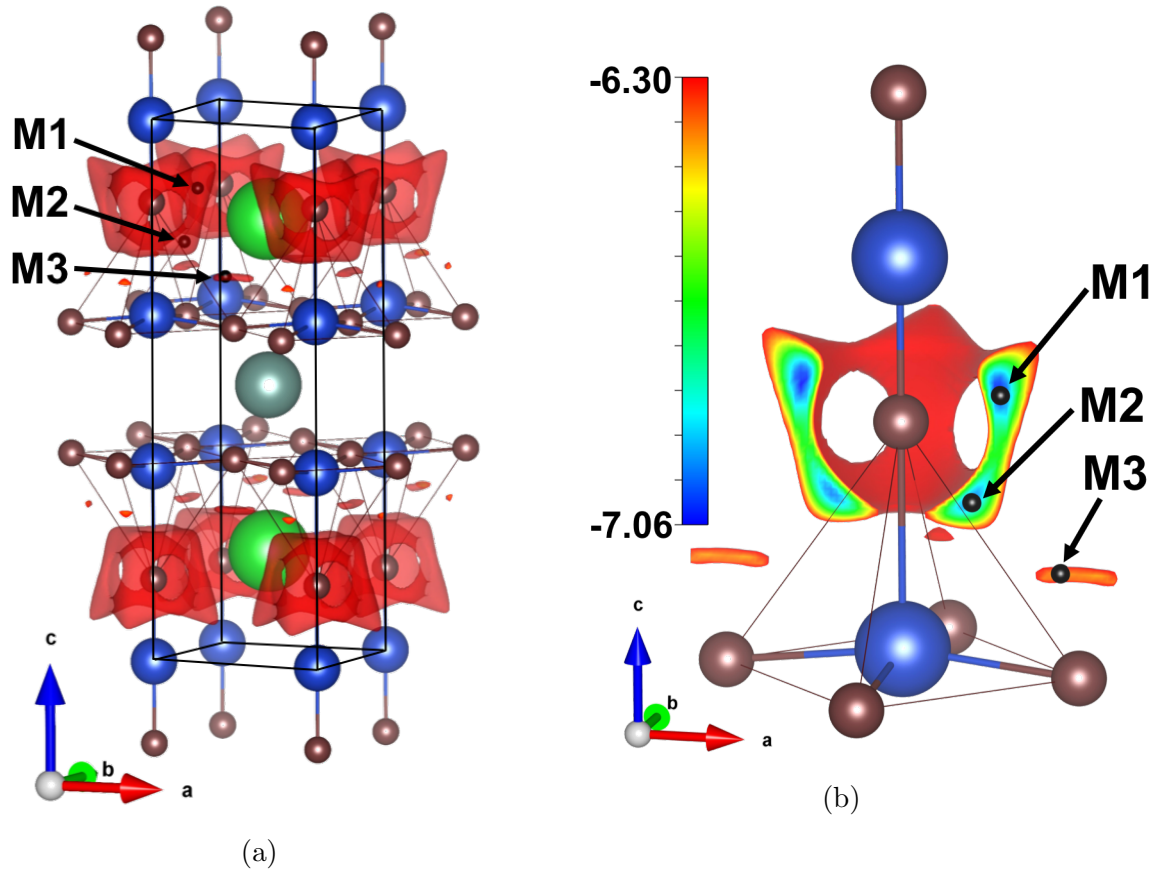


Figure 4.5: (a) The Initial muon site in YBa<sub>2</sub>Cu<sub>3</sub>O<sub>6</sub> and (b) the detail potential map in around muon side. The red area indicate the isosurface 700 meV.

### 4.2.3 The muon perturbation

In order to study the muon perturbation, the muon is introduced in to the YBa<sub>2</sub>Cu<sub>3</sub>O<sub>6</sub> as hydrogen ion. Because muon behave as ultradilute impuriy inside the system, the supercell is mandatory to simulate the realistic experimetal condition and the probabily of muons feels perturbation from other muon is effectively zero. The supercell size for this calculation is  $4 \times 4 \times 2$  ( $=32$ ) unit cell which contains 384 ion + 1 muon as shown in the Fig. 4.6. The charge of the supercell is set to be +1 due to the digmagnetic muon state in the insulator such as YBa<sub>2</sub>Cu<sub>3</sub>O<sub>6</sub>. Then, all ions including muon are allowed to relax until reach the force convegence threshold  $0.01 \text{ eV}/\text{\AA}$ . The effect of the muon at each muon sites are treated separately.

At the end of this calculation, the local crystal deformation and final muon site can be deduced at each muon site as shown in the Fig. 4.7. The muon perturbation is significant to the neighboring atoms. The local deformation that caused by muon are shown in the Fig. 4.7 (b), (c) and (d) with muon at M1, M2 and M3, respectively. The supercell size,  $4 \times 4 \times 2$  unit cells, is good enough to accomadate the periodic boundary conditions.

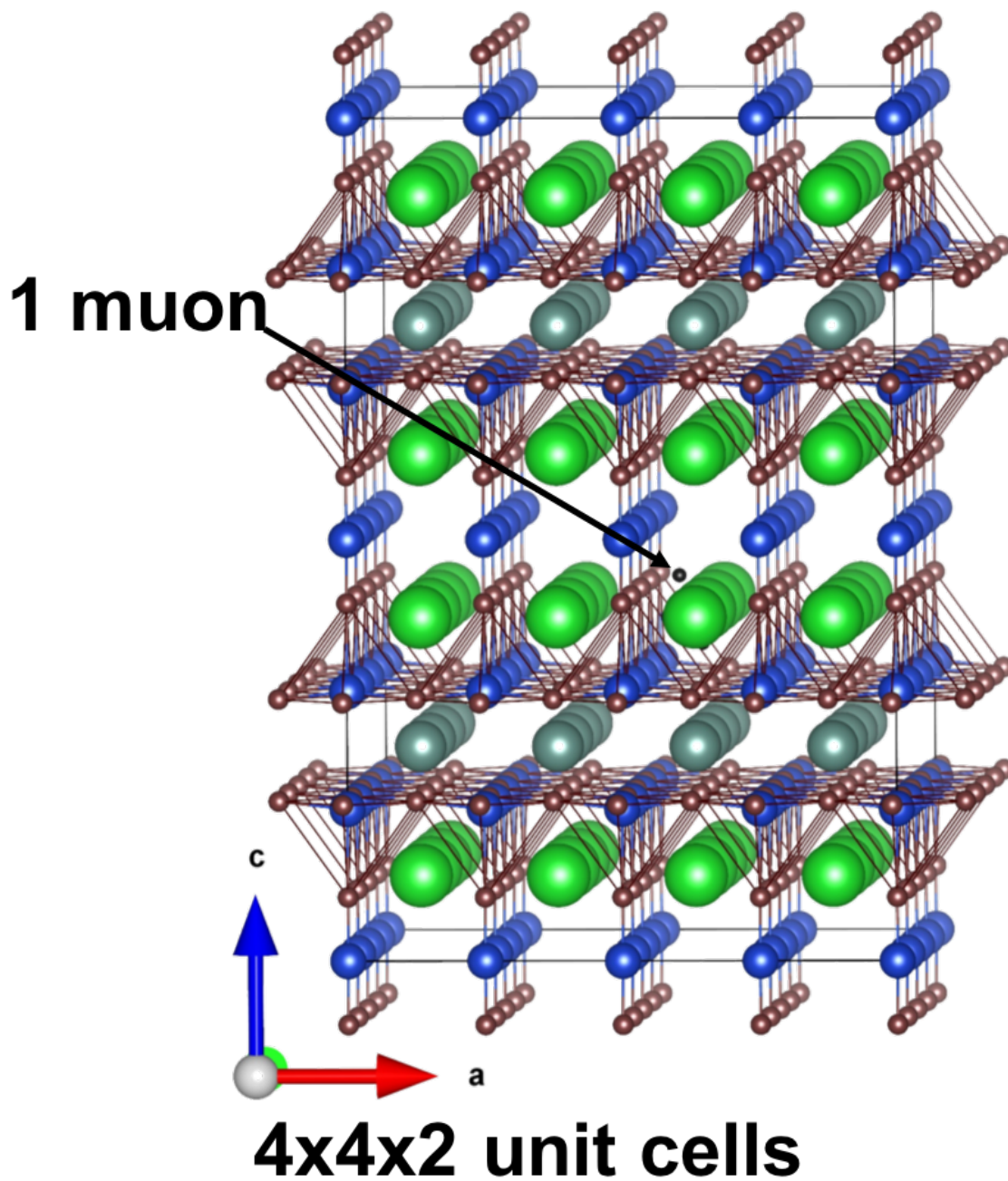


Figure 4.6: The supercell  $4 \times 4 \times 2$  unit cells which contains 384 atoms + 1 muon.

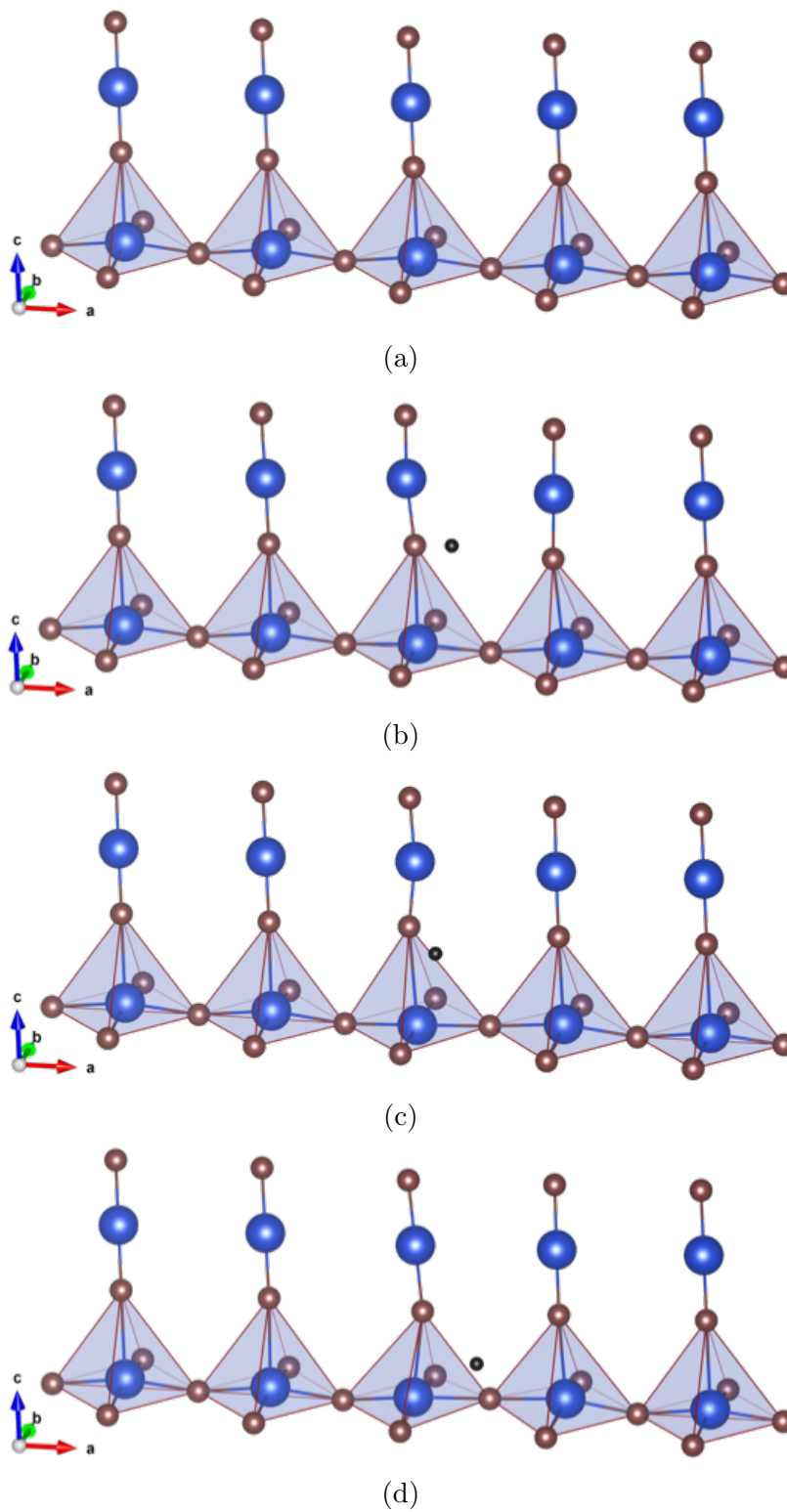


Figure 4.7: The crystal structure (a) unperturbed system, the muon perturbation with (b) muon at M1 (c) muon at M2 and muon at M3. The muon perturbation is significant to the neighboring ion and disappears in the supercell boundary.



#### 4.2.4 Internal fields simulation

As mention in the chapter 2, the main parameter that can be deduced from  $\mu$ SR time spectra is internal field at the muon sites. The main contribution to the internal fields is dipole-dipole interaction between localized magnetic moment with muon-spin. The calculation of internal fields was done by constucting spherical volume, Lorentz sphere, with the radius  $R_L$  as illustrated in the Fig. 4.8. The local moment outside the Lorentz sphere is discarded. The distorted crystal, perturbed supercell by muon, was placed in the center and surrounded by unperturbed supercell.

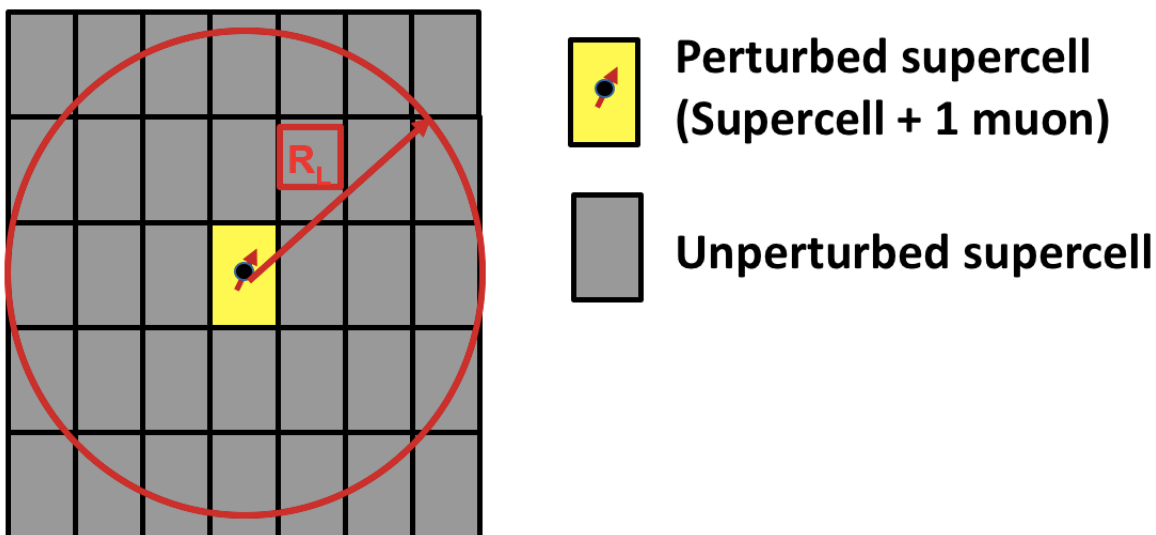


Figure 4.8: The illustrated of the Lorentz sphere with one perturbed supercell with one muon surrounded by unperturbed supercell.

The radius of the sphere,  $R_L$ , is needed to tune carefully in order to obtain accurate value of the internal fields. The trial calculation at various  $R_L$  value was performed until reach the convergence value. The convergence test is illustated in the Fig. 4.9. The internal value start to converge at around  $R_L = 40 \text{ \AA}$ . In order to guarantee the convergence and obtain the more accurate internal field value, in this thesis  $R_L$  is set to be  $100 \text{ \AA}$ .

The magnetic structure in this calculation was deduced from neutron diffraction experimental results at which spins are reside in the Cu ion [13]. Since  $\text{YBa}_2\text{Cu}_3\text{O}_6$  is a typical Mott insulator, the DFT+U calculation of the average magnetic moment size has strong dependence on the  $U$  value. Thus the carefully tune the  $U$  value is needed to get accurate value of the magnetic moment size and internal fields value. The magnetic moment size which is deduced from DFT+U calculation as a function of the  $U$  is shown in the Fig. 4.10. The dashed blue line indicates the magnetic moment,  $0.66 \mu_B$ , that is determined by neutron diffraction. The  $U$  value 9 eV is well reproduced this magnetic moment size.

The internal fields calculation results as function of the  $U$  value on the basis point dipole model, spin reside in the Cu, as suggested from neutron diffraction study are shown

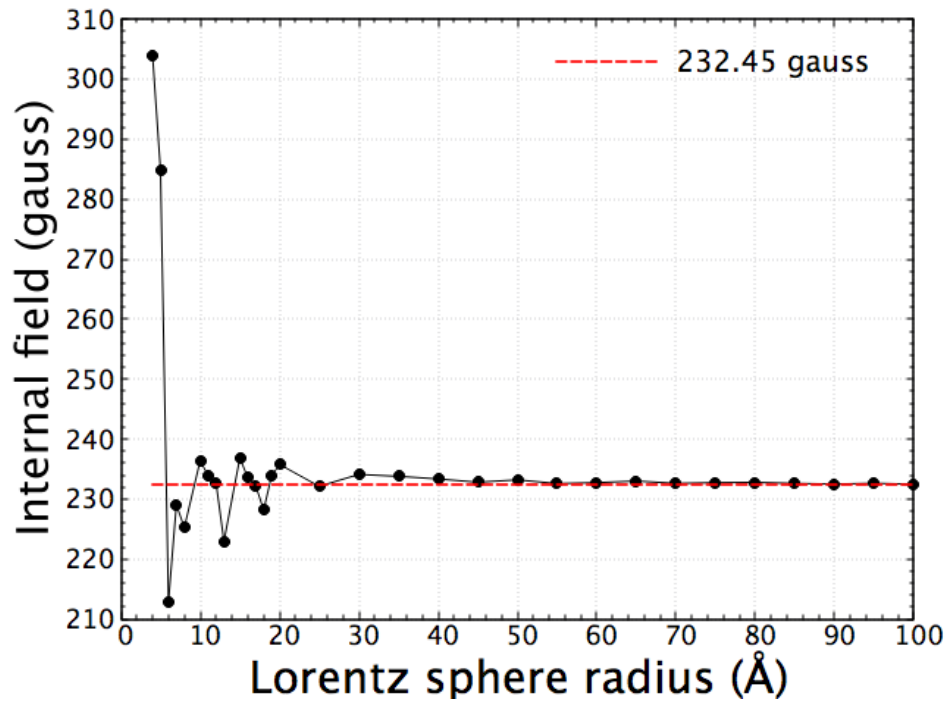


Figure 4.9: The convergence test of the internal fields. The value start to converge at  $R_L = 40 \text{ \AA}$ .

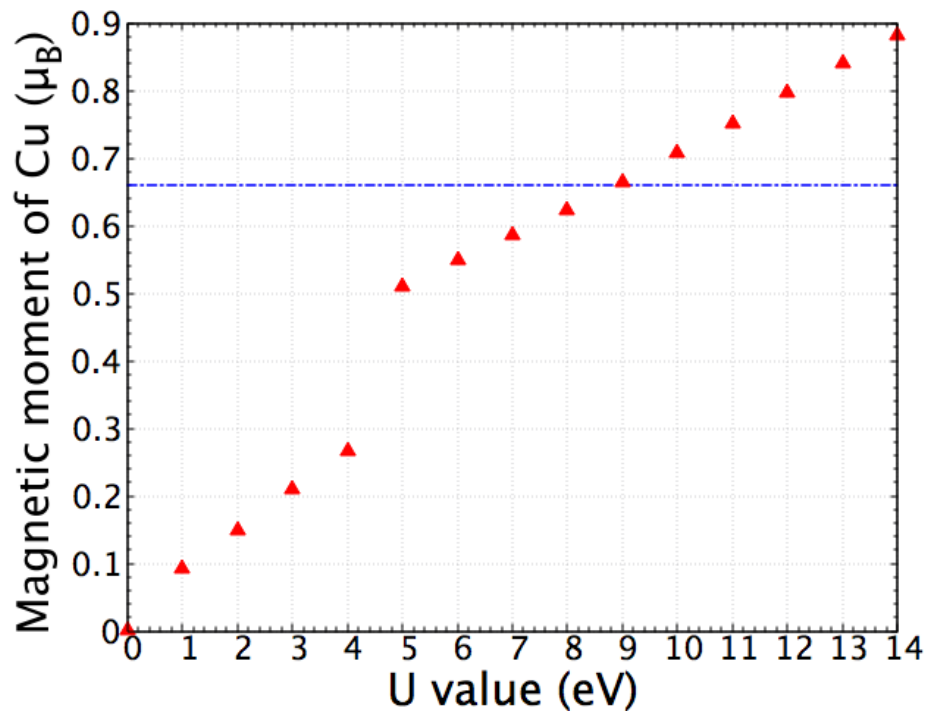


Figure 4.10: The magnetic moment size of Cu as function of the U. The dashed blue line indicates the magnetic moment size from neutron diffraction.

in the Fig. 4.11. The local crystal deformation is not considered in this results. The internal fields at M1, M2, and M3 positions monotonically increase with increasing  $U$ . Since there are three different muon spin precession component that are observed in our new high-statistics data with internal fields 118.8 G, 214.7 G and 293.6 G, the M2 position seems to be corresponded to the muon site owning internal fields 293,6 G at  $U$  value 4 eV. If we choose this  $U$  value for  $\text{YBa}_2\text{Cu}_3\text{O}_6$ , no estimated muon site is correspond to the internal field 214.7 G and this  $U$  value, 4 eV, is smaller to consider the strong on-site coulumb interaction.

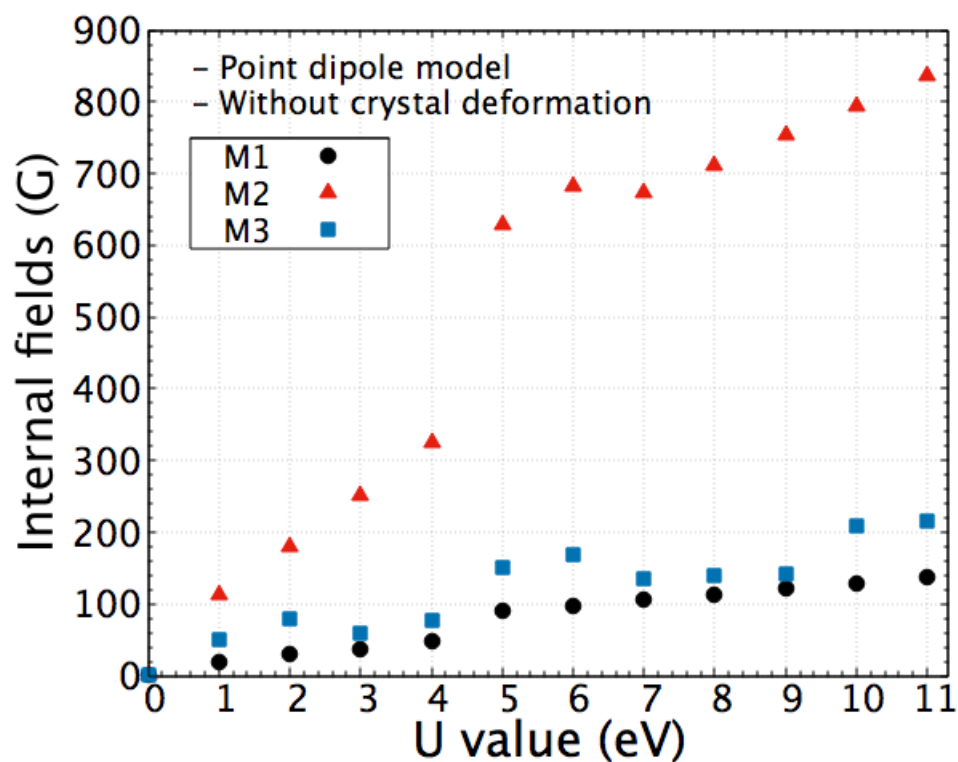


Figure 4.11: The calculated internal fields at muon site as function of the  $U$  based on point dipole model without any crystal deformation.

In the Fig. 4.12, the crystal deformation that induce by implanted muon is included in the calculations. If we set the M2 at  $U = 4$  or  $5$  eV related to the muon site owning internal fields 293.G, it is also no muon muon site correspond to the internal fields owning internal fields 214.7 G. Another possibility is to set M3 at the  $U = 6$  eV to be corresponding to the internal field 393.6 G. On the other hand, the M2 at  $U = 6$  eV is overestimated of any internal fields from the experimental. thus, we consider the quantum correction which is zero point energy vibration motion of muon as described in the next section.

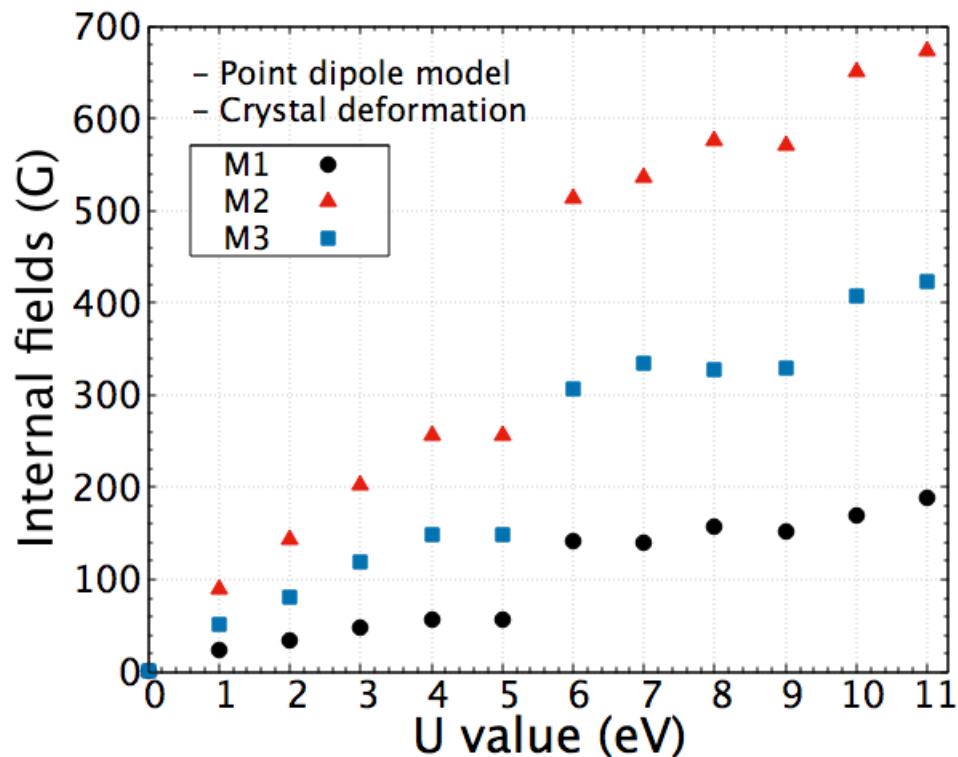


Figure 4.12: The calculated internal fields at muon site as function of the  $U$  based on point dipole model with crystal deformation.

### 4.3 Quantum correction

The quantum correction that concerned is zero point energy (ZPE) vibration motion of muon which is the energy of quantum system at the ground state. In classical system, the lowest energy is effectively zero, but in the quantum system the lowest energy is always fluctuated due to the Heisenberg uncertainty. The muon has probability to leave the local minimum position due to the ZPE. The illustration of this condition in one dimension is given in the Fig. 4.13. The  $r_0$  indicates the local minimum position and the red path indicate the probability of muon's motion. In order to quantify the muon probability distribution, I solve Schrödinger for muon around the local minimum potentials inside cubic box. The cubic side,  $1.5 \text{ \AA}$ , is good enough to guarantee the total muon probability density inside the cubic box  $\sim 100\%$ . The detail is given in the appendix B.

The muon probability density for each muon site is given in the Fig 4.14. The muon probability density at each muon site are indicated by different color and does not connected each other. This means that there is no probability of the muon to hopping from one position to another position. The cross section of the muon probability density at each position are given in the Fig. 4.15. The minimum potential is located at the center of the

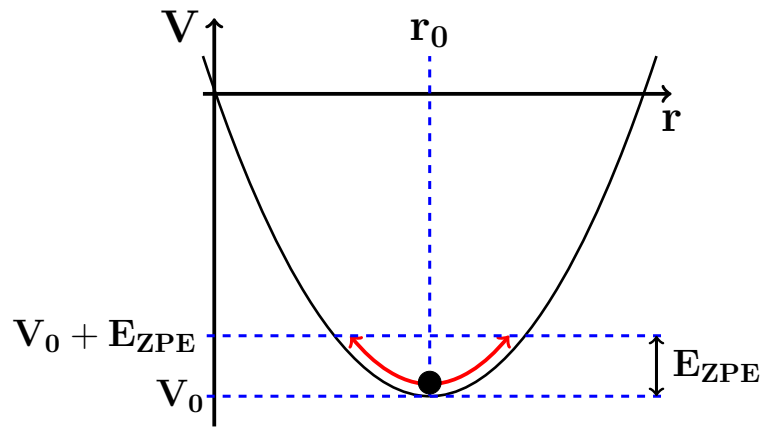


Figure 4.13: The illustration of the zero-point energy (ZPE) vibration of muon. The muon is not occupy single point but distributed around minimum potential.

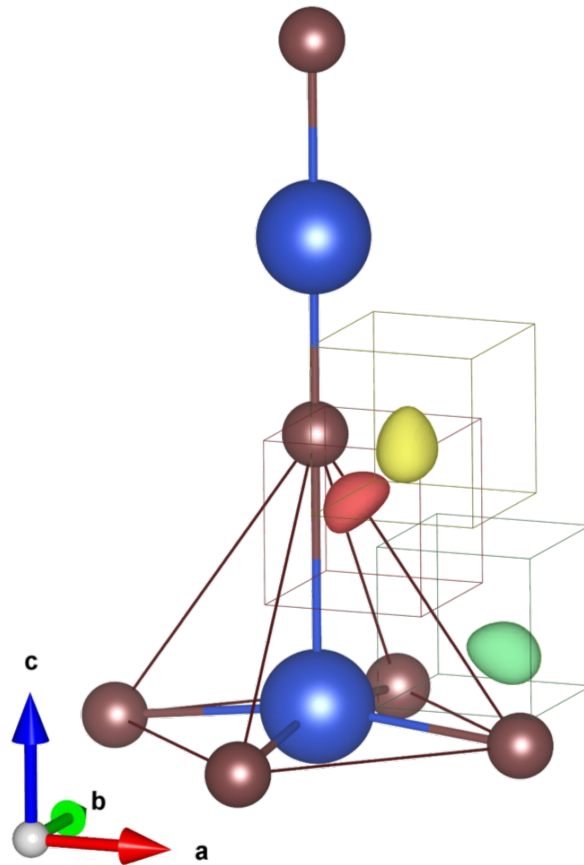


Figure 4.14: The muon probability density. The yellow, red and green area indicate the muon probability density of M1, M2, and M3 respectively at isosurface level  $1.5 \times 10^{-5}$ .

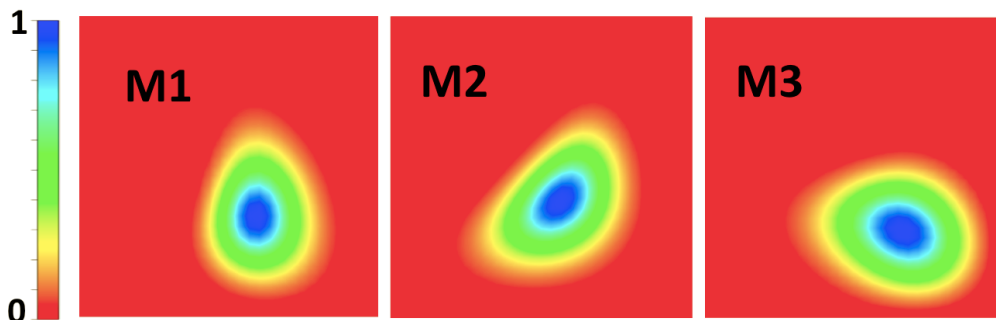


Figure 4.15: The muon probability density cross section. The local minimum potential is located at the center at each muon site. The highest muon probability density is away from most minimum potential due to the ZPE effect.

square. At the end, the internal field is evaluated following this equation.

$$\mathbf{B} = \sum_i \langle \psi_i | B_i | \psi_i \rangle \quad (4.1)$$

where  $\psi_i$  is the muon wave function at each grid point inside the cubic box and  $B_i$  is related internal field.

The Fig. 4.16 shows the internal field calculation including crystal deformation and quantum correction. As we can see in this figure, the M2 at  $U = 4$  eV seems to be realistic muon site owning internal fields 293.6 G, but M1 and M3 are not related to any experimental results. The another closer value to the 293.6 G is M3 at  $U = 5$  eV, but M2 is overestimated all experimental value. From this results, the point dipole model at which spin reside at the particular ion is not appropriate to explain the  $\mu$ SR experimental data of  $\text{YBa}_2\text{Cu}_3\text{O}_6$  even though we carefully consider local deformation of the crystal and quantum correction (zero point energy, ZPE) and tuning the  $U$  value.

## 4.4 The covalency effect

The covalency effect arises from the strong hybridization the Cu  $3d$ -orbital with surrounding O- $2p$  orbital. This effect causes the extension of the spin in the real space which is contrary with point dipole model, spin reside in particular ion. The DFT+ $U$  can give the description of the covalent nature in  $\text{CuO}_2$  plane. This effect is neglected in the analysis of previous  $\mu$ SR and neutron data on  $\text{YBa}_2\text{Cu}_3\text{O}_6$ , but this effect has found to be important to explain the missing neutron intensity in one dimensional cuprate,  $\text{Sr}_2\text{CuO}_3$ . The neutron diffraction is limited to observed the covalency effect in two dimensional cuprates because the spin density in the oxygen site is exactly cancel [37, 13]. Since the muon is very sensitive probe magnetism in the real space, muon can sense the covalency effect on the magnetism in two dimensional cuprates like  $\text{YBa}_2\text{Cu}_3\text{O}_6$ .

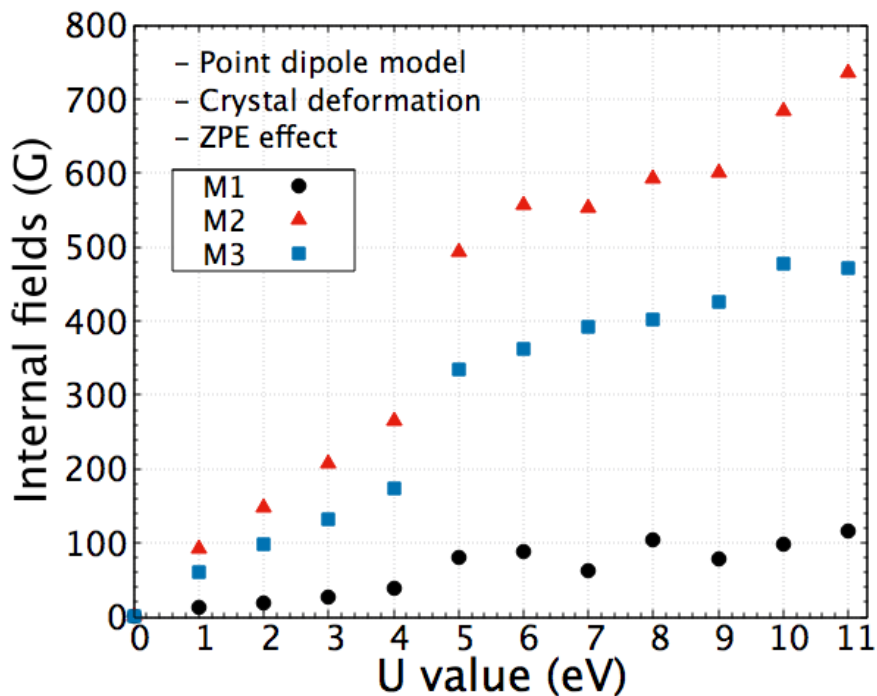


Figure 4.16: The calculated internal fields at muon site as function of the U based on point dipole model with crystal deformation and quantum correction.

The spin density from our DFT+U is shown in the Fig. 4.17. The green and red colour indicate the antiferromagnetic ordering. The spin density of the unperturbed system is shown in the Fig. 4.17 (a). The  $d$  orbital and  $p$  orbital character are clearly visualized at Cu site and planar O site, respectively. The total magnetic moment at planar oxygen site is effectively zero due to the symmetry of the spin density. In the perturbed system, the nearest atom to the muon is distorted from initial position. The spin density is also perturbed by presence of the muon as shown in the Fig. 4.17 (b), (c) and (d). This distortion lead to the change of the total value of the magnetic moment of nearest Cu and planar O. The value changing of the Cu moment is  $\sim 0.01 \mu_B$  and total magnetic moment at the oxygen site is  $\sim 0.02 \mu_B$ .

The internal evaluation with considering the covalency effect, using spin density model, is given in the Fig. 4.18. As the U value localize the electron and stabilized magnetic moment on the Cu site, the internal field at each site must be carefully evaluate as function of the U. The experimental internal field 293.6 G match to the calculated internal fields at M2 in the U value 5~7 eV with calculated internal field 284.26~324.69 G. In this U range, the other experimental internal field, 214.7 G, match with calculated internal field at M3, 206.50~241.15 G. The last experimental internal fields, 118.8 G, is set to be corresponded to the M1.

The total difference internal field from experiment and calculation is plotted as function of the U value as shown in the Fig. 4.19. This curve was fitting by fifth order polynomial

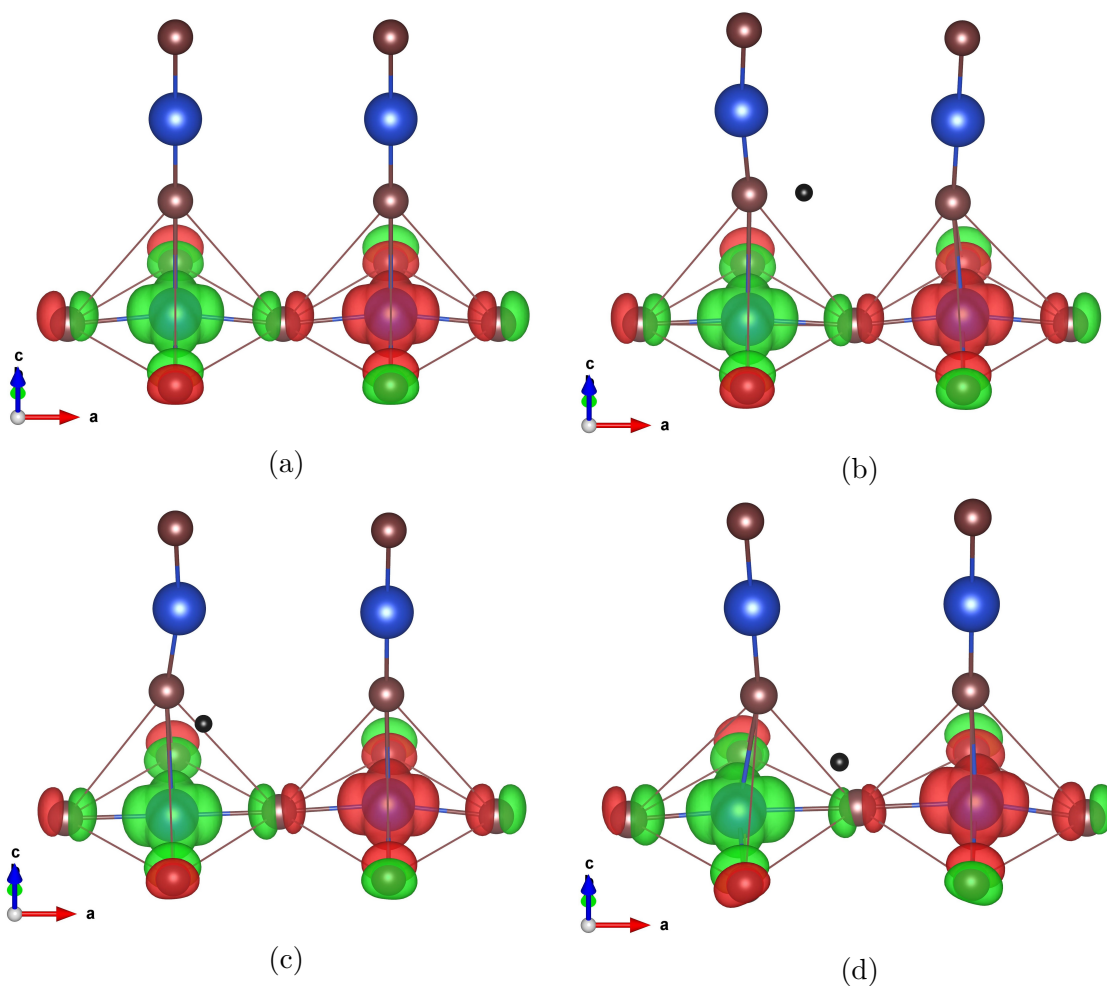


Figure 4.17: The muon perturbation to the spin density ion. (a) The unperturbed system in which the  $3d$  orbital of Cu and  $2p$  orbital of the planar O are clearly visualized. (b), (c) and (d) are perturbed system by muon at M1, M2, and M3, respectively. The muon perturbs the spin density which induces change in the total magnetic moment at neighboring ion.



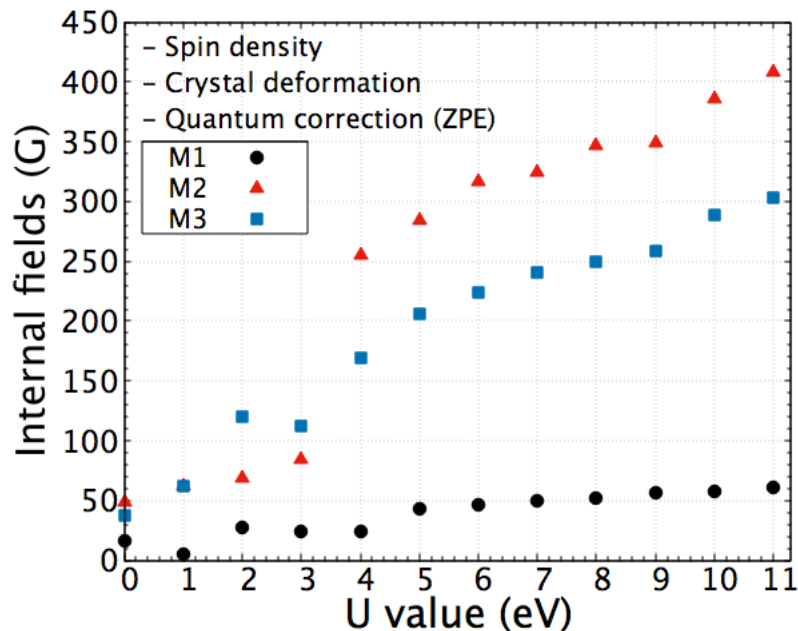


Figure 4.18: The calculated internal fields at muon site as function of the U based on spin density with crystal deformation and quantum correction.

function to obtain the optimum U value at which the difference is smallest. This optimum value is determined to be  $U = 6.6$  eV with total difference  $\sim 62.66$  G.

## 4.5 Discussion

The muon site identification is the central issue of  $\mu$ SR experiment because the muon spin precession frequency directly corresponds to the internal field at the muon site. Two methods of the muon site identification on the basis of the DFT calculation are: placing the muon in the randomly chosen low symmetry site [26] and the second one is determined by identifying the local minimum potential to be the muon position as the muon has a positive charge [29]. The first method argues that muon site determination on the basis of the local minimum potential is not appropriate, because the muon has zero point energy (ZPE) vibration and will be away from the minimum potentials. The muon site identification on the basis of the local potential must consider this effect and the possibility of muon jumping from one site to another site. The muon site identification by the local minimum potential method following the muon probability density calculation to judge the trapping muon site and how much the muon is away from the local minimum potential was done on the basis of an anharmonic potential model [31]. Even though this approach can give a better physical interpretation of the experimental results, the potential model might deviate from real conditions. Therefore, in this thesis, the potential around the local minimum position is interpolated from the DFT+U calculation, and the muon probability density calculation was done by a homemade program.

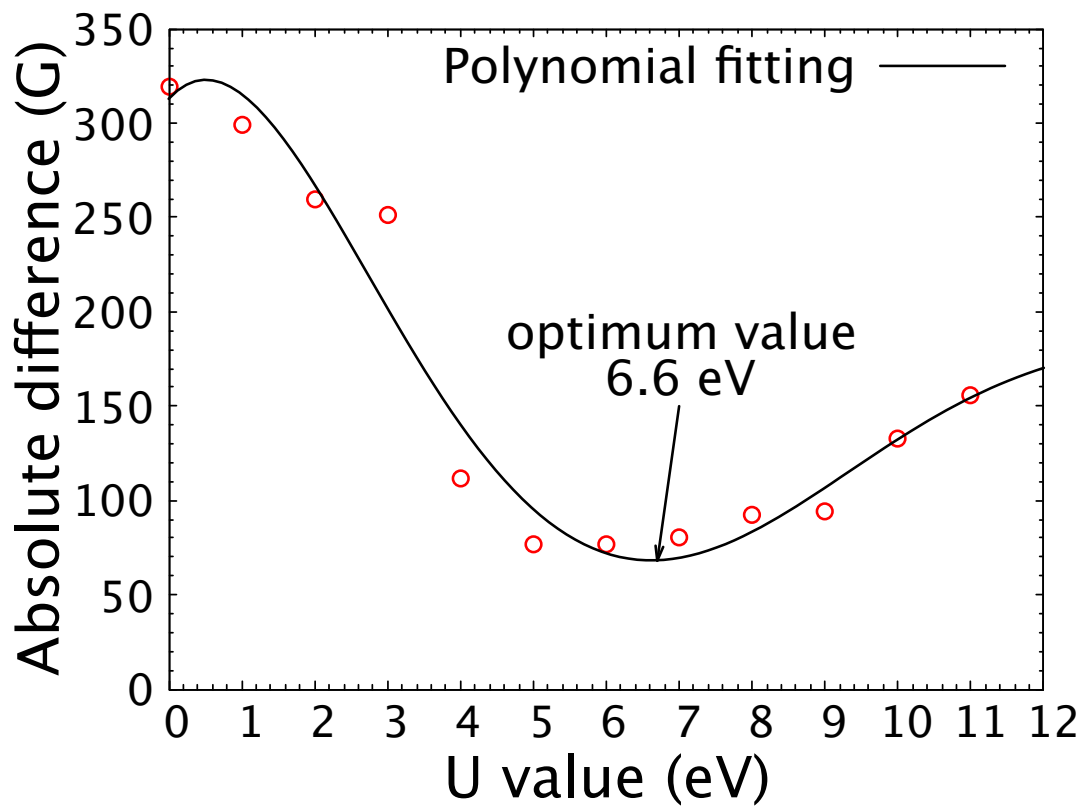


Figure 4.19: The polynomial fitting of the difference between experimental results and calculation as function of  $U$ . The lowest difference between experimental and calculation of the internal field is interpolated to be 6.6 eV.

described in the appendix B.

The ZPE energy of muon can be as large as 0.8 eV in F- $\mu$ -F molecule [26] and between 0.9 and 1.0 eV in quasi-one dimensional ferromagnet [27]. The ZPE at M1, M2 and M3 sites in  $\text{YBa}_2\text{Cu}_3\text{O}_6$  are 0.83, 0.82 and 0.76 eV, respectively. Due to the ZPE, the muon probability density is away from the local minimum potential which can be quantify in this thesis. From the fourier power intensity, mostly muon stop at M2 site. Beside muon delocalization of the muon due to the ZPE effect, there is also self trapping mechanism of muon around local minimum position [68].

As shown above, the point dipole model is not appropriate to discuss the spin state that is probed by  $\mu\text{SR}$  experiments. It has been shown the covalency effect on the magnetism can not be easily ignored. The covalency effect arises from hybridization between O  $2p$  orbital with Cu  $3d$  orbital has crucial effect on the spin density which directly interact with implanted muon. This effect has been found to be important in doping state leading to the Zhang-Rice singlet formation in which the hole doping reside in the oxygen side [69]. In the cuprate case, the spin density is extended to the planar oxygen site. The hyperfine tensor data analysis of planar  $^{17}\text{O}$  NMR spectra of  $\text{La}_2\text{CuO}_4$  show that  $\sim 31\%$  of spin density reside on the planar oxygen site [38]. In planar oxygen site, the spin up orbital correspond to the  $s + p_x$  symmetry and spin-down correspond to the  $s - p_x$  symmetry wherein net magnetic moment is zero [34]. The hybridization in cuprates is also pointed out by direct observation by ARPES and is found to be important control parameter for superconductivity. This results is supported by DFT+U calculation which demonstrate the powerful DFT in describing electronic structure of the high- $T_c$  cuprates [35].

The  $\text{Cu}^{2+}$  is  $3d^9$  system which has one unpaired electron and predicted to be has magnetic moment  $\sqrt{3} \mu_B$ . On the other hand neutron results is  $0.66 \mu_B$ . The reduction of magnetic moment is caused by spin-fluctuation. There are also fundamental issues in determination of magnetic moment from neutron diffraction which are overlap Bragg and magnetic peak and determination of the magnetic form factor. The point dipole model to calculate magnetic form factor in  $\text{Sr}_2\text{CuO}_3$ , one dimensional system, is failed to explain the missing neutron intensity in this system [37]. The neutron diffraction data in this system is well explained by considering covalency effect in the determination of the magnetic form factor which never been considered in the neutron data analysis of  $\text{YBa}_2\text{Cu}_3\text{O}_6$ . The covalency effect also contribute to the reduction of magnetic moment size from experimental results because spins are extended to the planar oxygen sites.

As  $\text{YBa}_2\text{Cu}_3\text{O}_6$  is a typical mott insulator, the Hubbard  $U$  is main parameter to tuning the magnetic moment at Cu  $3d^9$  site. The  $U = 9$  eV well reproduce the magnetic moment that deduced from neutron diffraction, magnetic moment per Cu =  $0.66 \mu_B$  which is ignored the covalency effect [13, 24]. The optimum value of  $U$  from polynomial fitting of the the absolute difference of internal field from experiment and calculation results is 6,6 eV. In another mother compound of the high- $T_c$  cuprates,  $\text{La}_2\text{CuO}_4$ , the  $U_{eff} = 6.5$  eV is well reproduced band-gap measured by photoinduced optical absorption spectroscopy [33].

The correspond calculated magnetic moment with the optimal value of the  $U$  for  $\text{YBa}_2\text{Cu}_3\text{O}_6$  is  $0.57 \mu_B$  per Cu(II). There is reduction of magnetic moment of the Cu due to the covalency effect  $\sim 14\%$  from the neutron diffraction results. The reduction of

the magnetic moment due to covalency effect also observed in other  $3d$  compound. The typical reduction of the  $\text{Fe}^{3+}$  moment due to the covalency effect in  $\text{Ca}_3\text{Fe}_2\text{Ge}_3\text{O}_{12}$  is  $\sim 14(2)\%$  [70] which compatible with the result that presented in this thesis. The reduction of the magnetic moment due to the strong Ir- $d$  and O- $p$  covalency also found in  $\text{SrM}\text{IrO}_6$  ( $M = \text{Ca, Mg}$ ) [71]. The difference magnetic moment size from the  $\mu\text{SR}$  and neutron is also caused by different fluctuation rate in the experiments technique. From the results in this thesis, we proposed that the reduction of magnetic moment from the theoretical prediction is due to the spin fluctuation and the covalency effect. The magnetic moment size also has dependence on the experimental technique.

The potential at M1 has the lowest energy following M2 and M3. On the other hand, the experimental data shows that the M2 has the highest Fourier intensity following M3 and M1 which indicates the M2 has the highest muon fraction following M3 and M1. The simulation to estimate the muon stability at each site is needed to confirm the muon fraction at each site which beyond this thesis scope. The biggest internal field different between experiment and calculation is M1, even though its Fourier intensity is small we can not be easily ignored. This signal is also reported by Nishida, *et.al* [21].



# Chapter 5

## Summary and Outlook

### 5.1 Summary

It has been demonstrated that the density functional theory (DFT) is powerful to reveal muon site in  $\text{YBa}_2\text{Cu}_3\text{O}_6$ . Three distinct muon sites have been determined which are consistent with the zero-field  $\mu\text{SR}$  experiments which its Fourier transform consists of three muon spin precession components. The muon perturbation to the host system can be quantified by introducing muon as an ultradilute impurity. The significant perturbation of the muon is found to be significant only to the neighboring ion.

The complete description of the muon behaviour in the  $\text{YBa}_2\text{Cu}_3\text{O}_6$  and how muon senses internal fields from surrounding electrical spins requires the quantum treatment of the muon itself as a muon is a fine particle and has zero-point energy vibration. The muon is not fixed in the single point position, but distributed around the local minimum potential. The muon probability density is determined from the spreading muon's wavefunction around the local minimum potential.

The internal fields calculation on the basis of dipole-dipole interaction between muon and the surrounding magnetic moment and spin reside in the particular ion, point dipole model, overestimates internal fields from the experiments. The correct interpretation of our  $\mu\text{SR}$  experimental data includes the covalency effect which electronic spin is extended in real space and a part of the spin density localizes in the planar oxygen sites. The neutron diffraction and NMR studies also point out this effect in another cuprate,  $\text{Sr}_2\text{CuO}_3$ , but neutron is unable to detect this effect in  $\text{YBa}_2\text{Cu}_3\text{O}_6$ . In parallel with the muon site identification, the spin density is also calculated by DFT. In  $\text{YBa}_2\text{Cu}_3\text{O}_6$ , the on-site Coulomb repulsive interaction among electrons parameter,  $U$ , plays a key role to open the gap at the Fermi level, localize the electron and stabilize magnetic moment. Thus the  $U$  value also gives a significant effect in the spin density. The careful tuning of the  $U$  value has been done in order to determine the best value of the  $U$  value for  $\text{YBa}_2\text{Cu}_3\text{O}_6$ .

The direct comparison of the internal fields at the muon site from our calculation and experiment reveals that the  $U$  value for  $\text{YBa}_2\text{Cu}_3\text{O}_6 \sim 6.6$  eV. This value also gives the correct band gap for  $\text{YBa}_2\text{Cu}_3\text{O}_6$  and is consistent with DFT+ $U$  and ARPES studies. We

also pointed out that the covalency effect plays a crucial role in the magnetism of  $\text{YBa}_2\text{Cu}_3\text{O}_6$ .

## 5.2 Outlook

In this thesis, the computational technique is developed in order to understand the physics from the  $\mu\text{SR}$  experiment. The further work is to justify the different Fourier intensity at each muon site which corresponds to the relative number of muons stopped at related positions. This computational technique is also able to be applied to other strongly correlated systems such as the pyrochlore system in which the correlation effect and strong orbital coupling are comparable.

# Appendix A

## The detail of the VASP calculations

In this thesis, I used the VASP version 5.4.4. The VASP program required at least 4 input file namely POSCAR, POTCAR, KPOINT, and INCAR files in the same directory. After calculaton finished, the outputs file are written in the same directory. There are some output file from VASP which are CHG, EIGENVAL, OSZICAR, CHGCAR IBZKPT, OUTCAR, REPORT, CONTCAR, PCDAT, WAVECAR, DOSCAR, KPOINTS, POSCAR, XDATCAR [72].

### A.1 Input file

#### A.1.1 INCAR

The INCAR file drives the calculation job. The calculation parameters are mainly set in the INCAR file. The typical INCAR file in this thesis is given as follows:

```
System = Y32Ba64Cu960192
```

```
PREC = Accurate
```

```
ISTART = 0
```

```
ICHARG = 2
```

```
IBRION = 1
```

```
NSW = 30
```

```
ISIF = 2
```

```
NELM = 300
```

```
EDIFF = 1E-4
```

```
EDIFFG = -0.05
```

```
POTIM = 1.5
```



```

ENCUT = 500

ISMear = 0
SIGMA = 0.05

LNONCOLLINEAR = .TRUE.
MAGMOM = 384*0 0.707 0.707 0 0.707 0.707 0 0.707 0.707 0 0.707 0.707 0 0.707 0.707 0 -0.707 -0.707
0 -0.707 -0.707 0 -0.707 -0.707 0 -0.707 -0.707 0 -0.707 -0.707 0 -0.707 -0.707 0 -0.707 -0.707 0
-0.707 0 -0.707 -0.707 0 -0.707 -0.707 0 -0.707 -0.707 0 -0.707 -0.707 0 -0.707 -0.707 0 -0.707
-0.707 0 -0.707 -0.707 0 0.707 0.707 0 0.707 0.707 0 0.707 0.707 0 0.707 0.707 0 0.707
0.707 0 0.707 0.707 0 0.707 0.707 0 0.707 0.707 0 0.707 0.707 0 -0.707
-0.707 0 -0.707 -0.707 0 -0.707 -0.707 0 -0.707 -0.707 0 -0.707 -0.707 0 -0.707 -0.707
0 -0.707 -0.707 0 -0.707 -0.707 0 -0.707 -0.707 0 0.707 0.707 0 0.707
0.707 0 0.707 0.707 0 0.707 0.707 0 0.707 0.707 0 0.707 0.707 0 0.707
0.707 0 0.707 0.707 0 0.707 0.707 0 0.707 0.707 0 0.707 0.707 0 0.707
0.707 0 0.707 0.707 0 0.707 0.707 0 0.707 0.707 0 0.707 0.707 0 -0.707
-0.707 0 -0.707 -0.707 0 -0.707 -0.707 0 -0.707 -0.707 0 -0.707 -0.707 0 -0.707 -0.707
0 -0.707 -0.707 0 -0.707 -0.707 0 -0.707 -0.707 0 576*0 0 0 0

LVTOT = .TRUE.
LVHAR = .TRUE.
LORBIT = 11
LAMBDA = 10
VOSKOWN = 1
GGA = 91
GGA_COMPAT = .FALSE.

# the Hubbard U parameter tag
LDAU = .TRUE.
LDAUTYPE = 2
LDAUL = -1 -1 2 -1 -1 !-1:none, 123:pdf-wave
LDAUU = 0.0 0.0 9.0 0.0 0.0
LDAUJ = 0.0 0.0 0.0 0.0 0.0
LDAUPRINT = 2
LMAXMIX = 4 !mixer quantum no.element: 4-d, 6-f

LREAL = Auto
LPLANE = .FALSE.
NSIM = 1

```

```
NELECT = 3200

# parameterization parameter
NPAR = 24
AMIX =0.2
BMIX = 0.0001
AMIX_MAG = 0.8
BMIX_MAG = 0.01
MAXMIX =120
NFREE = 20
```

The explanation of the same important tag in the INCAR file are given as follows:

- The System-tag contains the system name. This tag does not directly correspond to any calculation parameter.
- The PREC-tag determines the accuracy of the calculation. There are several options for this tag: PREC= Low — Medium — High — Normal — Accurate — Single. This tag controls the energy cut and the resolution of the FFT-grid. In this thesis, instead of automatic control of the energy cut for the plane wave by PREC-tag, I control manually by ENCUT-tag in order to make uniform calculation conditions for all calculation jobs.
- The ISTART-tag determines whether to continue calculation from existing WAVECAR or not. In this thesis, all calculations use ISTART=0, which starts the job from the scratch.
- The ICHARG-tag determines how the initial charge density is constructed. At the first self-consistent calculation, the ICHARG was set to be 2 (take superposition of atomic charge densities) for non-collinear calculation. But using the charge densities from this step, the calculation was continued to the non-collinear calculations by using ICHARG = 1.
- The IBRION-tag describes how the ion moves and relaxes to the ground state. I mostly use the conjugate gradient algorithm (IBRION=2) and quasi-Newton (variable metric) algorithm (IBRION=1).
- The EDIFF-tag determines the energy convergence threshold for the electronic self-consistent loop and the EDIFFG-tag determines the break condition for the ionic relaxation. The EDIFFG = -0.05 means that the relaxation will stop if all forces are smaller than 0.05 eV/Å.
- The MAGMOM-tag specifies the initial magnetic moment for each atom. The MAGMOM = 3 times of the number of ions in noncollinear calculations. The order follows the order of ions in the POSCAR file.

- The GGA-tag control the type of the GGA is used for the calculations. There are several option for this tag namely 91 — PE — RP — PS — AM. with the following meaning:

```

91   : Perdew -Wang 91
PE   : Perdew-Burke-Ernzerhof
RP   : revised Perdew-Burke-Ernzerhof
PS   : Perdew-Burke-Ernzerhof revised for solids.

```

- The LDAU-tag controls the onsite coulumb interaction (GGA+U or LDAU+U). The Hubbard U is introduced by LDAUTYPE-tag. the LDAUTYPE=1 follows the Liechtenstein formulation and LDAUTYPE=2 follows Duradev formulation which mainly used in this thesis. The LDAUL-tag specifies the l-quantum number of the atom following the order of the ion in the POSCAR. The LDAUL = -1 means no onsite Coulumb interaction, 1 for p orbital, 2 for d orbital and 3 for f orbital.
- The LDAUU specifies the strength of the effective on-site Coulomb interactions and the LDAUJ specifies the strength of the effective on-site exchange interactions. The order is also follow the order of the atom in POSCAR.
- The NELECT-tag determiner the number of the electron in the system. When introduce muon as hydrogen ion, the NELECT is set to be total electron-1 to compensate the positive charge of the muon.

### A.1.2 POSCAR

The POSCAR contains the structural parameter of the system. The unitcell POSCAR can be easily convert from the crystallography information file (CIF) and for the supercell construction is made by VESTA [73]. The typical POSCAR file that was used in this thesis is given as follows:

```

ba2 cu3 o6 y
1.0
15.4600000381      0.0000000000      0.0000000000
0.0000000000      15.4600000381      0.0000000000
0.0000000000      0.0000000000      23.7040004730
Y   Ba   Cu   O   H
32  64   96  192  1
Direct
0.125000000      0.125000000      0.250000000
0.125000000      0.125000000      0.749999980
0.125000000      0.625000023      0.250000000
...

```

The first line is comment where we can write down the name of the system. The second line is the scale factor for the lattice parameter and atomic coordinates. On the following three give the unit cell of the system. the sixth line supplies the atomic species and the following line is the number of the corresponding atom. The seventh line supplies the switch between cartesian and direct lattice and the following number is three dimension of the atomic position.

### A.1.3 POTCAR

The POTCAR file contains the pseudopotential for each atomic species used in the calculation. The order of each POTCAR file of the atom must be follow the order of the atom in the POSCAR file. The POTCAR file that used in this thesis is given as follows:

```
PAW_GGA Y_sv 10Feb1998
11.0000000000000000
parameters from PSCTR are:
VRHFIN =Y: 4s4p5s4d
LEXCH  = 91
EATOM  = 1047.6225 eV,   76.9981 Ry

TITEL  = PAW_GGA Y_sv 10Feb1998
LULTRA =          F    use ultrasoft PP ?
IUNSCR =          1    unscreen: 0-lin 1-nonlin 2-no
RPACOR =    2.200    partial core radius
POMASS =  88.906; ZVAL  =   11.000    mass and valenz
RCORE  =    2.600    outmost cutoff radius
RWIGS  =    3.430; RWIGS =    1.815    wigner-seitz radius (au A)
ENMAX  = 211.698; ENMIN = 158.774 eV
RCLOC  =    2.212    cutoff for local pot
LCOR   =          T    correct aug charges
LPAW   =          T    paw PP
EAUG   = 363.258
DEXC   =    .000
RMAX   =    3.169    core radius for proj-oper
RDEP   =    2.745    core radius for depl-charge
QCUT   = -3.945; QGAM  =    7.889    optimization parameters
...
End of Dataset
PAW_GGA Ba_sv 14Apr2000
10.0000000000000000
parameters from PSCTR are:
VRHFIN =Ba: 5s5p6s
```

```
LEXCH = 91
EATOM = 701.3292 eV, 51.5462 Ry

TITEL = PAW_GGA Ba_sv 14Apr2000
LULTRA = F use ultrasoft PP ?
IUNSCR = 1 unscreen: 0-lin 1-nonlin 2-no
RPACOR = 2.400 partial core radius
POMASS = 137.327; ZVAL = 10.000 mass and valenz
RCORE = 2.800 outmost cutoff radius
RWIGS = 3.740; RWIGS = 1.979 wigner-seitz radius (au A)
ENMAX = 187.204; ENMIN = 140.403 eV
RCLOC = 2.516 cutoff for local pot
LCOR = T correct aug charges
LPAW = T paw PP
EAUG = 351.165
DEXC = .000
RMAX = 3.370 core radius for proj-oper
RAUG = 1.300 factor for augmentation sphere
RDEP = 2.976 core radius for depl-charge
QCUT = -3.709; QGAM = 7.419 optimization parameters
...
End of Dataset
PAW_GGA Cu 05Jan2001
11.0000000000000000
parameters from PSCTR are:
VRHFIN =Cu: d10 p1
LEXCH = 91
EATOM = 1393.0707 eV, 102.3878 Ry

TITEL = PAW_GGA Cu 05Jan2001
LULTRA = F use ultrasoft PP ?
IUNSCR = 1 unscreen: 0-lin 1-nonlin 2-no
RPACOR = 2.000 partial core radius
POMASS = 63.546; ZVAL = 11.000 mass and valenz
RCORE = 2.300 outmost cutoff radius
RWIGS = 2.480; RWIGS = 1.312 wigner-seitz radius (au A)
ENMAX = 273.246; ENMIN = 204.934 eV
RCLOC = 1.712 cutoff for local pot
LCOR = T correct aug charges
LPAW = T paw PP
EAUG = 516.456
```

```
DEXC = -.002
RMAX = 2.789 core radius for proj-oper
RAUG = 1.300 factor for augmentation sphere
RDEP = 2.302 core radius for depl-charge
QCUT = -4.481; QGAM = 8.963 optimization parameters
...
End of Dataset
PAW_GGA O 05Jan2001
6.000000000000000000
parameters from PSCTR are:
VRHFIN =0: s2p4
LEXCH = 91
EATOM = 433.0277 eV, 31.8266 Ry

TITEL = PAW_GGA O 05Jan2001
LULTRA = F use ultrasoft PP ?
IUNSCR = 0 unscreen: 0-lin 1-nonlin 2-no
RPACOR = .000 partial core radius
POMASS = 16.000; ZVAL = 6.000 mass and valenz
RCORE = 1.520 outmost cutoff radius
RWIGS = 1.550; RWIGS = .820 wigner-seitz radius (au A)
ENMAX = 400.000; ENMIN = 300.000 eV
ICORE = 2 local potential
LCOR = T correct aug charges
LPAW = T paw PP
EAUG = 605.392
DEXC = .000
RMAX = 2.264 core radius for proj-oper
RAUG = 1.300 factor for augmentation sphere
RDEP = 1.550 radius for radial grids
QCUT = -5.520; QGAM = 11.040 optimization parameters
....
End of Dataset
PAW_GGA H 07Jul1998
1.000000000000000000
parameters from PSCTR are:
VRHFIN =H: ultrasoft test
LEXCH = 91
EATOM = 12.5313 eV, .9210 Ry

TITEL = PAW_GGA H 07Jul1998
```

```

LULTRA =      F    use ultrasoft PP ?
IUNSCR =      0    unscreen: 0-lin 1-nonlin 2-no
RPACOR =     .000  partial core radius
POMASS =  0.1111; ZVAL =  1.000    mass and valenz
RCORE =     1.100  outmost cutoff radius
RWIGS =     .700; RWIGS =     .370  wigner-seitz radius (au A)
ENMAX =  250.000; ENMIN =  200.000 eV
RCLOC =     .701  cutoff for local pot
LCOR =      T    correct aug charges
LPAW =      T    paw PP
EAUG =  400.000
RMAX =     2.174  core radius for proj-oper
RAUG =     1.200  factor for augmentation sphere
RDEP =     1.112  core radius for depl-charge
QCUT =   -5.749; QGAM =  11.498    optimization parameters
...
End of Dataset

```

The type of the pseudopotentials and exchange correlation function that used in this thesis are projected augmented wave (PAW) and GGA in the Perdew-wang 91 as written in the INCAR file. The electron that treated as outer (valence) electrons for each atom is given in the line VRHFIN for each atom.

### A.1.4 KPOINTS

The KPOINTS contains the information of the k-points coordinates and mesh size. The typical KPOINTS file is describe as follows:

```

YBa2Cu3O6
0
Monkhorst
5 5 5      ! subdivisions N_1, N_2 and N_3 along recipr. l. vectors
0. 0. 0.   ! optional shift of the mesh (s_1, s_2, s_3)

```

The first line is treated as comments. The 0 in second line means the automatic k-mesh generation and the following line indicate automatic k-mesh generation following Monkhorst-pack scheme [74].

## A.2 OUTPUT

The important OUTPUT file after the electronic and ionic relaxation are:

- The CONTCAR file contains the atomic position after relaxation with same format with the POSCAR file.
- The LOCPOT file contains the total local potential in eV. The Potential map can be easily transfer to the VESTA program. To write this file, the line `LVTOT = .TRUE.` must be added in the INCAR file.
- The CHGCAR file contains the total charge density multiplied by the volume,  $\rho(r) * V_{\text{cell}}$ . The density is written using the following commands Fortran:

```
WRITE(IU,FORM) (((C(NX,NY,NZ),NX=1,NGXC),NY=1,NGYZ),NZ=1,NGZC)
```

The x index is the fastest index, and the z index the slowest index. For spinpolarized calculations, two sets of data can be found in the CHGCAR file. The first set contains the total charge density (spin up plus spin down), the second one the magnetization density (spin up minus spin down). For non collinear calculations the CHGCAR file contains the total charge density and the magnetisation density in the x, y and z direction in this order. This can be easily visualized by VESTA.

The internal fields calculation on the basis of the spin density from DFT+U calculations was done by read the LOCPOT in order to get the potential around muon positions for the zero-point energy (ZPE) and read CHGCAR to get the magnetization density. The description of the program to read those file and used them in the internal fields calculations is given in the appendix B.

## A.3 Implementation in the Supercomputer

The VASP program is written by Fortran 90 which has flexebility to do parallel computing by simply apply the MPI (Message Passing Interface) library. The paralelization in the VASP can be done by parallelization and data distribution over bands and/or over plane wave coefficients (NCORE and NPAR) and parallelization over k-points (KPAR). In this thesis, the paralelization was done by NPAR parameter, over bands. The NPAR controls the number of bands that are treated in parallel. On massively parallel systems and modern multi-core machines, the recommend setting is

$$\text{NPAR} = \approx \sqrt{\text{number of cores}} \quad (\text{A.1})$$

or

$$\text{NPAR} = \text{number of cores per compute node} \quad (\text{A.2})$$

The calculation in this thesis is mainly in the Big Waterfall Massively Parallel Computer (BWMPC) in HOKUSAI supercomputer, ACCC RIKEN [65]. The Massively Parallel Computer (BWMPC) comprises 840 nodes of CX2550 M4. Each node provides a theoretical peak performance of 3.07 TFLOPS and a memory capacity of 96 GB. The InfiniBand



EDR of 12.6 GB/s is used to connect each node to enable high performance communication and file sharing. The typical calculation used 192 cores in the 8 computer node with the following details bash file:

```
#!/bin/sh
#-----pjsoption-----#
#PJM -L rscunit=bwmpc
#PJM -L rscgrp=batch
#PJM -L vnode=8
#PJM -L vnode-core=30
#PJM -L elapse=24:00:00
#PJM -g G18022
#PJM -j
#-----Program execution-----#
mpirun -np 192 -ppn 24 /vasp.5.4.4/vasp_BW/bin/vasp_ncl
```

# Appendix B

## The dipole-field calculation program

The internal fields at the muon site was calculated on the basis dipole-dipole interaction between muon and localized magnetic moment in the system with considering local crystal deformation, zero point energy (ZPE) of muon and covalency effect (using spin density from CHGCAR instead using localized point dipole at Cu-site). The detail flowchart of the program is given as follow:

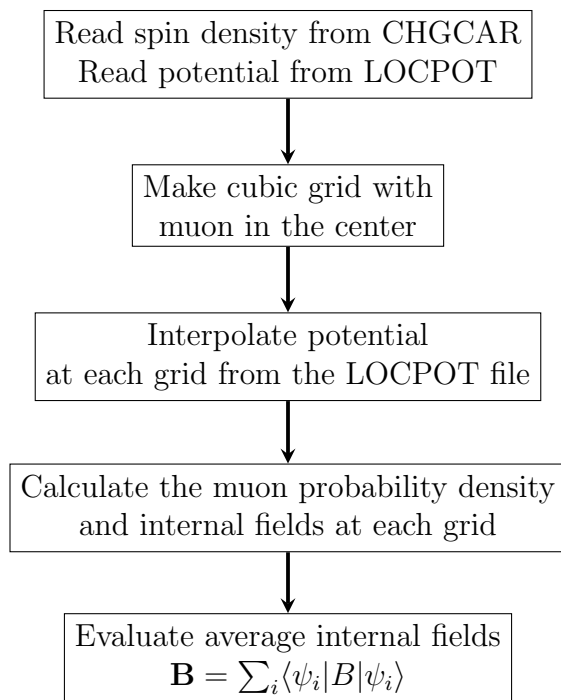


Figure B.1: The folow chart of dipole field program.

As described in the flowchart, the first step is read spin density from CHGCAR and potential from the LOCPOT file. Since the VASP was written by Fortran 90, It is very flexuble to do post processing by using Fortran 90. The following line is to read CHGCAR.

```

!=====READ CHGCAR FILE=====
!write(*, "('', a)") trim(CHGCAR)
open(unit=10, file = "CHGCAR", action="read")
read(10,*)      ! SKIP MOLECULAR STRUCTURE
read(10,*) sf   ! SCALE FACTOR
read(10,*) latt ; latt = sf*latt(:, :)

Mu = Mu(1)*latt(1,:) + Mu(2)*latt(2,:) + Mu(3)*latt(3,:)
Vol = latt(1,1)*latt(2,2)*latt(3,3)

rewind(10)
nline = 1
read(10, "(a)") line
do while (.not. line == "")
read(10, "(a)") line
nline = nline + 1
end do
read(10,*) ngx, ngy, ngz
allocate(rho(ngx, ngy, ngz))
! READ TOTAL CHARGE DENSITY
read(10,*) ((rho(i, j, k), i = 1, ngx), j = 1, ngy), k = 1, ngz)
! READ MAGNETIZATION DENSITY IN X-DIRECTION
io = 1 ! skip augmentation occupancies
do while (io /= 0)
read (10, "(3i5)", iostat = io) ngx1, ngy1, ngz1
end do
allocate(mag_x(ngx1, ngy1, ngz1))
read(10,*) ((mag_x(i, j, k), i = 1, ngx1), j = 1, ngy1), k = 1, ngz1)
mag_x = mag_x / vol
! READ MAGNETIZATION DENSITY IN Y-DIRECTION
io = 1
do while (io /= 0)
read (10, "(3i5)", iostat = io) ngx2, ngy2, ngz2
end do
allocate(mag_y(ngx2, ngy2, ngz2))
read(10,*) ((mag_y(i, j, k), i = 1, ngx2), j = 1, ngy2), k = 1, ngz2)
mag_y = mag_y / Vol
! READ MAGNETIZATION DENSITY IN Z-DIRECTION
io = 1
do while (io /= 0)
read (10, "(3i5)", iostat = io) ngx3, ngy3, ngz3

```

```

end do
allocate(mag_z(ngx3, ngy3, ngz3))
read(10,*) (((mag_z(i, j, k), i = 1, ngx3), j = 1, ngy3), k = 1, ngz3)
mag_z = mag_z / Vol
close(10)

```

and the following line to read the LOCPOT file :

```

!=====READ LOCPOT=====
open(unit=13, file="LOCPOT", action="read ")
nline = 1
read(13, "(a)") line
!read Header
do while (.not. line == "")
read(13, "(a)") line
nline = nline + 1
end do
read(13,*) ngx, ngy, ngz
allocate(loc(ngx,ngy,ngz))
read(13,*) (((loc(i, j, k), i = 1, ngx), j = 1, ngy), k = 1, ngz )
NX = size(loc)
close(13)
!=====

```

The next step is making grid and interpolate potential in each point in this grid:

```

allocate(V(N(1), N(2), N(3)))
do k = 1, N(3)
do j = 1, N(2)
do i = 1, N(1)
V(i, j, k) = interpolate(xc, yc, zc, Vs, xi(i), yi(j), zi(k))
end do
end do
end do

```

To calculate the muon probability density, the Schrödinger for muon inside the cubic by finite difference method [75] by transform the the Schrödinger in to the matrix equation and solve the eigenvalue and eigenfunction. The following line is to construct the matrix from the the Schrödinger equation:

```

k1 = hbar**2 / (2*mas) * 6.24150934E-2
M = 1; L = 1
dx = ((maxval(xi)-minval(xi))/(N(1)))**2 ; dx = k1 / dx

```

```

dy = ((maxval(yi)-minval(yi))/(N(2)))**2 ; dy = k1 / dy
dz = ((maxval(zi)-minval(zi))/(N(3)))**2 ; dz = k1 / dz
allocate(A(size(Vi),size(Vi)))
do i = 1, size(Vi)
  if (i > 1+(M-1)*N(1)) then ; A(i,i-1) = A(i,i-1) + dx ; end if
  if (i < M*N(1)) then ; A(i,i+1) = A(i,i+1) + dx ; end if
  if (i > N(1)*(N(2)*(L-1)+1)) then ; a(i,i-N(1)) = a(i,i-N(1)) + dy ;
  end if
  if (i <= N(1)*(N(2)*L-1)) then ; A(i,i+N(1)) = A(i,i+(N(1))) + dy ;
  end if
  if (i > N(1)*N(2)) then ; A(i,i-N(1)*N(2)) = A(i,i-N(1)*N(2)) + dz ;
  end if
  if (i <= N(1)*N(2)*(N(3)-1)) then ; A(i,i+N(1)*N(2)) = A(i,i+N(1)*N(2))
  + dz ; end if
  A(i,i) = -(2*dx + 2*dy + 2*dz + Vi(i));
  if (i/N(1) == M) then ; M = M+1; end if
  if ((M-1)/N(2) == L) then ; L = L+1; end if
end do

```

To solve this matrix, the subroutine "dsyev" from LAPACK library was used.

```

subroutine solve_matrix(A,eig,n)
implicit none
integer(kind=8) :: n, l, inf
real(kind=8) :: A(n,n), eig(n), work(n*(3+n/2))
l = n*(3+n/2)
call dsyev('V','U',n,A,n,eig,work,l,inf)
end subroutine

```

The following line is to calculate the internal fields at each grid :

```

do ii = 1, nn
H1 = 0
H2 = 0
H3 = 0
!$acc region
do i = -dmax(1), dmax(1)
xgr = xg + i
do j = -dmax(2), dmax(2)
ygr = yg + j
do k = -dmax(3), dmax(3)
zgr = zg + k

```

```

xr = (xia(ii) - xgr*latt(1,1))*1E-8
yr = (yia(ii) - ygr*latt(2,2))*1E-8
zr = (zia(ii) - zgr*latt(3,3))*1E-8
R = sqrt(xr**2 + yr**2 + zr**2)
SR = Sx_out*xr + Sy_out*yr + Sz_out*zr
do rr = 1, size(R)
if (R(rr) > dt*1E-8 .and. R(rr) <= Rmax*1E-8) then
H1 = H1 + (3*xr(rr)*SR(rr) - Sx_out(rr)*(R(rr)**2))/(R(rr)**5)
H2 = H2 + (3*yr(rr)*SR(rr) - Sy_out(rr)*(R(rr)**2))/(R(rr)**5)
H3 = H3 + (3*zr(rr)*SR(rr) - Sz_out(rr)*(R(rr)**2))/(R(rr)**5)
end if
end do
end do
end do
end do
!$acc end region
Hx(ii) = H1 - Hx_out1(ii) + Hx_0(ii)
Hy(ii) = H2 - Hy_out1(ii) + Hy_0(ii)
Hz(ii) = H3 - Hz_out1(ii) + Hz_0(ii)
write(*,*) ii
write(*,*) Hx(ii), Hy(ii), Hz(ii)

end do

```

Since this calculation step is very heavy, this job is done by GPU computing which use of a GPU (graphics processing unit) as a co-processor to accelerate CPUs computing. The GPU has ability do the massive parallel computation. The typical GPU that used for my calculation is NVIDIA TITAN X which has 3584 cores. The line !\$acc region and !\$acc end region are commands to communicate between GPU and CPU.

At the end the internal fields at the muon site is evaluated by the following line:

```

allocate(phi(nA))
phi = A(:,nA)
phi = phi*phi

Ha = sum(phi*Hx)
Hb = sum(phi*Hy)
Hc = sum(phi*Hz)
H = sqrt(Ha**2 + Hb**2 + Hc**2)

```



# Appendix C

## Internal fields calculations results

Table C.1: The internal field at each muon sites as function of the U value. This calculation is on the basis point dipole model

U (eV)	Internal magnetic field (G)		
	M1	M2	M3
0	0.28	1.69	0.75
1	18.89	112.90	49.79
2	30.07	179.70	79.26
3	42.38	253.28	111.70
4	54.12	323.47	142.66
5	103.49	618.49	272.78
6	111.16	664.36	293.00
7	118.55	649.97	312.48
8	126.28	692.38	332.87
9	134.59	737.89	354.75
10	143.17	784.96	505.97
11	152.04	833.58	737.31
Exp.	118.8	293.6	214.7



Table C.2: The internal field at each muon sites as function of the U value. This calculation is on the basis point dipole model by including lattice deformation

U (eV)	Internal magnetic field (G)		
	M1	M2	M3
0	0.33	1.35	0.71
1	23.31	90.23	50.58
2	34.22	143.83	81.24
3	48.12	202.39	118.87
4	55.87	257.19	147.77
5	114.61	459.48	281.46
6	142.15	513.99	307.19
7	140.36	536.54	333.83
8	156.70	576.12	327.44
9	151.35	571.04	329.44
10	169.33	650.50	406.87
11	188.18	673.49	422.89
Exp.	118.8	293.6	214.7

Table C.3: The internal field at each muon sites as function of the U value. This calculation is on the basis point dipole model by including lattice deformation and zero point energy vibration

U (eV)	Internal magnetic field (G)		
	M1	M2	M3
0	0.19	1.38	0.88
1	13.63	92.83	60.79
2	19.79	147.24	98.26
3	26.68	207.05	132.70
4	38.83	265.40	174.36
5	79.74	493.51	334.77
6	87.79	557.18	363.09
7	63.51	552.59	391.54
8	104.03	592.72	401.33
9	78.01	600.15	426.97
10	98.92	683.81	477.38
11	115.70	734.92	471.52
Exp.	118.8	293.6	214.7

Table C.4: The internal field at each muon sites as function of the U value. This calculation is on the basis spin density (the extended spin in the real space due to the covalency effect) by including lattice deformation and zero point energy vibration

U (eV)	Internal magnetic field (G)		
	M1	M2	M3
0	16.34	48.58	37.42
1	5.60	62.45	62.24
2	27.93	69.20	119.99
3	24.11	84.38	111.94
4	24.59	254.82	169.06
5	42.60	284.26	206.50
6	45.97	316.64	223.96
7	49.35	324.69	241.15
8	52.51	347.05	249.74
9	56.05	348.99	258.36
10	58.09	386.30	288.23
11	61.20	408.05	303.73
Exp.	118.8	293.6	214.7



# Bibliography

- [1] H. K. Onnes, Commun. Phys. Lab. Univ. Leiden **120b**, **122b**, **124c** (1911).
- [2] J. Bardeen, L. N. Cooper, and J. R. Schrieffer, Physical Review **108**, 1175 (1957).
- [3] J. Bardeen, L. N. Cooper, and J. R. Schrieffer, Physical Review **106**, 162 (1957).
- [4] C. Kittel, *Introduction to Solid State Physics*, Wiley, 8 edition, 2004.
- [5] B. Keimer, S. A. Kivelson, M. R. Norman, S. Uchida, and J. Zaanen, Nature **518**, 179 (2015).
- [6] J. Nagamatsu, N. Nakagawa, T. Muranaka, Y. Zenitani, and J. Akimitsu, Nature **410**, 63 (2001).
- [7] J. G. Bednorz and K. A. Müller, Z. Physik B - Condensed Matter **64**, 189 (1986).
- [8] M. K. Wu et al., Physical Review Letters **58**, 908 (1987).
- [9] F. London and H. London, Proceedings of the Royal Society of London. Series A - Mathematical and Physical Sciences **149**, 71 (1935).
- [10] Y. Koike and T. Adachi, J. Phys. Soc. Jpn. **85**, 091006 (2016).
- [11] N. Nishida et al., Jpn. J. Appl. Phys. **26**, L1856 (1987).
- [12] R. F. Kiefl et al., Physical Review Letters **63**, 2136 (1989).
- [13] J. M. Tranquada et al., Physical Review B **38**, 2477 (1988).
- [14] J. M. Tranquada et al., Physical Review Letters **60**, 156 (1988).
- [15] T. J. Jackson et al., Physical Review Letters **84**, 4958 (2000).
- [16] Y. J. Uemura et al., Physical Review Letters **62**, 2317 (1989).
- [17] J. E. Sonier et al., Phys. Rev. Lett. **83**, 4156 (1999).
- [18] S. Sanna, G. Allodi, G. Concas, A. D. Hillier, and R. D. Renzi, Physical Review Letters **93** (2004).

- 
- [19] C. Niedermayer et al., Physical Review Letters **80**, 3843 (1998).
- [20] R. I. Miller et al., Physical Review B **73** (2006).
- [21] N. Nishida and H. Miyatake, Hyperfine Interact **63**, 183 (1991).
- [22] M. Weber et al., Hyperfine Interact **63**, 207 (1991).
- [23] Q. Li and J. H. Brewer, Hyperfine Interact **63**, 169 (1991).
- [24] G. M. Lopez, A. Filippetti, M. Mantega, and V. Fiorentini, Physical Review B **82** (2010).
- [25] W. E. Pickett, Reviews of Modern Physics **61**, 433 (1989).
- [26] J. S. Möller, D. Ceresoli, T. Lancaster, N. Marzari, and S. J. Blundell, Physical Review B **87** (2013).
- [27] S. J. Blundell et al., Physical Review B **88** (2013).
- [28] F. Xiao et al., Physical Review B **91** (2015).
- [29] F. Bernardini, P. Bonfà, S. Massidda, and R. De Renzi, Physical Review B **87** (2013).
- [30] F. Lang et al., Physical Review B **94** (2016).
- [31] S. C. Cheung et al., Physical Review B **97** (2018).
- [32] Y. Tokura and N. Nagaosa, Science **288**, 462 (2000).
- [33] M. Haruta et al., Journal of Applied Physics **114**, 083712 (2013).
- [34] C. Lane et al., Physical Review B **98** (2018).
- [35] C. E. Matt et al., Nature Communications **9**, 972 (2018).
- [36] P. W. Anderson, Science **235**, 1196 (1987).
- [37] A. C. Walters et al., Nature Physics **5**, 867 (2009).
- [38] R. E. Walstedt and S.-W. Cheong, Physical Review B **64** (2001).
- [39] S. J. Blundell, Contemporary Physics **40**, 175 (1999).
- [40] J. H. Brewer and R. Cywinski,  *$\mu$ SR : an introduction*, Scottish Universities Summer School in Physics and Institute of Physics, London, 1999.
- [41] J. E. Sonier, Muon Spin Rotation/Relaxation/Resonance ( $\mu$ SR) brochure, <http://musr.ca/intro/musr/musrbrochure.pdf>.

- [42] G. M. Luke et al., Phys. Rev. Lett. **73**, 1853 (1994).
- [43] PSI , <https://www.isis.stfc.ac.uk/pages/2014-morenzoni-psi.pdf>.
- [44] F. Pratt, Physica B: Condensed Matter **289-290**, 710 (2000).
- [45] W. Kohn, Reviews of Modern Physics **71**, 1253 (1999).
- [46] P. Hohenberg and W. Kohn, Physical Review **136**, B864 (1964).
- [47] W. Kohn and L. J. Sham, Physical Review **140**, A1133 (1965).
- [48] M. T. Lusk and A. E. Mattsson, MRS Bulletin **36**, 169 (2011).
- [49] R. O. Jones and O. Gunnarsson, Reviews of Modern Physics **61**, 689 (1989).
- [50] D. M. Ceperley and B. J. Alder, Physical Review Letters **45**, 566 (1980).
- [51] J. P. Perdew and A. Zunger, Physical Review B **23**, 5048 (1981).
- [52] S. H. Vosko, L. Wilk, and M. Nusair, Canadian Journal of Physics **58**, 1200 (1980).
- [53] J. P. Perdew and Y. Wang, Physical Review B **45**, 13244 (1992).
- [54] J. P. Perdew, K. Burke, and M. Ernzerhof, Physical Review Letters **77**, 3865 (1996).
- [55] B. Hammer, L. B. Hansen, and J. K. Nørskov, Physical Review B **59**, 7413 (1999).
- [56] D. R. Hamann, M. Schlüter, and C. Chiang, Physical Review Letters **43**, 1494 (1979).
- [57] D. Vanderbilt, Phys. Rev. B **41**, 7892 (1990).
- [58] P. E. Blöchl, Phys. Rev. B **50**, 17953 (1994).
- [59] G. Kresse and D. Joubert, Phys. Rev. B **59**, 1758 (1999).
- [60] J. Orenstein, Science **288**, 468 (2000).
- [61] A. I. Liechtenstein, V. I. Anisimov, and J. Zaanen, Phys. Rev. B **52**, R5467 (1995).
- [62] S. L. Dudarev, G. A. Botton, S. Y. Savrasov, C. J. Humphreys, and A. P. Sutton, Physical Review B **57**, 1505 (1998).
- [63] G. Kresse and J. Furthmüller, Physical Review B **54**, 11169 (1996).
- [64] G. Kresse and J. Furthmüller, Computational Materials Science **6**, 15 (1996).
- [65] HOKUSAI , RIKEN, <http://accr.riken.jp/en/tag/hokusai/>.
- [66] J. H. Brewer et al., Physical Review Letters **60**, 1073 (1988).

- [67] G. Roth et al., *Zeitschrift für Physik B Condensed Matter* **69**, 53 (1987).
- [68] G. Prando et al., *Phys. Rev. B* **87**, 064401 (2013).
- [69] F. C. Zhang and T. M. Rice, *Physical Review B* **37**, 3759 (1988).
- [70] V. P. Plakhty, A. G. Gukasov, R. J. Papoular, and O. P. Smirnov, *Europhysics Letters (EPL)* **48**, 233 (1999).
- [71] S. Bhowal and I. Dasgupta, *Phys. Rev. B* **97**, 024406 (2018).
- [72] G. Kresse, M. Marsman, and J. Furthmüller, *VASP the GUIDE*, 2018.
- [73] K. Momma and F. Izumi, *Journal of Applied Crystallography* **44**, 1272 (2011).
- [74] H. J. Monkhorst and J. D. Pack, *Phys. Rev. B* **13**, 5188 (1976).
- [75] Z. Romanowski, *Molecular Physics* **109**, 2679 (2011).

# Irwan Ramli



## PERSONAL DETAIL

---

Place, date of birth : West celebes, Indonesia, March 12, 1989  
Nationality : Indonesia  
Affiliation : - Department of condensed matter physics,  
Graduate school of science, Hokkaido University  
Sapporo 060-8010, Japan  
- Meson Science Laboratory  
RIKEN Nishina center for accelerator based science  
2-1 Hirosawa, Wako, Saitama, 351-0198, Japan  
- Department of Physics, Faculty of Science  
Universitas Cokroaminoto Palopo  
Palopo 91921, Indonesia  
Address : Room No. 309, Main Research Building, RIKEN  
: 2-1 Hirosawa, Wako, Saitama, 351-0198, Japan  
Email : irwan.ramli[atmark]riken.jp

## EDUCATION

---

2006-2010 : Bachelor degree, Universitas Negeri Makassar  
2011-2013 : Master degree, Institut teknologi Sepuluh Nopember  
2016-now : Doctoral degree, Hokkaido University

## PUBLICATION

---

- **Irwan Ramli**, S. S. Mohd-Tajudin, M. R. Ramadhan, D.P. Sari, S. Sulaiman, M. I. Mohamed-Ibrahim, B. Kurniawan and I. Watanabe, Magnetic Properties of  $\text{YBa}_2\text{Cu}_3\text{O}_6$  Studied by Density Functional Theory Calculation, *Materials Science Forum* **966**, 257-262 (2019).
- Muhammad Redo Ramadhan, **Irwan Ramli**, Muhammad Darwis Umar, Suci Winarsih, Dita Puspita Sari, Azwar Manaf, Budhy Kurniawan, Mohamed Ismail Mohamed-Ibrahim, Shukri Sulaiman, and Isao Watanabe, Effects of the Supercell's Size on Muon Positions Calculations of  $\text{La}_2\text{CuO}_4$ , *Materials Science Forum* **966**, 465-470 (2019).
- Julia Angel, Retno Asih, Hironori Nomura, Tomoya Taniguchi, Kazuyuki Matsuhira, Muhammad Redo Ramadhan, **Irwan Ramli**, Makoto Wakeshima, Yukio Hinatsu, Mohamed Ismail Mohamed-Ibrahim, Shukri Sulaiman, and Isao Watanabe, Magnetic Properties of Hole-Doped Pyrochlore Iridate  $(\text{Y}_{1-x-y}\text{Cu}_x\text{Ca}_y)_2\text{Ir}_2\text{O}_7$ , *Materials Science Forum* **966**, 269-276 (2019).



## CONFERENCE, WORKSHOP

---

### • Poster presentation

Muon Position and Internal Fields in  $\text{YBa}_2\text{Cu}_3\text{O}_{6+x}$  ( $x \sim 0.6$ ), The eighth International Summer School on HPC Challenges in Computational Sciences, June 25-30, 2017, Boulder, Colorado, USA.

A fast Program for Internal Fields Calculation at the Muon Site, RIKEN Symposium International Workshop on Organic Molecule Systems, August 1-3, 2017, Parkroyal Hotel, Batu Feringghi, Pulau Pinang, Malaysia.

Muon site estimation in some strongly correlated systems, 2017 Autumn Meeting The Physical Society of Japan, September 21-24, 2017, Iwate University, Ueda Campus (3-18-8 Ueda, Morioka-shi, Iwate).

Implanted Muons in Strongly Correlated System, 73rd Annual Meeting The Physical Society of Japan, March 22-25, 2018, Tokyo University of Science, Noda Campus (2641, Noda-shi, Yamazaki).

Density Functional Theory Simulation of Spin Distribution Perturbed by Muon in  $\text{YBa}_2\text{Cu}_3\text{O}_6$ , The 12th International Conference on Materials and Mechanisms of Superconductivity and High Temperature Superconductors(M2S-2018), August 19-24, 2018, Beijing International Convention Center (BICC), Beijing, China.

Ab initio modeling of the implanted muon in  $\text{YBa}_2\text{Cu}_3\text{O}_6$ , 2018 Autumn Meeting The Physical Society of Japan, September 9-12, 2018, Doshisha University, Kyotanabe Campus (Tatara, Kyotanabe-shi).

### • Oral presentation

Rietveld Analysis of Nanocrystalline of Barium M-Hexaferrite Synthesized by Using Coprecipitation Method, Emallia Conference 2016 Winter Theoretical and Experimental Aspects of Advanced Material Sciences Hokkaido Univ.-PNU-RIKEN Joint Symposium, December 19-20, 2016, Hokkaido University, Sapporo.

Development Package for Muon Site and Dipole Fields Calculations, HU/RIKEN-PNU Joint Workshop, April 13th, 2017 (Thu), Pusan National University (PNU), Busan, South Korea.

Muon Sites in high- $T_c$  Superconductor,  $\text{YBa}_2\text{Cu}_3\text{O}_6$ , Emallia Conference 2017 Summer Theoretical and Experimental Aspects of Advanced Material Sciences Hokkaido Univ.-Pusan Univ.-RIKEN Joint Symposium, September 7-8, 2017, Pusan National University (PNU), Busan, South Korea.

Muon Sites in high- $T_c$  Superconductor,  $\text{YBa}_2\text{Cu}_3\text{O}_6$ , RIKEN AICS HPC Youth, February 5 to 6, 2018 Workshop FY2017, Kobe, Japan.

How muon senses ordered Cu spin in  $\text{YBa}_2\text{Cu}_3\text{O}_6$ ? - A supercell approach by DFT calculations-, Muon Spectroscopy User Meeting: Future Developments and Site Calculations, July 16-1, 2018, The Cosener's House, Abingdon, UK.

Study of Microscopic Magnetism in  $\text{YBa}_2\text{Cu}_3\text{O}_6$  by  $\mu\text{SR}$  and DFT, The 4th Emallia Conference 2018 Hokkaido Univ. - Pusan Univ. - RIKEN Symposium, July 23-25, 2018, Hokkaido University, Sapporo.

Covalent bonding effect on the magnetism of  $\text{YBa}_2\text{Cu}_3\text{O}_6$  studied by DFT and  $\mu\text{SR}$ , 4th International Conference on Functional Materials Science 2018 (ICFMS 2018), November 13-15, 2018, Bali, Indonesia.

**AWARD** 

---

- Best poster presentation in 4th International Conference on Functional Materials Science 2018 (ICFMS 2018), November 13-15, 2018, Bali, Indonesia.